

PARAMETERS AFFECTING ADIABATIC EFFECTIVENESS AND
TURBULENCE IN FILM COOLING

A Dissertation

Submitted to the Faculty

of

Purdue University

by

Zachary Taylor Stratton

In Partial Fulfillment of the

Requirements for the Degree

of

Doctor of Philosophy

May 2019

Purdue University

West Lafayette, Indiana

THE PURDUE UNIVERSITY GRADUATE SCHOOL
STATEMENT OF DISSERTATION APPROVAL

Dr. Tom I-P. Shih, Chair

School of Aeronautics and Astronautics

Dr. Gregory Blaisdell

School of Aeronautics and Astronautics

Dr. Jonathan Poggie

School of Aeronautics and Astronautics

Dr. Jun Chen

School of Mechanical Engineering

Approved by:

Dr. Tom I-P. Shih

Head of the School of Aeronautics and Astronautics

ACKNOWLEDGMENTS

I must first express my sincere gratitude to my advisor, Dr. Tom I-P. Shih. His continued support for me and my research throughout my MS and PhD degrees has been invaluable. I must also thank my committee members Dr. Greg Blaisdell, Dr. Jun Chen, and Dr. Jon Poggie for their insight regarding my work and their classes and research that inspired my interest in turbulence and CFD. I would also like to thank all of my lab mates for making my graduate journey so enjoyable: Chien-Shing, Kenny, Jason, Adwiteey, Ashutosh, Irsha, Yongkai, Wanjia, James, Dominik, Wanjae, and Sabina. Finally, I would like to thank my family, Damji, and Fatty for their support.

I would like to thank Dr. Visbal at the Air Force Research Laboratory for providing the large-eddy simulation code used for this work and Dr. Garmann and Dr. Bisek for their help. I would also like to thank Dr. Thole at Penn State University for providing the experimental measurements used for validation. Finally, I would like to thank the American Society of Mechanical Engineers (ASME) for granting permission to reprint my paper (TURBO-18-1195) in this dissertation.

This work was supported by the Ames Laboratory and the National Energy Technology Laboratory with funding from the Department of Energy under contract no. DE-AC02-07CH11358 and agreement no. 26110-AMES-CMI. Additionally, the computational resources to complete this work were provided by the Extreme Science and Engineering Discovery Environment (XSEDE) via the Stampede cluster at the University of Texas at Austin, supported by National Science Foundation grant number ACI-1548562.

TABLE OF CONTENTS

	Page
LIST OF TABLES	vi
LIST OF FIGURES	vii
NOMENCLATURE	x
ABSTRACT	xii
1 INTRODUCTION	1
1.1 Background on Film Cooling	1
1.2 Previous Studies and Motivation	4
1.3 Objectives	9
2 LARGE-EDDY SIMULATION OF FILM COOLING	11
2.1 Problem Description	11
2.2 Governing Equations	13
2.3 Numerical Method	16
2.3.1 Numerical Setup	17
2.4 Results	19
2.4.1 Verification and Validation	20
2.4.2 Instantaneous Flow Field	28
2.4.3 Time-Averaged Flow Field	32
2.4.4 Mean Boundary Layer vs. Resolved Turbulent Boundary Layer	38
2.5 Summary	42
3 IDENTIFYING WEAKNESSES IN EDDY-VISCOSITY MODELS FOR PREDICTING FILM COOLING BY MEANS OF LARGE-EDDY SIMU- LATION	44
3.1 Problem Description	44
3.2 Governing Equations	45
3.3 Numerical Method and Setup	47
3.4 Results	48
3.4.1 Verification and Validation	48
3.4.2 Thermal and Turbulent Field	54
3.4.3 Boussinesq Hypothesis and Eddy Viscosity	55
3.4.4 Gradient-Diffusion Hypothesis and Turbulent Prandtl Number .	59
3.5 Summary	64

	Page
4 EFFECTS OF VELOCITY RATIO ON TRENDS IN FILM-COOLING ADIABATIC EFFECTIVENESS AND TURBULENCE	66
4.1 Problem Description	66
4.2 Results	67
4.2.1 Adiabatic Effectiveness Trends	68
4.2.2 Turbulent Kinetic Energy	76
4.2.3 Reynolds Stresses	77
4.2.4 Turbulent Heat Flux	79
5 CONCLUSIONS AND RECOMMENDATIONS	85
5.1 Summary of Research and Findings	85
5.2 Recommendation for Future Studies	89
REFERENCES	91
A POPE'S MODEL SPECTRUM	97
A.1 Code and Output	98

LIST OF TABLES

Table	Page
2.1 Summary of cases.	12
2.2 Boundary layer mesh resolutions.	20
3.1 Summary of cases.	45
4.1 Summary of cases.	68

LIST OF FIGURES

Figure	Page
1.1 Gas-turbine cooling [1–3].	1
1.2 Film cooling.	2
1.3 Jet-in-crossflow illustration [5].	3
2.1 Computational model.	12
2.2 Computational mesh. (Green ring indicates hole edge).	19
2.3 Turbulent boundary layer profiles non-dimensionalized by viscous units at $Re_{\delta_{mom}} = 670$	21
2.4 v_{rms}^+ , w_{rms}^+ , and uv^+ profiles at $Re_{\delta_{mom}} = 670$	21
2.5 Q-criterion iso-surfaces for a resolved turbulent boundary layer, colored by velocity magnitude.	22
2.6 Longitudinal one-dimensional spectrum.	24
2.7 Adiabatic effectiveness measurements.	26
2.8 Velocity measurements along centerline ($z/D = 0$).	27
2.9 Q-criterion colored by θ with 2-D contour of ω_z . a) Case 1; b) Case 2; c) Case 3; d) Case 4.	29
2.10 Sketch of flow structure near the hole. a) low VR; b) high VR.	30
2.11 Instantaneous non-dimensional temperature at $y/D = 0.05$. a) case 1; b) case 2; c) case 3; d) case 4.	31
2.12 Time-averaged non-dimensional temperature with ω_x contour lines at $x/D = 0.5$ and 2. a) case 1; b) case 2; c) case 3; d) case 4.	33
2.13 Favre-averaged non-dimensional Reynolds normal stresses at $x/D = 2$. a) case 1; b) case 2; c) case 3; d) case 4.	35
2.14 Favre-averaged non-dimensional Reynolds shear stresses at $x/D = 2$. a) case 1; b) case 2; c) case 3; d) case 4.	36
2.15 Favre-averaged non-dimensional turbulent heat fluxes at $x/D = 2$. a) case 1; b) case 2; c) case 3; d) case 4.	37

Figure	Page
2.16 Time-averaged non-dimensional temperature with ω_x contour lines at $x/D = 2$ for a mean and turbulent boundary layer. a) cases 1 and 5; b) cases 4 and 8.	39
2.17 Q-criterion iso-surfaces, colored by θ , for VR = 0.31 (cases 1 and 5).	40
2.18 Non-dimensional turbulent kinetic energy at $x/D = 2$. a) cases 1 and 5; b) cases 4 and 8.	41
3.1 Computational model.	45
3.2 RANS computational mesh.	48
3.3 RANS grid independence for centerline adiabatic effectiveness.	49
3.4 RANS grid independence for laterally averaged adiabatic effectiveness.	49
3.5 Adiabatic effectiveness measurements experiment, LES, and RANS.	51
3.6 Velocity measurements along $z/D = 0$ at $x/D = 3$ and 6.	53
3.7 Non-dimensional temperature and ω_x contours at $x/D = 2$	55
3.8 Turbulent kinetic energy (k) at $x/D = 2$	56
3.9 Stress and strain alignment for VR = 0.91 (high BR/low DR) at $x/D = 0$ computed with LES data.	58
3.10 LES and RANS contours of eddy viscosity at $x/D = 0$	59
3.11 LES and RANS contours of $\widetilde{u''w''}$ at $x/D = 0$	60
3.12 Turbulent heat flux and non-dimensional temperature gradient at $x/D = 0$ computed with LES data.	62
3.13 Turbulent Prandtl number and eddy diffusivity at $x/D = 0$ computed with LES data.	64
4.1 Computational Model.	67
4.2 Adiabatic effectiveness measurements for VR = 0.46	70
4.3 Adiabatic effectiveness measurements for VR = 0.63	71
4.4 Non-dimensional temperature at $z/D = 0$ for VR = 0.63	72
4.5 Non-dimensional temperature with ω_x contour lines at $x/D = 2$ for VR = 0.46	74
4.6 Non-dimensional temperature with ω_x contour lines at $x/D = 2$ for VR = 0.63	75
4.7 Non-dimensional turbulent kinetic energy at $x/D = 0$ for VR = 0.46	77

Figure	Page
4.8 Non-dimensional turbulent kinetic energy at $x/D = 0$ for $VR = 0.63$. . .	78
4.9 Non-dimensional $\widetilde{u''w''}$ at $x/D = 0$ for $VR = 0.46$	80
4.10 Non-dimensional $\widetilde{u''\theta''}$ at $x/D = 0$ for $VR = 0.46$	81
4.11 Non-dimensional $\widetilde{v''\theta''}$ at $x/D = 0$ for $VR = 0.46$	82
4.12 Non-dimensional $\widetilde{w''\theta''}$ at $x/D = 0$ for $VR = 0.46$	83
A.1 Sample output for Pope's model spectra, $Re_L = 26700$	98

NOMENCLATURE

BR	blowing ratio, $\rho_c u_c / \rho_\infty u_\infty$
D	film-cooling hole diameter
DR	density ratio, ρ_c / ρ_∞
E	energy-spectrum function
h	specific enthalpy
k	turbulent kinetic energy
L/D	length-to-diameter ratio of the film-cooling hole
ℓ	Kolmogorov length scale, $(\nu^3 / \epsilon)^{1/4}$
M_∞	crossflow Mach number
MR	momentum-flux ratio, $\rho_c u_c^2 / \rho_\infty u_\infty^2$
p/D	pitch-to-diameter ratio between film-cooling holes
Pr	Prandtl number
Pr_t	turbulent Prandtl number
q	thermal conductivity
Re	Reynolds number based on crossflow values, $u_\infty D / \nu_\infty$
$Re_{\delta_{mom}}$	Reynolds number based on momentum thickness
S_{ij}	strain-rate tensor
T_{aw}	adiabatic wall temperature
T_c	coolant temperature
T_∞	crossflow temperature
u_c	coolant jet velocity
u_τ	friction velocity, $\sqrt{\tau_w / \rho}$
u_∞	crossflow velocity
$\widetilde{u_i'' u_j''}$	Favre-averaged Reynolds stress tensor
$\widetilde{u_i'' \theta''}$	Favre-averaged turbulent heat flux tensor

VR	velocity ratio, u_c/u_∞
x	streamwise coordinate measured from film-cooling hole trailing edge
y	distance normal from film-cooled flat plate
y^+	non-dimensional wall distance, $u_\tau y/\nu$
z	spanwise coordinate measured from center of film-cooling hole

Greek

α_f	filter coefficient
α_t	eddy diffusivity
γ	ratio of specific heats
δ	boundary-layer thickness
δ_{mom}	momentum thickness
Δt	time-step size
η	adiabatic effectiveness, $(T_{aw} - T_\infty)/(T_c - T_\infty)$
θ	non-dimensional temperature, $(T - T_\infty)/(T_c - T_\infty)$
κ	wavenumber
μ	dynamic viscosity
ν	kinematic viscosity
ν_t	eddy viscosity
ρ	density
ω_i	vorticity components

ABSTRACT

Stratton, Zachary T. Ph.D., Purdue University, May 2019. Parameters Affecting Adiabatic Effectiveness and Turbulence in Film Cooling. Major Professor: Tom I-P. Shih.

Gas-turbine engines use film cooling to actively cool turbine components and keep thermal loads on the materials at acceptable levels for structural integrity and service life. The turbulent mixing between the film-cooling jet and the crossflow decreases the coolant temperature, which reduces the cooling performance. This turbulent mixing is sensitive to parameters such as density ratio (DR), blowing ratio (BR), velocity ratio (VR), and momentum-flux ratio (MR) and understanding the effects of these parameters on the turbulent mixing is critical for improving film cooling.

This research seeks to improve understanding by using large-eddy simulation (LES) as a tool to analyze the turbulence of film cooling. With this knowledge it is possible evaluate more fundamental turbulence modeling assumptions utilized by Reynolds-Averaged Navier-Stokes (RANS) approaches as they apply to film cooling. This analysis can provide insight regarding how to improve turbulence models.

The film-cooling problem studied involves the cooling of a flat plate, where the cooling jets issued from a plenum through one row of circular holes of diameter D and length $4.7D$ that are inclined at 35° relative to the plate. Parameters studied include $BR = 0.5 - 1.3$, $DR = 1.1 - 2.1$, $VR = 0.3 - 0.9$, and $MR = 0.16 - 0.9$. For LES, two different boundary layers upstream of the film-cooling hole were investigated - one in which a laminar boundary layer was tripped to become turbulent from near the leading edge of the flat plate, and another in which a mean turbulent BL is prescribed directly without any superimposed turbulent fluctuations. For RANS, two different turbulence models were investigated - realizable $k-\epsilon$ and $k-\omega$ shear-stress-transport (SST). The wall-resolved LES solutions generated are extensively verified

and validated using analytical, DNS, and experimental measurements to ensure high quality.

LES results obtained show that having an upstream boundary layer that does not have turbulent fluctuations enhances the cooling effectiveness significantly at low VRs when compared to an upstream boundary layer that resolved the turbulent fluctuations. However, these differences diminish at higher VRs. Instantaneous flow reveals a bifurcation in the jet vorticity as it exits the hole at low VRs, one branch forming the shear-layer vortex, while the other forms the counter-rotating vortex pair. At higher VRs, the shear layer vorticity is found to reverse direction, changing the nature of the turbulence and the heat transfer. Results obtained also show the strength and structure of the turbulence in the film-cooling jet to be strongly correlated to VR.

RANS results obtained show the turbulent and thermal structure of the jets predicted by the two RANS models to differ considerably. However, both models are consistent in underpredicting the spread of the film-cooling jet. The counter-rotating vortex pair dominates the interaction of the jet and crossflow in the near-wall region, and neither RANS model could predict the strength and structure of this interaction. The gradient-diffusion and Boussinesq hypotheses were evaluated by using the LES data. Comparing LES and RANS results shows that $k-\epsilon$ tends to overpredict eddy viscosity, while SST tends to underpredict the eddy viscosity. Additionally, both models predict very low values of eddy viscosity near the wall which leads to incorrect Reynolds stresses. While regions of counter-gradient diffusion and stress-strain misalignment were identified in the near-wall region, further above the wall, the jet behaved according to the hypotheses.

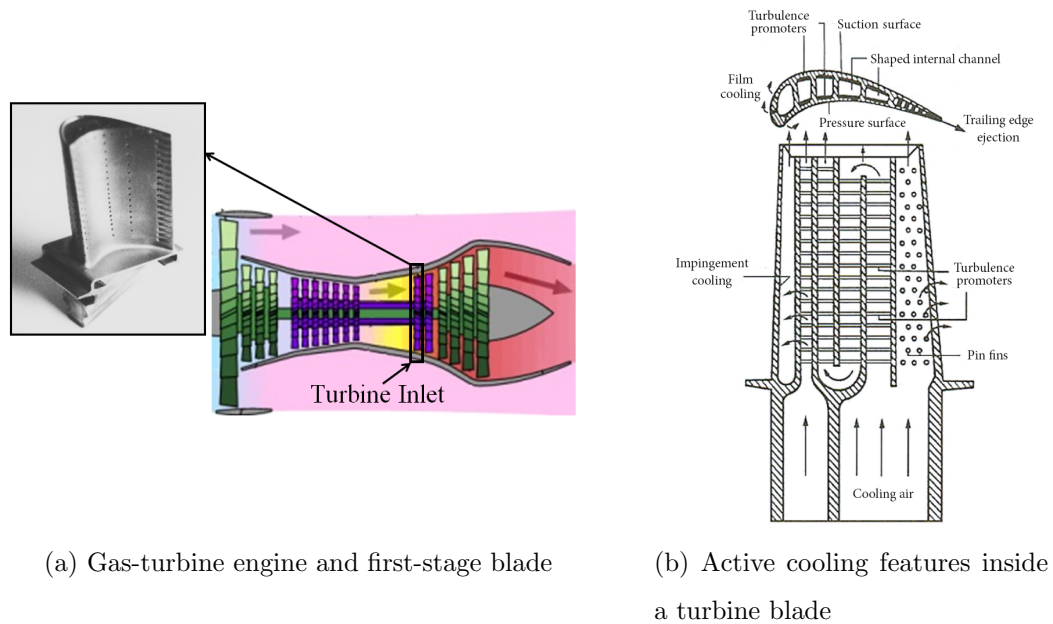
The turbulence scaling when VR is fixed at 0.46 and 0.63 was investigated. The LES results show that separation and spreading of the film-cooling jet increase as BR, DR, and MR increase while VR remains constant. For a given VR, the LES predicts an absolute difference between the minimum adiabatic effectiveness of the lowest and highest MRs to be 2 to 5 times greater than those predicted by RANS. This is because

RANS with either model cannot respond appropriately to changes in MR. However, RANS can correctly predict that adiabatic effectiveness decreases as VR increases. The LES results show the turbulent kinetic energy and Reynolds stresses near the film-cooling hole to change considerably with MRs at a constant VR, while turbulent heat flux changes negligibly. This suggests that while improved turbulence models for heat flux can improve RANS prediction of spreading, capturing trends, however, requires improved modeling of the Reynolds stresses.

1. INTRODUCTION

1.1 Background on Film Cooling

Greater thermal efficiency can be achieved in gas-turbine engines by increasing the temperature at the inlet to the turbine. Today's jet engines desire turbine inlet temperatures above 1600°C , which exceeds the melting point of the turbine's material. The life of the turbine components relies on active cooling schemes to control thermal loads on the material. Figure 1.1a shows a typical turbine blade at the turbine inlet, and Fig. 1.1b shows several ways to cool the turbine.



(a) Gas-turbine engine and first-stage blade

(b) Active cooling features inside a turbine blade

Figure 1.1.: Gas-turbine cooling [1–3].

Film cooling is one way that is often used to cool turbine blades, especially in the first-stage turbine. It is accomplished by bleeding relatively cool air from the compressor and injecting it into serpentine channels within the vanes and blades.

As the air flows through these channels, some is ejected through small holes drilled into the vane's and blade's surface to form a thin film of cool air next to the external surface of the vane and blade, protecting them from the hot gas. Figure 1.2 illustrates the film-cooling concept.

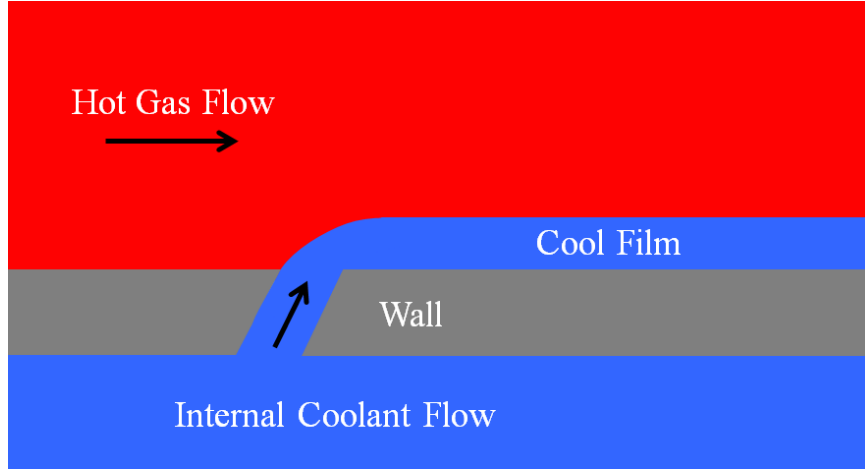


Figure 1.2.: Film cooling.

Film-cooling is one class of jet-in-crossflow (JICF), where the goal is for the jet to remain attached to the wall. Thus, the wall has a strong influence on the resulting flow physics. JICF has been a difficult and intriguing problem in fluid dynamics due to the presence of many different interacting flow structures at any one time with the counter-rotating vortex pair (CRVP) being the most significant [4–6]. Figure 1.3 illustrates a typical JICF with the notable features labeled.

Extensive research has been done to better understand film-cooling flows [7, 8]. Of particular interest is how film-cooling efficiency can be increased by changes in geometry, non-dimensional parameters, and upstream boundary layer. One measure of efficiency and performance is the adiabatic effectiveness. The adiabatic effectiveness is the non-dimensional temperature on the surface of the blade and is defined as

$$\eta = \frac{T_{aw} - T_{\infty}}{T_c - T_{\infty}} \quad (1.1)$$

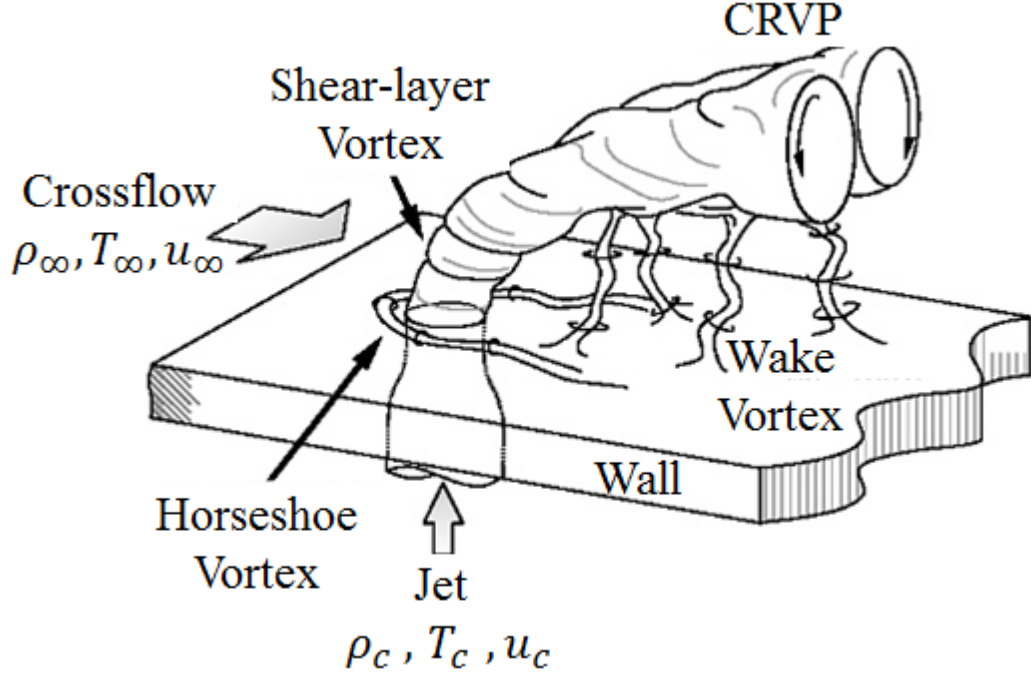


Figure 1.3.: Jet-in-crossflow illustration [5].

where T_{aw} is the adiabatic wall temperature, and T_∞ and T_c are the crossflow and coolant temperatures, respectively (see Fig. 1.3). Adiabatic effectiveness ranges from zero to one, where zero indicates no cooling and one indicates maximum cooling. The adiabatic effectiveness will change depending on the crossflow velocity and density (u_∞, ρ_∞) and the coolant jet velocity and density (u_c, ρ_c). Because the coolant jet velocity is not constant through the film-cooling hole it is typically defined as $u_c = \dot{m}/(\rho_c A_c)$, where \dot{m} is the mass-flow rate through the hole and A_c is the cross-sectional area of the hole. These parameters form four important non-dimensional parameters that are useful for defining film-cooling flows: 1) the density ratio (DR), which is the ratio of the coolant to crossflow density,

$$\text{DR} = \frac{\rho_c}{\rho_\infty}; \quad (1.2)$$

2) the velocity ratio (VR), which is the ratio of the coolant to crossflow velocity,

$$\text{VR} = \frac{u_c}{u_\infty}; \quad (1.3)$$

3) the blowing ratio (BR), which is the ratio of the coolant mass flux to the crossflow mass flux,

$$\text{BR} = \frac{\rho_c u_c}{\rho_\infty u_\infty}; \quad (1.4)$$

4) the momentum-flux ratio (MR), which is the ratio of the coolant momentum flux to the crossflow momentum flux,

$$\text{MR} = \frac{\rho_c u_c^2}{\rho_\infty u_\infty^2}. \quad (1.5)$$

1.2 Previous Studies and Motivation

Computational fluid dynamics (CFD) has been useful to provide understanding of the turbulent flow associated with film cooling and how design and operating parameters affect film cooling. However, many early studies have shown CFD based on Reynolds-Averaged Navier-Stokes (RANS) to be ineffective in predicting trends in film cooling. This is because most RANS are based on eddy-viscosity models, and they are unable to predict the high degree of anisotropy in film-cooling flows. In particular, they are unable to capture the correct lateral spreading of the cooling jet [9–11].

Over the last decade many researchers have turned to large-eddy simulation to analyze film-cooling flows which has produced many insightful results over a very wide range of setups and flow conditions. Of particular interest are studies that look at the effect of imposing a laminar or mean velocity profile and a resolved turbulent boundary layer upstream of the coolant hole; while the former offers a significant reduction in computational cost it can have a significant impact on the film-cooling effectiveness. Another topic of interest are studies that look at a range of DR or BR and show how the physics evolve over this range. Tyagi et al. [12] was one of the

first efforts to study film cooling with LES and find that LES can match more closely with experimental results than RANS; additionally, they identify several coherent structures and find that “hot spots” occur due to the entrainment associated with the hairpin structures. Dai et al. [13] analyzes the instantaneous flow structures showing how the hairpin and CRVP form and evolve over different VR. Sakai et al. [14] shows how the unsteady vortical structures drastically change with blowing ratio, in addition they look at the effect of a turbulent versus laminar boundary layer on film cooling effectiveness and find that the jet is more impacted by the choice of boundary layer at low BR. Zhong et al. [15] study the effect of a laminar versus turbulent boundary layer on film-cooling effectiveness and coherent structures and note that the turbulent boundary layer enhanced the mixing of the coolant and main flow. Ziefle et al. [16, 17] study the effect of a boundary layer with and without resolved turbulent fluctuations for $BR = 0.5$ and $DR = 2.0$ and conclude that that a resolved turbulent boundary must be used for LES of film cooling. Kalghatgi et al. [18] use dynamic mode decomposition to analyze the instantaneous structures for $BR = 1$ and $DR = 2$ and show that the low frequency streamwise-oriented modes contribute the most toward wall temperature fluctuation; additionally they showed that a mean inflow profile was sufficient to match experimental measurements. Renze et al. [19] studied multiple BRs and DRs utilizing a resolved turbulent boundary layer and showed how the CRVP formed and that VR had an impact on the separation and reattachment of the cooling jet. Sakai et al. [20] studied a range of DRs and found that the hairpin vortices are dominant at low DR, whereas they are suppressed at high DR; additionally they studied the effect of a turbulent boundary layer and found the cooling effectiveness decreased. Stratton et al. [21] studied film cooling with compound angled holes and found LES can match the experimental data well when the turbulent boundary layer is resolved. Rodebaugh et al. [22] compared mean velocity profiles with a resolved turbulent boundary layer for compound angled holes and found that results generally improved when the turbulent boundary layer was resolved, but in some cases it had no effect. Whereas there have been several LES

studies that analyze the turbulence near film-cooling holes [23–28], few have focused on it in the context of varying upstream boundary layer or over a range of DR.

The majority of research on the effect of DR has been studied experimentally. One of the first studies, completed in 1975, by Foster et al. [29] showed that at a fixed DR and increasing VR, the film cooling effectiveness near the hole ($x/D < 15$) decreases while film cooling effectiveness further downstream increases; additionally, for a fixed VR and increasing DR, the adiabatic effectiveness increases. Goldstein et al. [30] found adiabatic effectiveness to be strongly dependent on DR, with DR affecting the separation and reattachment of the jet, the lateral spreading, and the energy transfer between the jet and mainflow. Pietrzyk et al. [31, 32] made many hydrodynamic measurements of film-cooling flow and found that the turbulence intensity at the mid-hole plane scales with VR. Sinha et al. [33] found that separation and reattachment of the film-cooling jet can be scaled with MR, but the cooling effectiveness cannot be scaled with BR, VR, or MR. Johnson et al. [34] shows that VR can be used with some success to scale the film cooling effectiveness for high BR cases. Zhou et al. [35] study a range of BR, Mach numbers, and DR, they find that denser coolant results in better film-cooling effectiveness and VR has a dominant effect in the near hole region ($x/D < 10$). Vinton et al. [36] study the impact of freestream acceleration and DR on film-cooling effectiveness and conclude that increasing DR at constant BR increases the lateral spread of the coolant and that MR cannot be used to scale film-cooling effectiveness. Eberly et al. [37, 38] studied a range of DRs and BRs for different p/D and hole geometries and found that turbulence levels in the jet scale with MR and that increasing DR increases the lateral spreading of the coolant.

Large-eddy simulations and experimental studies can be expensive and slow, whereas RANS simulations can be efficient with fast turn-around times in generating solutions. In particular, RANS offers considerable cost savings versus rig testing when it comes to designing compressors and turbines in gas-turbine engines [39]. Additionally, algorithms for optimizing film-cooling hole design rely on computationally cheap RANS solutions [40]. Durbin’s recent review of turbulence modeling also suggests

that RANS modeling will remain an essential element of applied CFD for the foreseeable future [41]. Therefore, there is a desire to improve RANS turbulence models to better predict cooling trends of film-cooling flows.

There has been several attempts by researchers to improve turbulence modeling for film cooling, models that could more accurately account for anisotropy. Bergeles et al. [42] was one of the first to apply an anisotropic turbulence model to a jet-in-crossflow by multiplying the eddy viscosity in the lateral direction by a correction factor that varied based on wall-normal distance. This correction, based on pipe-flow data, was applied in the log-law region and above. Lakehal et al. [43] extended Bergeles' model to include the viscous sublayer as well. Though these models improved the lateral spreading, the peak values of adiabatic effectiveness were underestimated. Azzi and Lakehal [44] used an explicit algebraic stress model to calculate each Reynolds stress in combination with a two-layer model to account for near-wall anisotropy. Although this model showed some improvement over turbulence models based on a scalar eddy viscosity, it was still unable to capture the lateral spreading. Lakehal [45] further extended the anisotropic model of [42, 43] by using the near-wall velocity scale ($\overline{v'v'}$) and dissipation (ϵ) from channel-flow direct numerical simulation (DNS) data and by having the turbulent Prandtl number (Pr_t) vary with Re_{y_n} , where y_n is the normal distance from the wall. The anisotropic model in combination with the variable Pr_t significantly improved cooling predictions for film-cooling of a flat plate, but underestimated cooling over a turbine blade. Jones et al. [46] employed the $v^2f-k\omega$ model for film-cooling flows, but little improvement was seen over scalar models. However, when the $v^2f-k\omega$ model was combined with a variable Pr_t formulation, better lateral spreading of the coolant was observed. Liu et al. [47, 48] studied the effect of Pr_t using scalar eddy-viscosity models and found that allowing the Pr_t to vary laterally or as a function of non-dimensional temperature can further improve cooling predictions for round holes at both low and high BRs. However, it was found that solely varying Pr_t has little affect on the cooling predictions for a slot jet, where the wall has significant influence on the flow field. Li et al. [49, 50] devised an algebraic

anisotropic eddy-viscosity model and scalar flux model, where they multiplied ν_t by correction factors derived from an algebraic Reynolds stress model to get $\nu_{t,ij}$. This model improves cooling predictions by better capturing lateral spreading and cooling magnitude. However, the separation and reattachment near the hole do not match the experimental data.

Recently, machine learning has been explored as a potential method to improve turbulence modeling [51]. Machine learning is able to extract patterns from large data sets and form mathematical expressions that can be applied to turbulence modeling (i.e., relating stress to strain or heat flux to temperature gradient). These large data sets are now more available than ever thanks to databases containing LES and DNS solutions. Ling et al. [52] proposes that machine learning can be used to identify regions of high RANS uncertainty. Weatheritt et al. [53] uses symbolic regression to improve the model for Reynolds stress anisotropy. Ling et al. [54] and Kutz [55] show how deep neural networks can also be used to improve models of the Reynolds stresses. Sandberg et al. [56] shows how gene expression programming techniques can be used to improve adiabatic effectiveness predictions in trailing-edge slot flows. Milani et al. [57] shows how random forests can be used to better model the turbulent heat flux to improve film-cooling predictions in RANS. These results show a very promising union between machine learning and turbulence modeling in the near future. However, in order to apply the methods described above to improve turbulence modeling, the turbulence behaviour in the flow of interest must be understood.

Magnetic resonance imaging (MRI) experiments and large-eddy simulation (LES) of film cooling can be used to study the fundamental assumptions invoked by RANS models and provide insight toward model development. Coletti et al. [27] used MRI data to show that eddy viscosity is strongly non-uniform and anisotropic. Additionally, it was shown that eddy diffusivity should increase downstream to capture scalar mixing, but eddy viscosity should decrease downstream to capture the persistence of the CRVP - suggesting that models should account for variable Pr_t . Ling et al. [58] examined various scalar flux models and found that all models showed large errors in

the near-wall region. It was also shown that Pr_t varies significantly with lower values near the wall. Ling et al. [59] found negative eddy viscosities and strongly anisotropic flow in a JICF using LES data.

1.3 Objectives

The objective of this study is four-fold:

1. Understand the flow physics of film cooling and scaling of turbulence quantities with blowing ratio, density ratio, and velocity ratio. Many LES studies focus on a single DR, with only few exceptions, notably [19,20], but their focus is not on the turbulence near the jet. Many experimental studies have varied the DR, but often lack the measurement tools to examine the three-dimensional turbulent flow field. LES simulations of film cooling will be validated with experimental measurements and then used to determine how different turbulence quantities scale with VR and how this scaling is related to the adiabatic effectiveness.
2. Understand mean versus turbulent boundary layer inflow for film cooling. While several studies have suggested that a resolved turbulent boundary layer is necessary for LES to accurately predicting the cooling effectiveness, others have matched experimental data with a simple mean profile without superimposed turbulence. The effect of a mean velocity profile without superimposed turbulence imposed at the inflow versus a resolved turbulent boundary layer will be evaluated over a range of VRs. This objective is addressed in Chapter 2.
3. Identify weaknesses in eddy-viscosity models for predicting film cooling by means of large-eddy simulation. High-resolution LES data can provide insight for turbulence-model development. A limitation of some of the previous studies [27, 58, 59] is that the analysis is limited to one set of parameters (e.g. BR = 1, DR = 1). Because film cooling performance is very sensitive to the flow parameters, it is desirable to analyze the RANS assumptions over a range of

parameters. The objective of this study is to use the computed LES results, for film cooling of a flat plate through one row of circular holes, to evaluate RANS models and assumptions. The first part of this objective focuses on evaluating the cooling, vorticity, and turbulent kinetic energy trends of two RANS models (realizable $k-\epsilon$ and $k-\omega$ SST) for a range of parameters (BR = 0.5 and 1.0 and DR = 1.1 and 1.6). The second part examines where in the flow, if any, the Boussinesq hypothesis and gradient-diffusion hypothesis are appropriate assumptions over a range of parameters. This objective is addressed in Chapter 3.

4. Understand how trends in film-cooling adiabatic effectiveness and turbulence scales with BR, DR, MR when VR is fixed. Additionally, with the advent of machine learning and its promising application to turbulence modeling, another objective is to understand which turbulence quantities are most impactful for predicting trends in adiabatic effectiveness. Thus, RANS simulations with two turbulence models, realizable $k-\epsilon$ and $k-\omega$ SST, are, again, evaluated with respect to the LES data to determine where turbulence predictions need to be improved in order to capture cooling trends when VR is fixed. This objective is addressed in Chapter 4.

2. LARGE-EDDY SIMULATION OF FILM COOLING

In this chapter, the LES results are presented that address the first two objectives. First, the chosen film-cooling problem is described. Next, the governing equations, numerical method, and setup are presented. Finally, the simulation results including verification and validation, scaling of turbulence quantities, and inflow effects are shown. Parts of this chapter are adapted from the journal publication by Stratton and Shih [60].

2.1 Problem Description

The problem selected to address the objective of this study is shown in Fig. 2.1. It consists of a flat plate film cooled by jets issuing from a plenum through one row of circular holes. Each hole has diameter, $D = 2.6$ mm, and length, $L = 4.7D$, and is inclined at 35° with respect to the plate. The holes along the row are spaced $3D$ apart.

The hot-gas above the plate is air. The hot gas at the inflow boundary has velocity, $U_\infty = 36.35$ m/s, and temperature that is either $T_\infty = 296$ K or $T_\infty = 329$ K depending on the DR. The coolant is also air and has a temperature of either $T_c = 269$ K or $T_c = 203$ K. The operating conditions were chosen to yield a Mach number of $M = 0.1$, DR = 1.1 and 1.6, and BR = 0.5 and 1.0. These parameters give rise to four different VRs ranging from 0.313 to 0.909. The Reynolds numbers for DR = 1.1 and 1.6, based on hole diameter and crossflow velocity and viscosity, are $Re = 5135$ and $Re = 6160$, respectively.

The turbulent boundary layer, measured $5D$ upstream of the hole, has a boundary layer thickness of $\delta = 1.2D$ and momentum thickness of $\delta_{mom} = 0.13D$, which corresponds to a $Re_{\delta_{mom}} = 670$. A summary of cases studied is given in Table 2.1.

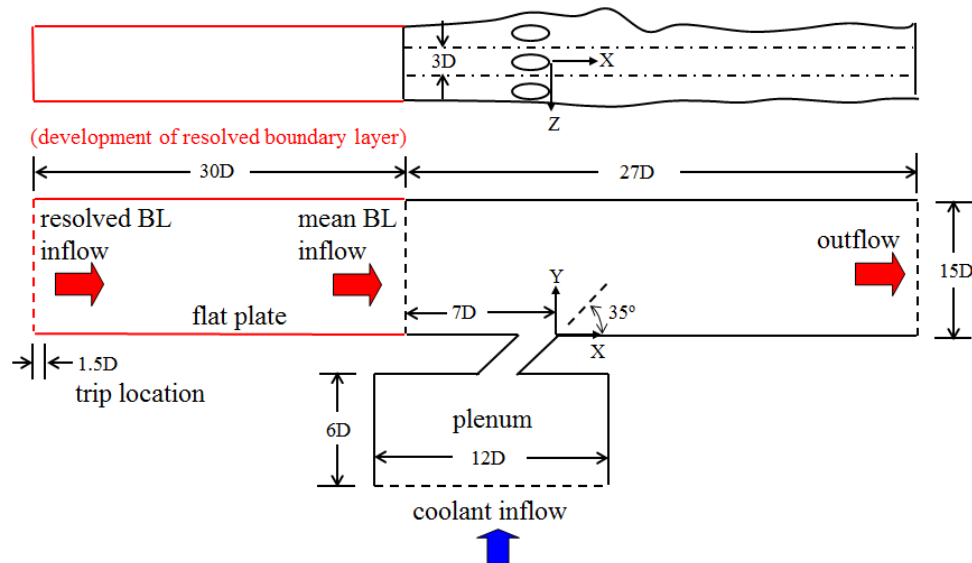


Figure 2.1.: Computational model.

Table 2.1.: Summary of cases.

Case	Boundary Layer	DR	BR	VR	MR	$T_c(K)$	$T_\infty(K)$
1	Resolved	1.6	0.5	0.313	0.156	203	329
2	Resolved	1.1	0.5	0.455	0.227	269	296
3	Resolved	1.6	1.0	0.625	0.625	203	329
4	Resolved	1.1	1.0	0.909	0.909	269	296
5	Mean Profile	1.6	0.5	0.313	0.156	203	329
6	Mean Profile	1.1	0.5	0.455	0.227	269	296
7	Mean Profile	1.6	1.0	0.625	0.625	203	329
8	Mean Profile	1.1	1.0	0.909	0.909	269	296

The geometry and flow conditions chosen for this study correspond to those in the experiment by Eberly and Thole [38]. Their experimental data were used to validate the LES simulations.

2.2 Governing Equations

In this study, implicit LES is used, meaning the governing equations are unfiltered, and there is no need for a subgrid-scale model. The governing equations employed are the unsteady, three-dimensional continuity, momentum and total energy equations. For compressible flows, these equations are as follows:

$$\frac{\partial \rho}{\partial t} + \frac{\partial}{\partial x_i} (\rho u_i) = 0 \quad (2.1)$$

$$\frac{\partial}{\partial t} (\rho u_i) + \frac{\partial}{\partial x_j} (\rho u_j u_i - \sigma_{ji}) = f_i, \quad (2.2)$$

$$\frac{\partial}{\partial t} (\mathcal{E}) + \frac{\partial}{\partial x_j} (u_j \mathcal{E} - \sigma_{ji} u_i + \Theta_j) = f_i u_i, \quad (2.3)$$

where ρ is the density; u_i are the velocity components; σ_{ji} is the stress tensor; \mathcal{E} is the total energy; Θ_i is the heat flux; and f_i is a body force. The stress tensor, total energy, and heat flux are given by

$$\sigma_{ji} = -p\delta_{ij} + \mu \left(\frac{\partial u_i}{\partial x_j} + \frac{\partial u_j}{\partial x_i} \right) - \frac{2}{3}\mu \frac{\partial u_k}{\partial x_k} \delta_{ij}, \quad (2.4)$$

$$\mathcal{E} = \rho \left(e + \frac{u_i u_i}{2} \right), \quad (2.5)$$

$$\Theta_i = -q \frac{\partial T}{\partial x_i}, \quad (2.6)$$

where p is the pressure; T is the temperature; μ is the dynamic viscosity; δ_{ij} is the Kronecker delta; e is the internal energy ($c_v T$); and q is the thermal conductivity. The fluid is air and assumed to be thermally perfect so that $p = \rho RT$.

The governing equations can be rewritten in a different form to assist in solving them numerically. Introducing a general time-dependent curvilinear coordinate transformation from physical to computational space and expressing in strong conservation form, the non-dimensional equations are:

$$\frac{\partial}{\partial \tau} \left(\frac{\mathbf{Q}}{J} \right) + \frac{\partial \mathbf{F}}{\partial \xi} + \frac{\partial \mathbf{G}}{\partial \eta} + \frac{\partial \mathbf{H}}{\partial \zeta} = \frac{1}{Re} \left[\frac{\partial \mathbf{F}_v}{\partial \xi} + \frac{\partial \mathbf{G}_v}{\partial \eta} + \frac{\partial \mathbf{H}_v}{\partial \zeta} \right] \quad (2.7)$$

where the solution vector is $\mathbf{Q} = [\rho, \rho u, \rho v, \rho w, \rho E]^T$ and the transformation Jacobian is $J = \partial(\xi, \eta, \zeta, \tau) / \partial(x, y, z, t)$. The inviscid flux vectors are:

$$\begin{aligned} \mathbf{F} &= \frac{1}{J} \begin{bmatrix} \rho U \\ \rho u U + \xi_x p \\ \rho v U + \xi_y p \\ \rho w U + \xi_z p \\ (\rho E + p)U - \xi_t p \end{bmatrix}, \\ \mathbf{G} &= \frac{1}{J} \begin{bmatrix} \rho V \\ \rho u V + \eta_x p \\ \rho v V + \eta_y p \\ \rho w V + \eta_z p \\ (\rho E + p)V - \eta_t p \end{bmatrix}, \\ \mathbf{H} &= \frac{1}{J} \begin{bmatrix} \rho W \\ \rho u W + \zeta_x p \\ \rho v W + \zeta_y p \\ \rho w W + \zeta_z p \\ (\rho E + p)W - \zeta_t p \end{bmatrix}. \end{aligned} \quad (2.8)$$

In these equations U , V , and W are the contravariant velocities, given as:

$$\begin{aligned} U &= \xi_t + \xi_x u + \xi_y v + \xi_z w \\ V &= \eta_t + \eta_x u + \eta_y v + \eta_z w \\ W &= \zeta_t + \zeta_x u + \zeta_y v + \zeta_z w \end{aligned} \quad (2.9)$$

and the total energy is:

$$E = \frac{T}{\gamma(\gamma - 1)M_\infty^2} + \frac{1}{2} (u^2 + v^2 + w^2) \quad (2.10)$$

where γ is the ratio of specific heats and M_∞ is the crossflow Mach number. The metric quantities are given as $\xi_x = \partial\xi/\partial x$, for example. The viscous fluxes are:

$$\begin{aligned}
\mathbf{F}_v &= \frac{1}{J} \begin{bmatrix} 0 \\ \xi_{x_i} \sigma_{i1} \\ \xi_{x_i} \sigma_{i2} \\ \xi_{x_i} \sigma_{i3} \\ \xi_{x_i} (u_j \sigma_{ij} - \Theta_i) \end{bmatrix}, \\
\mathbf{G}_v &= \frac{1}{J} \begin{bmatrix} 0 \\ \eta_{x_i} \sigma_{i1} \\ \eta_{x_i} \sigma_{i2} \\ \eta_{x_i} \sigma_{i3} \\ \eta_{x_i} (u_j \sigma_{ij} - \Theta_i) \end{bmatrix}, \\
\mathbf{H}_v &= \frac{1}{J} \begin{bmatrix} 0 \\ \zeta_{x_i} \sigma_{i1} \\ \zeta_{x_i} \sigma_{i2} \\ \zeta_{x_i} \sigma_{i3} \\ \zeta_{x_i} (u_j \sigma_{ij} - \Theta_i) \end{bmatrix},
\end{aligned} \tag{2.11}$$

where the stress tensor is

$$\sigma_{ij} = \mu \left(\frac{\partial \xi_k}{\partial x_j} \frac{\partial u_i}{\partial \xi_k} + \frac{\partial \xi_k}{\partial x_i} \frac{\partial u_j}{\partial \xi_k} - \frac{2}{3} \delta_{ij} \frac{\partial \xi_l}{\partial x_k} \frac{\partial u_k}{\partial \xi_l} \right) \tag{2.12}$$

and the heat flux vector is

$$\Theta_i = \left[\frac{1}{(\gamma - 1) M_\infty^2} \right] \left(\frac{\mu}{Pr} \right) \frac{\partial \xi_j}{\partial x_i} \frac{\partial T}{\partial \xi_j} \tag{2.13}$$

where $\xi_i (\equiv \xi, \eta, \zeta)$ in Eqs. 2.12 and 2.13.

For these equations the perfect-gas equation is $p = \rho T / \gamma M_\infty^2$. The length scale is non-dimensionalized by D and all flow variables are non-dimensionalized by their crossflow values, except pressure, which is non-dimensionalized by $\rho_\infty u_\infty^2$. Sutherland's law is used for viscosity, $\mu = T^{3/2} \frac{1+0.38}{T+0.38}$. A constant Prandtl number ($Pr = 0.72$) and Stokes hypothesis for bulk viscosity are assumed.

2.3 Numerical Method

The LES simulations are performed with the Navier-Stokes solver, FDL3DI [61, 62]. The equations are discretized by using a finite-difference approach. Spatial derivatives were approximated by sixth-order accurate compact operators [63] at the interior points. At boundary points, one-sided formulas are utilized, in which the operator drops to fifth-order one point off the boundary and fourth-order at the boundary. Second derivatives are computed by applying the first derivative operator twice.

Time derivatives were approximated by a second-order accurate three-point backward formula. The solution algorithm is implicit and uses the approximately-factored scheme of Beam and Warming [64] with the diagonal form of Pulliam and Chaussee [65] to reduce computational cost. Sub-iterations were used to eliminate factorization errors and achieve second-order accuracy at each time step.

An eighth-order low-pass filter is applied to filter high-wavenumber components of the solution. This filter replaces the computed value, ϕ_i , with a filtered value, $\hat{\phi}_i$, at a particular node after each sub-iteration using:

$$\alpha_f \hat{\phi}_{i-1} + \hat{\phi}_i + \alpha_f \hat{\phi}_{i+1} = \sum_{n=0}^N \frac{a_n}{2} (\phi_{i+n} + \phi_{i-n}) \quad (2.14)$$

where α_f is the filter coefficient and a_n is a constant. The α_f is set at 0.4 at the interior points. One-side biased filters are used near the boundaries. To reduce dispersion associated with the biased filter the order is reduced to fourth-order and α_f is increased. Since the filter removes the smallest length scales in the flow, it acts as an alternative to traditional sub-grid scale models, and this is known as implicit LES [66]. By removing the smallest length scales that are typically under-resolved and will alias, this filter also acts to suppress numerical instabilities [67]. This approach has been shown to yield similar or improved results compared to traditional SGS approaches at reduced computational cost [68]. Additionally, it has been shown to seamlessly approach DNS as the grid resolution is increased [69].

This numerical algorithm is implemented for structured meshes with overset capability. A sixth-order interpolation is used to interpolate data between the overset meshes [70].

2.3.1 Numerical Setup

For the “mean profile” cases, shown in Tab. 2.1, the inflow boundary condition is a $1/7^{th}$ power-law mean turbulent boundary profile with $\delta = 1.1D$. This profile is imposed without any turbulent fluctuations or mean turbulent kinetic energy profile. This is among the simplest inflow boundary conditions that can be imposed, however, applying this boundary condition assumes that turbulent fluctuations in the boundary layer are of negligible impact.

For the “resolved” cases the inflow boundary condition is a laminar boundary layer profile with $\delta = \delta_0 = 0.4D$, corresponding to $Re_{\delta_{mom}} = 270$. This laminar profile is tripped and develops spatially into a turbulent boundary layer. Transition to turbulent flow is controlled via a body-force trip positioned $1.5D$ downstream of the inlet [69]. This body-force takes on the following form:

$$f = \frac{2D_c}{\pi x_{\text{ref}} y_{\text{ref}} z_{\text{ref}}} \sin^2 \left(\pi \frac{z - Z}{z_{\text{ref}}} \right) \exp \left[- \left(\frac{x - X}{x_{\text{ref}}} \right)^2 - \left(\frac{y - Y}{y_{\text{ref}}} \right)^2 \right] \quad (2.15)$$

where $f_x = f \cos \phi$, $f_y = f \sin \phi$, and $f_z = 0$. The center of the source is located at $(X = -35.5, Y = 0.0, Z = 0.0)$, and the width, height, and spanwise variation of the force is given by $x_{\text{ref}} = 0.04$, $y_{\text{ref}} = 0.004$, and $z_{\text{ref}} = 0.4$, respectively. It is positioned such that the turbulent boundary layer measured $5D$ upstream of the hole has $Re_{\delta_{mom}} = 670$. The strength of the force is $D_c = 0.06$, and $\phi = 179$. This artificial body force and its corresponding work were added to the momentum and total energy equations.

At the symmetry planes between holes, periodic boundary conditions were imposed. Note that only one hole was simulated. At the plenum inflow, velocity and temperature were imposed without any superimposed turbulence. At the outflow boundary above the plate, the static pressure was set at 1 atm. The flow variables are extrapolated at the top and end of the domain; at these boundaries rapid grid

stretching is employed in addition to the low-pass filter described earlier, which creates a type of sponge layer that eliminates spurious reflections. All walls are adiabatic and no-slip with zero-normal pressure gradient approximated by a third-order accurate extrapolation.

The domain is discretized using 16 overset structured blocks, as seen in Fig. 2.2. As the figure indicates, there is a finer mesh that extends to about $2.5D$ above the flat plate, above which there is a coarser mesh in the less relevant freestream region that is stretched towards the top of the domain. At the outlet there is also a $5D$ region where the grid is stretched aggressively. Care was taken to exactly match grid points in the overlap region where possible. In regions where grids cannot be perfectly matched, such as between the o-grid and h-grid, the cell volumes are closely matched, which is shown to reduce interpolation errors [71]. The mesh consists of grid spacings of $\Delta x^+ = 9$, $0.4 < \Delta y^+ < 8$ (from the wall to the edge of the boundary layer), $\Delta z^+ = 5$ upstream of the hole and similar values downstream of the hole. The $\Delta y^+ = 0.4$ value corresponds to a spacing of $\Delta y = 0.001D$. The total mesh size was 22×10^6 grid points for the “mean profile” cases and 35×10^6 grid points for the “resolved” cases which is due to the additional upstream mesh necessary for resolving the boundary layer. With a total mesh size of 35×10^6 grid points there are approximately 13×10^6 in the boundary layer transition region, 3.0×10^6 in the plenum, 6.0×10^6 in the hole, and 10×10^6 downstream of the hole.

The non-dimensional timestep of $\Delta t u_\infty / D = 4 \times 10^{-4}$ was used for all simulations, resulting in a Courant number well below one. The low Mach number and skewed cells in the hole, due to the hole angle of 35° , necessitated a small time step. Additionally, this time-step ensured that the small time-scales were resolved. The simulations were run for ~ 5 flow-through time periods (based on freestream velocity and a domain length of $27D$) to allow the transient flow to settle before time-averaging over ~ 6 flow-through time periods. The total simulation of the “resolved” film cooling case required $\sim 7 \times 10^5$ timesteps which required ~ 70000 cpu-hours (70 hours on 1000 cores).

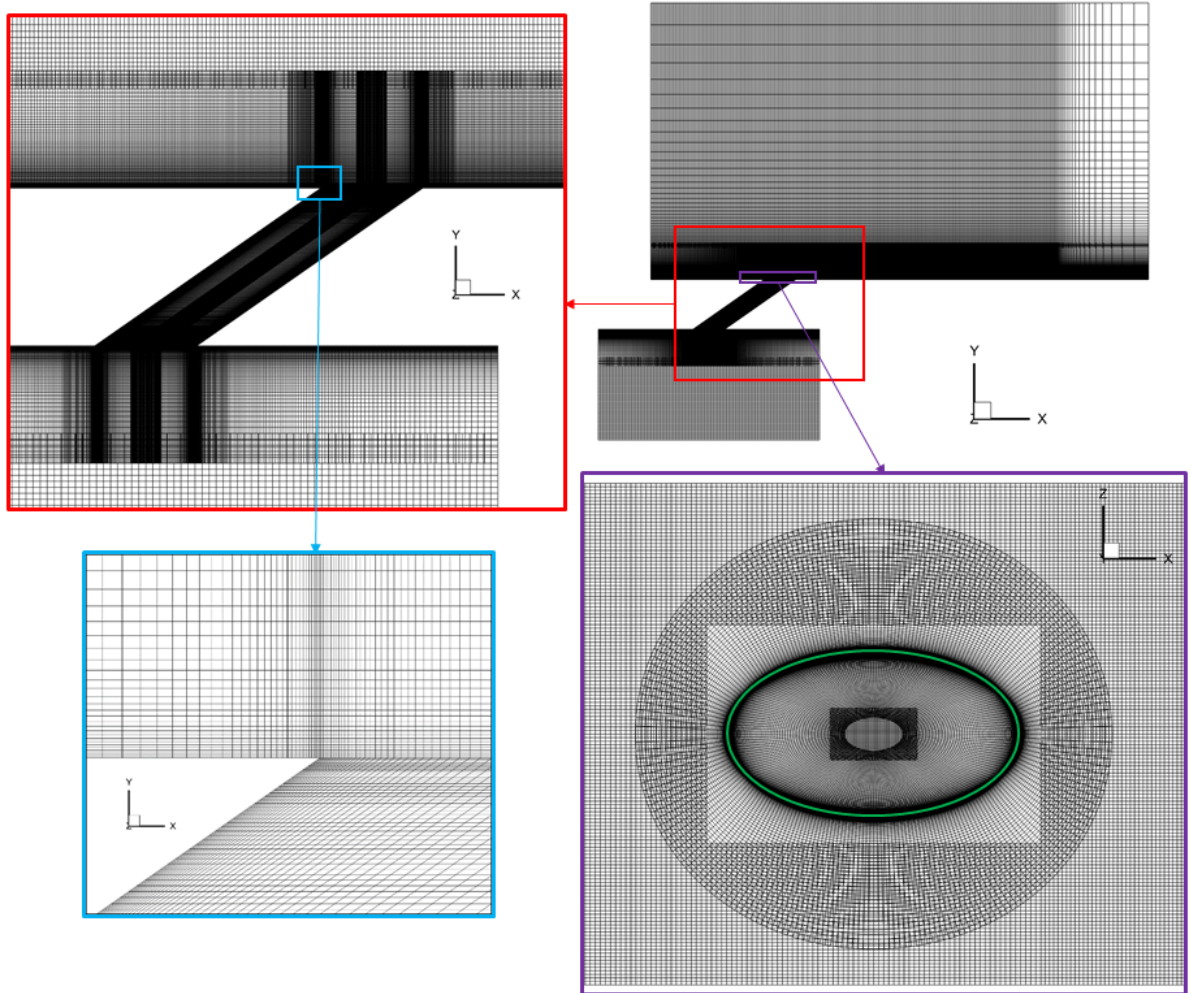


Figure 2.2.: Computational mesh. (Green ring indicates hole edge).

2.4 Results

The results of this study are organized as follows. First, the meaningfulness of the LES solutions are examined through a grid-sensitivity study, including a comparison of turbulence quantities with DNS and experimental turbulent boundary layer data and an analysis of velocity spectra. Afterwards, the adiabatic effectiveness and velocities computed on the optimal grid is compared with experimental thermal and particle image velocimetry (PIV) measurements. Next, the instantaneous flow field

is visualized with Q-criterion, vorticity, and non-dimensional temperature measurements. This is followed by analysis of the time-averaged thermal, Reynolds stress, and turbulent heat flux measurements. Finally, the “mean profile” cases are compared with the “resolved” boundary layer cases to understand the advantages and disadvantages of this approach.

2.4.1 Verification and Validation

To accurately simulate mixing between the crossflow and the film-cooling jet it is crucial that the upstream boundary layer is properly resolved. To ensure the near-wall resolution was sufficient to resolve the turbulent boundary layer, boundary layer simulations were run in isolation and compared to experimental PIV measurements of Eberly and Thole [38] and DNS measurements of Schlatter and Orlu [72]. A coarse and fine mesh were evaluated with the resolution details shown in Tab. 2.2. The Δy_w^+ and Δy_e^+ columns refer to the wall and edge of boundary layer, respectively.

Table 2.2.: Boundary layer mesh resolutions.

Mesh	Δx^+	Δy_w^+	Δy_e^+	Δz^+	Grid points
Coarse	17	0.4	10	8	8×10^6
Fine	9	0.4	8	5	24×10^6

The non-dimensional streamwise velocity and turbulent fluctuation profiles at $Re_{\delta_{mom}} = 670$ are shown in Fig. 2.3. These figures show that the coarse mesh profile overshoots the log-law as-well as overshoots the near-wall peak in u_{rms}^+ , these are typical signs that there is a lack of resolution in the near-wall region [69]. When the mesh is refined there is good agreement with the log-law, as well as the DNS and experimental data. Additional turbulence measurements are shown in Fig. 2.4, for these quantities the experimental data is unavailable. The coarse mesh tends to underestimate v_{rms}^+ near the wall, however the coarse and fine mesh agree well with the

DNS measurements for w_{rms}^+ and wv^+ . The region that shows the most disagreement is near the edge of the boundary layer at $y^+ \approx 300$. However, in this region there often discrepancies among DNS results at this relatively low $Re_{\delta_{mom}}$ and the data of Schlatter and Orlu generally tend to predict smaller fluctuations compared to other DNS results [73]. To get a sense of the turbulent structure of the resolved turbulent boundary layer, Q-criterion iso-surfaces, colored by velocity magnitude, are shown in Fig. 2.5.

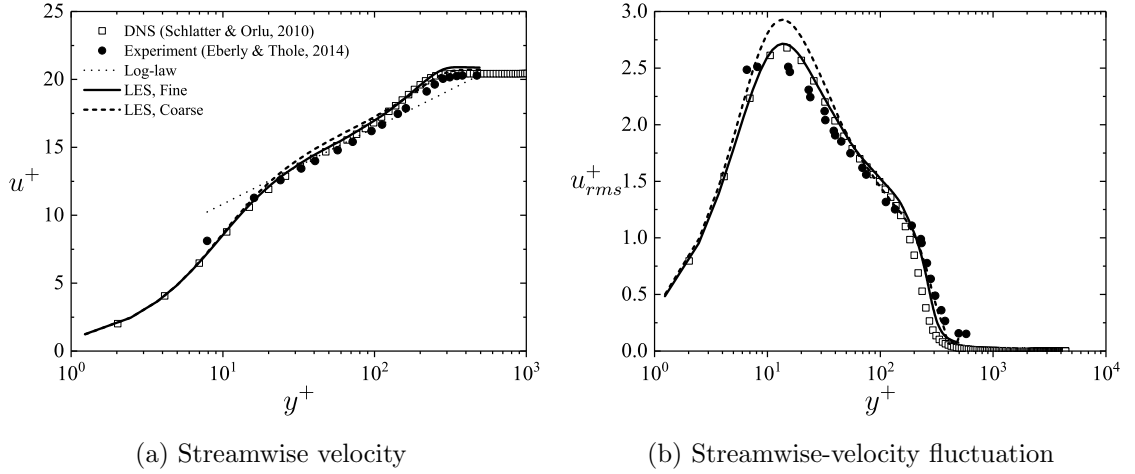


Figure 2.3.: Turbulent boundary layer profiles non-dimensionalized by viscous units at $Re_{\delta_{mom}} = 670$.

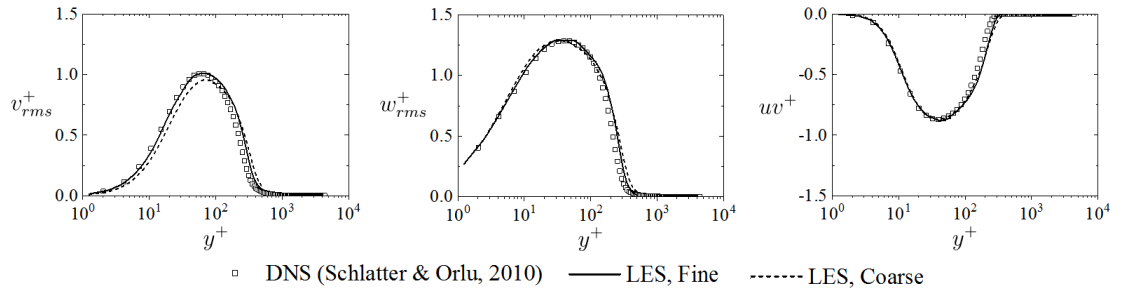


Figure 2.4.: v_{rms}^+ , w_{rms}^+ , and wv^+ profiles at $Re_{\delta_{mom}} = 670$.

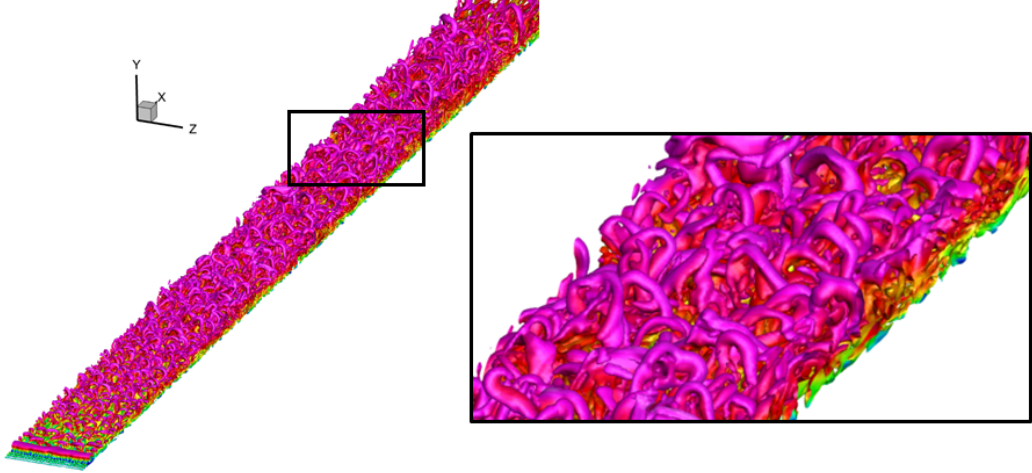


Figure 2.5.: Q-criterion iso-surfaces for a resolved turbulent boundary layer, colored by velocity magnitude.

To further assess the effect of grid resolution, the velocity spectra on the two grids were compared. The data generated is plotted along with Pope’s semi-empirical model of the velocity spectrum for isotropic turbulence [74]. This model agrees well with a range of experimental measurements, notably the turbulent boundary layer data of Saddoughi and Veeravalli [75]. Pope’s model has the form

$$E(\kappa) = C\epsilon^{2/3}\kappa^{-5/3}f_L(\kappa L)f_\ell(\kappa\ell) \quad (2.16)$$

$$f_L(\kappa L) = \left[\frac{\kappa L}{\sqrt{(\kappa L)^2 + c_L}} \right]^{5/3+p_0} \quad (2.17)$$

$$f_\ell(\kappa\ell) = \exp(-\beta[(\kappa\ell)^4 + c_\ell^4]^{1/4} - c_\ell) \quad (2.18)$$

where $C = 1.5$; $p_0 = 2$; $\beta = 5.2$; $\kappa L = \kappa\ell\text{Re}_L^{3/4}$; and ℓ is the Kolmogorov length scale given by $(\nu^3/\epsilon)^{1/4}$. The functions f_L and f_ℓ determine the shape of the energy-containing range and dissipation range, respectively. The constants c_L and c_ℓ are

solved by satisfying the following relations for turbulent kinetic energy and dissipation:

$$k = \int_0^{\infty} E(\kappa) d\kappa \quad (2.19)$$

$$\epsilon = 2\nu \int_0^{\infty} \kappa^2 E(\kappa) d\kappa. \quad (2.20)$$

The model spectrum, in non-dimensional form, can be uniquely determined by a specified turbulent Reynolds number (Re_L) or Taylor microscale Reynolds number (Re_λ), and they are related by $Re_L = k^2/(\epsilon\nu) = 3Re_\lambda^2/20$. The Taylor microscale is estimated from the LES data by using $\lambda = \sqrt{u'^2/(du'/dx)^2}$. Finally, to compare the model spectrum to the LES data, a one-dimensional, longitudinal spectrum is computed by using

$$E_{11}(\kappa_1) = \int_{\kappa_1}^{\infty} \frac{E(\kappa)}{\kappa} \left(1 - \frac{\kappa_1^2}{\kappa^2}\right) d\kappa \quad (2.21)$$

The LES longitudinal spectrum calculation utilizes Taylor's hypothesis to convert frequency to streamwise wavenumber as follows: $\kappa_1 = 2\pi f/U_c$, where U_c is the local velocity. Since this analysis requires relatively isotropic flow, the LES data are probed near the edge of the boundary layer ($Re_{\delta_{mom}} = 670$) at $y^+ = 275$ where $Re_L \approx 210$. Solving the equations above as described gives $c_L = 3.46$ and $c_\ell = 0.44$. The equations are solved in Matlab using 'integral' and 'fsolve' functions; see Appendix A for details. The longitudinal spectrum are compared in Fig. 2.6. Note that Pope's model represents a theoretical DNS result, where all length scales are resolved. As expected, the LES matches Pope's model for the small wavenumbers (large length-scales) and deviates as the dissipation range is approached, representing the unresolved scales. One could calculate the energy resolved by the coarse and fine LES simulations by integrating under the curves and taking the difference between the LES and model results. Doing so shows that the coarse mesh resolves 99.0% of the energy containing eddies, while the fine mesh resolves 99.95%. This suggests that the flow is very well resolved by the LES. Based on these results, the fine mesh resolution is used for all film-cooling LES simulations.

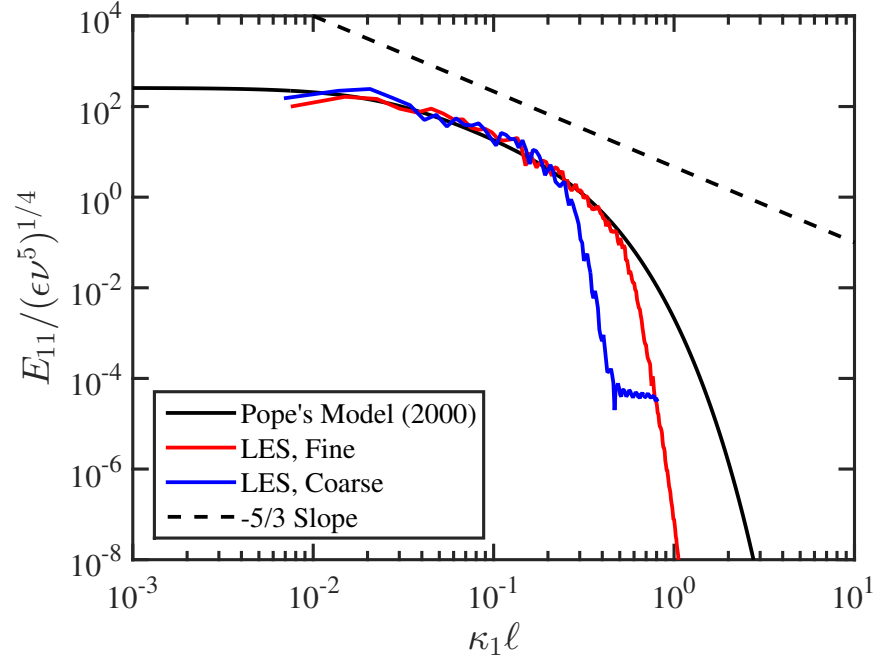


Figure 2.6.: Longitudinal one-dimensional spectrum.

Comparison between the experimental and LES adiabatic effectiveness measurements are seen in Fig. 2.7. This figure shows the adiabatic effectiveness contours on the wall ($y/D = 0$) along with the hole centerline ($z/D = 0$) and laterally-averaged adiabatic effectiveness plots from experiments and LES. In general there is good agreement between the resolved boundary layer cases and the experimental measurements, with both the spreading of the coolant and the trends captured correctly. The experimental results show slightly higher temperatures in the hole and slightly lower temperatures on the uncooled wall which could explain the small discrepancy in centerline adiabatic effectiveness at low BRs. The experiment used a low-conductivity STYROFOAMTM for the adiabatic flat-plate test section and did not apply a conduction correction.

Approximating the inflow as a mean profile is generally unacceptable for lower BRs with excessive spreading of the coolant causing overpredictions of adiabatic effectiveness. However, at higher BRs approximating the inflow as a mean profile has

little impact on the adiabatic effectiveness measurements downstream of the hole. However, note the presence of a cool region curving around the upstream side of the hole. This is due to a horseshoe vortex forming on the upstream side of the hole and entraining coolant; recall Fig. 1.3. This feature will be discussed more in the following sections.

The centerline velocity profiles at $x/D = 3$ and $x/D = 6$ are shown in Fig. 2.8. The experiment used particle image velocimetry to obtain these measurements [38]. These measurements were only made for a round hole inclined at 30° and spacing of $p/D = 6$, which differs slightly from the current study. The figures show good agreement among the range of BR and DR studied. In general the mean boundary layer inflow profile tends to overestimate the streamwise velocity at the edge of the jet.

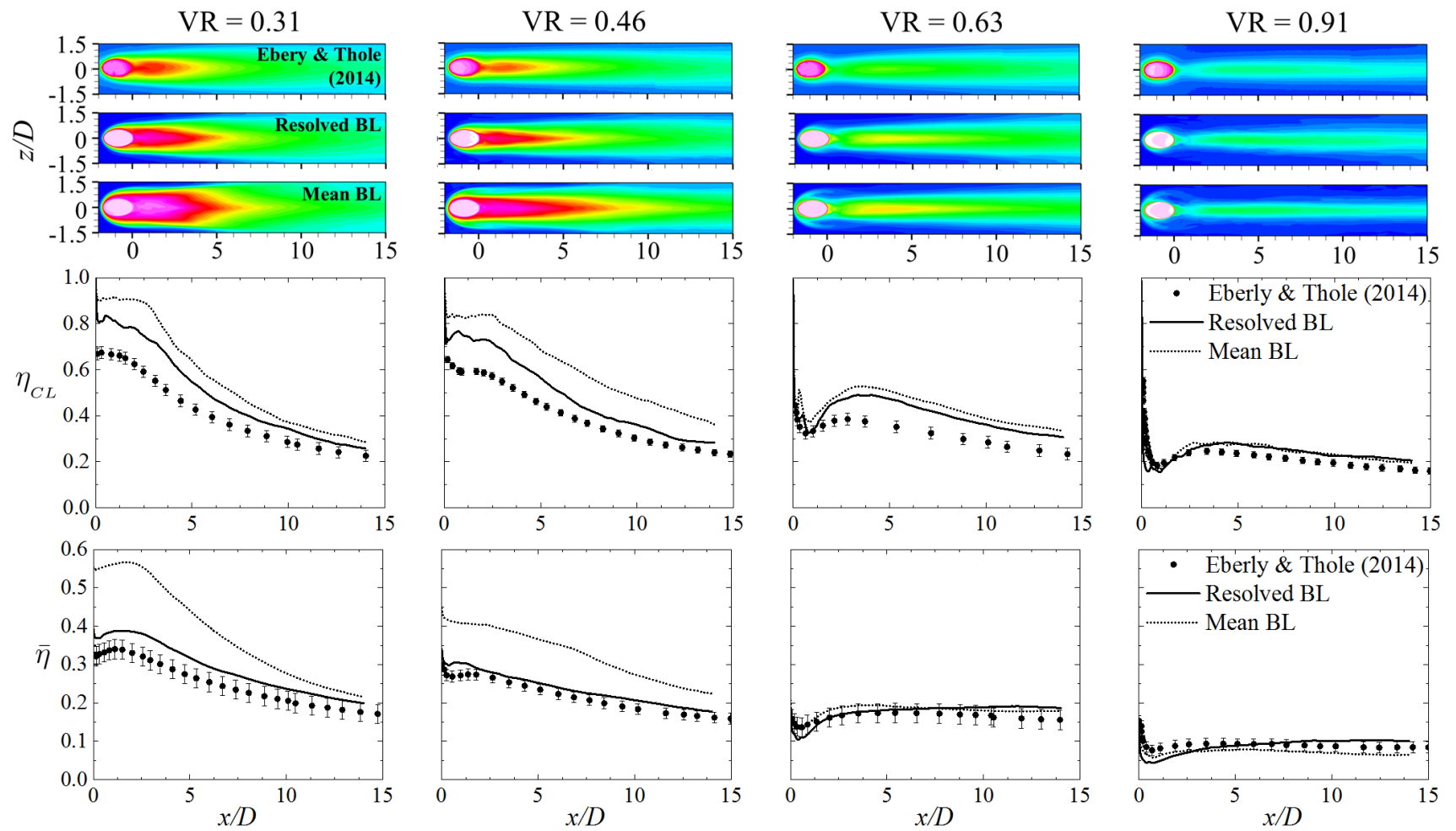


Figure 2.7.: Adiabatic effectiveness measurements.

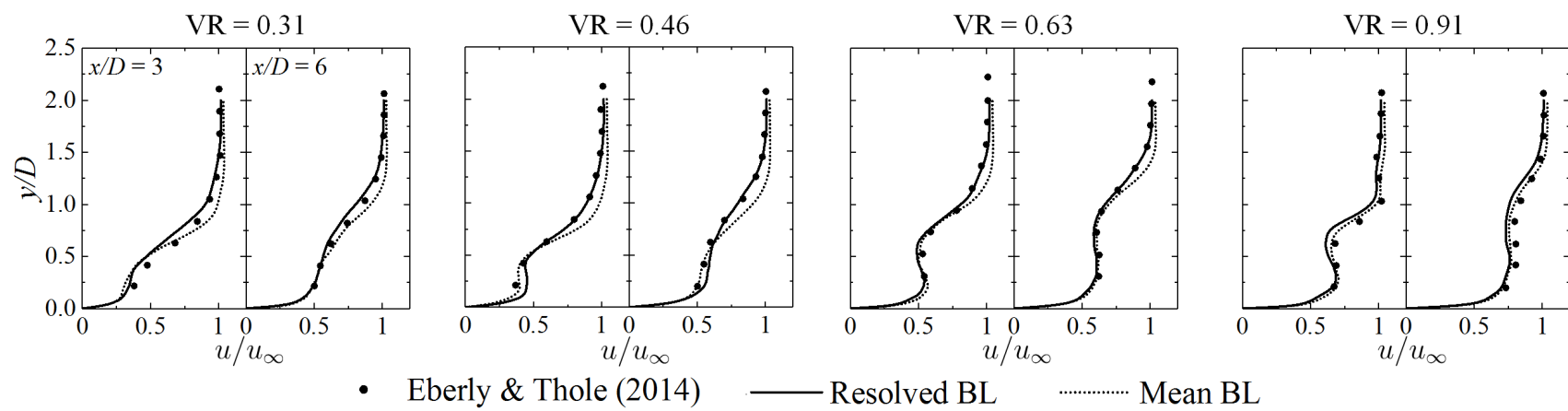


Figure 2.8.: Velocity measurements along centerline ($z/D = 0$).

This validation gives confidence that the physics are represented correctly in this LES study.

2.4.2 Instantaneous Flow Field

This section and the next will focus on the cases in which the spatially developing turbulent boundary layer is resolved. Instantaneous vorticity is visualized in Fig. 2.9 where the the q-criterion iso-surfaces are colored by non-dimensional temperature (θ) and plotted alongside a two-dimensional figure of ω_z . At the lowest VR (low BR/high DR) the vorticity on the upstream side of the hole and the vorticity in the boundary layer have similar magnitudes and meet to form a shear layer between the hot-gas and cool-gas. This shear layer forms clockwise-oriented vortices (blue in the figure) downstream. As the VR increases, the strength of the vorticity in the hole increases and the shear layer exhibits greater instability as hole-vorticity dominates the interaction. At the highest VR (high BR/low DR), the shear layer is overwhelmed by the hole vorticity and counter-clockwise vortices (red in the figure) form downstream of the hole. In Fig. 2.9 while some coherent shear-layer vortices are seen, there is overall lack of clearly defined Kelvin-Helmholtz vortices, this is due to two main factors. The first is the resolved boundary layer upstream of the hole which adds an element of randomness to the eddies in the boundary layer that interact with the jet. The second is the relatively long hole used in this setup ($L/D = 4.7$), this gives the flow that enters the hole time to develop into a sort of turbulent pipe-flow; this can be seen in the Q-criterion iso-surfaces as well as the ω_z figures, where there is a lot of vorticity in the hole on the upstream side. These two factors contribute to turbulent mixing that makes it difficult to see clean coherent structures.

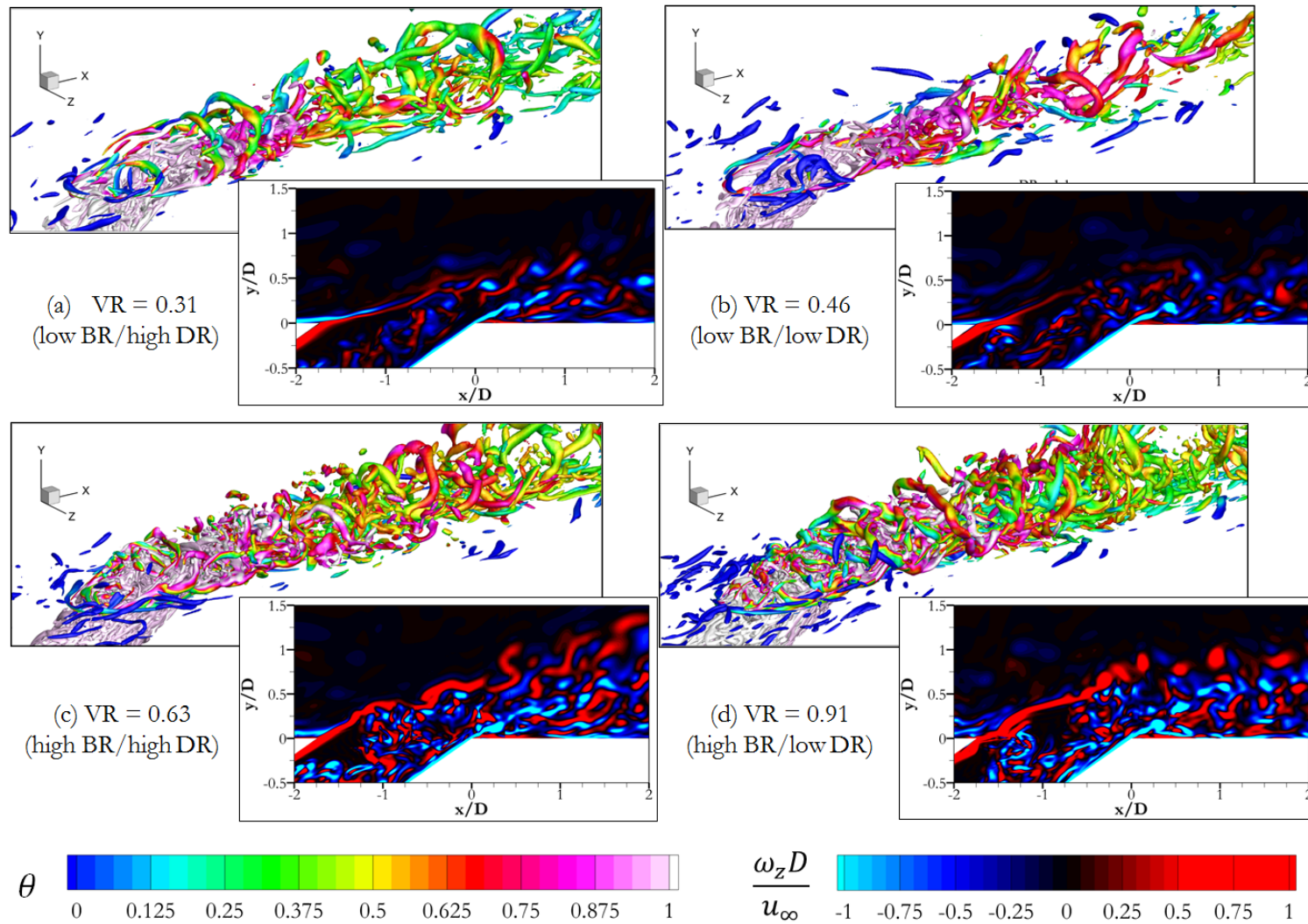
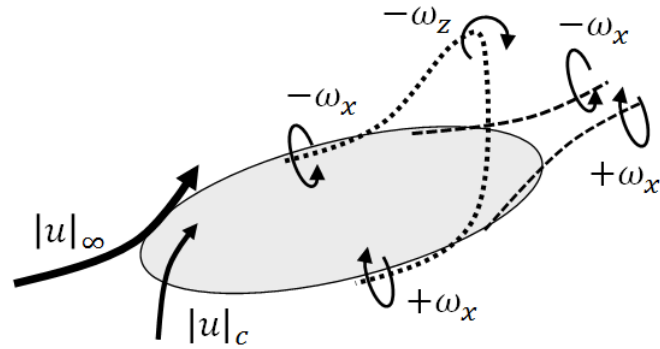
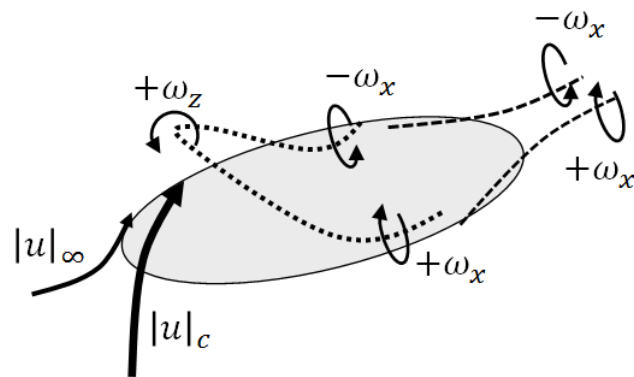


Figure 2.9.: Q-criterion colored by θ with 2-D contour of ω_z . a) Case 1; b) Case 2; c) Case 3; d) Case 4.



(a) low VR



(b) high VR

Figure 2.10.: Sketch of flow structure near the hole. a) low VR; b) high VR.

To better visualize the change in the shear layer vorticity as VR changes, a sketch of the vortices are provided in Fig. 2.10. At low VR the velocities in the crossflow and jet meet such that a clock-wise oriented vortex results. This is a three-dimensional structure that resembles a hairpin vortex where the legs originate from the sides of the hole, where the dominant vorticity is $\pm\omega_x$. There is a bifurcation in this x -vorticity with part of it energizing the legs of the hairpin structure and part of it feeding the CRVP. At higher VR the velocities in the crossflow and jet meet such that a counter-clockwise vortex results which again forms a hairpin structure, but with the head trailing the legs. The impact of this reversal in vorticity on the time-averaged statistics will be evaluated in the following section.

The non-dimensional temperature, just above the wall, is plotted in Fig. 2.11. The trends in this figure match what would be expected based on Fig. 2.7, as well as previous studies, with higher DR at a fixed BR resulting in better spreading of the jet and better cooling; it can also be said that cooling tends to decrease as VR increases. At the lowest VR it can be seen that the vorticity that originates from the sides of the hole is shed periodically and carries cool fluid with it which is seen as small lobes of coolant in the contour plot. As the VR increases coolant tends to leave the hole asymmetrically (Fig. 2.11c). At higher VRs the lift-off of the jet is significant, but the vorticity still traps coolant close to the wall.

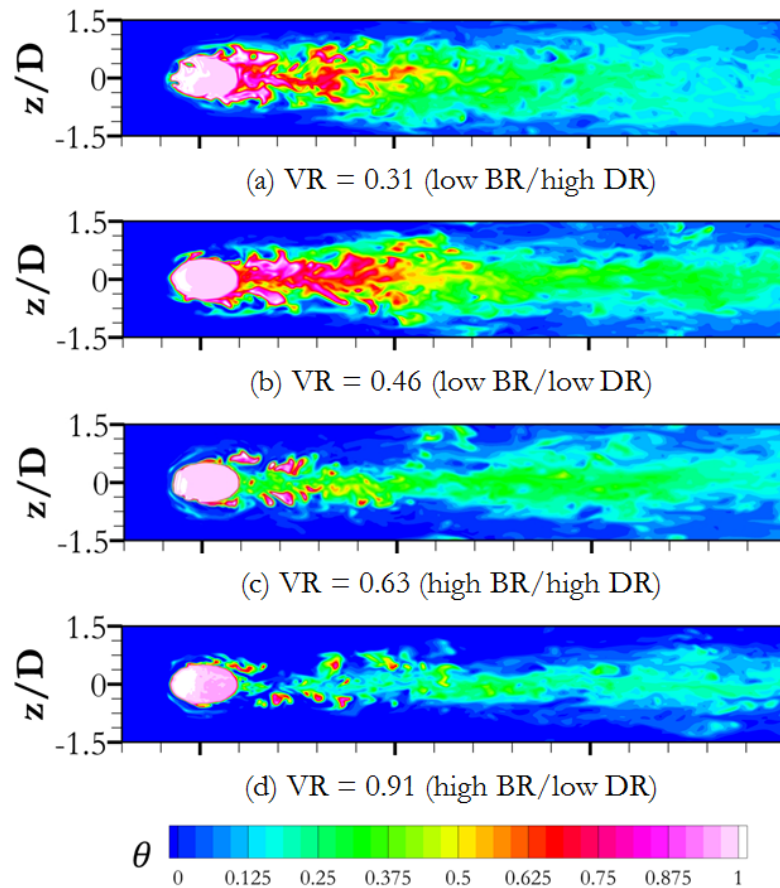


Figure 2.11.: Instantaneous non-dimensional temperature at $y/D = 0.05$. a) case 1; b) case 2; c) case 3; d) case 4.

2.4.3 Time-Averaged Flow Field

Figure 2.12 shows the time-averaged non-dimensional temperature of the jet at two locations downstream of the hole. The contour lines of ω_x are superimposed on the temperature to visualize the CRVP. The lighter ($-\omega_x$) or darker ($+\omega_x$) the contour lines, then the stronger the vorticity; additionally more contour lines relative to another figure, indicates stronger vorticity. At the lowest VR the coolant spread is greatest, with small tails of coolant sticking to the walls at $x/D = 2$. As VR increases, these tails disappear and the temperature profile is more rounded. This is due to the strengthening CRVP entraining more hot gas from the crossflow, evidenced by increasing x -vorticity near the wall. The CRVP induces a z -velocity towards the middle of the jet which creates this shear layer on the flat plate underneath the CRVP. As VR continues to increase the jet exhibits significant lift-off and more hot gas is entrained, seen in the reduced θ at $z/D = 0$. Again, this increasing entrainment with increasing VR is due to the strengthening CRVP. Since the CRVP originates from the vorticity in the hole (as seen in Figs. 2.9 and 2.10), the coolant is at the core of the CRVP. Finally, these figures show how quickly the CRVP loses strength downstream from $x/D = 0.5$ to $x/D = 2$.

Understanding how the turbulence, in particular the Reynolds stresses and turbulent heat flux, scales with VR (BR/DR) can provide insight into designing better film cooling as well as guidance on improving existing turbulence models. The turbulent statistics can also help in understanding how the time-dependent flow physics are manifested in the time-averaged flow field. The Favre-averaged Reynolds normal stresses ($\widetilde{u''u''}$, $\widetilde{v''v''}$, $\widetilde{w''w''}$) are plotted in Fig. 2.13. At the lowest VR the $\widetilde{u''u''}$ profile is relatively wide with a large magnitude in the shear layer between the jet and crossflow. As VR increases, this profile is constricted towards the center of the jet with a noticeable decrease in magnitude near the wall. This turbulent energy near the wall helps to keep the coolant attached and is one reason why the tails of coolant in Fig. 2.12a are no longer present in Fig. 2.12b. When VR further increases

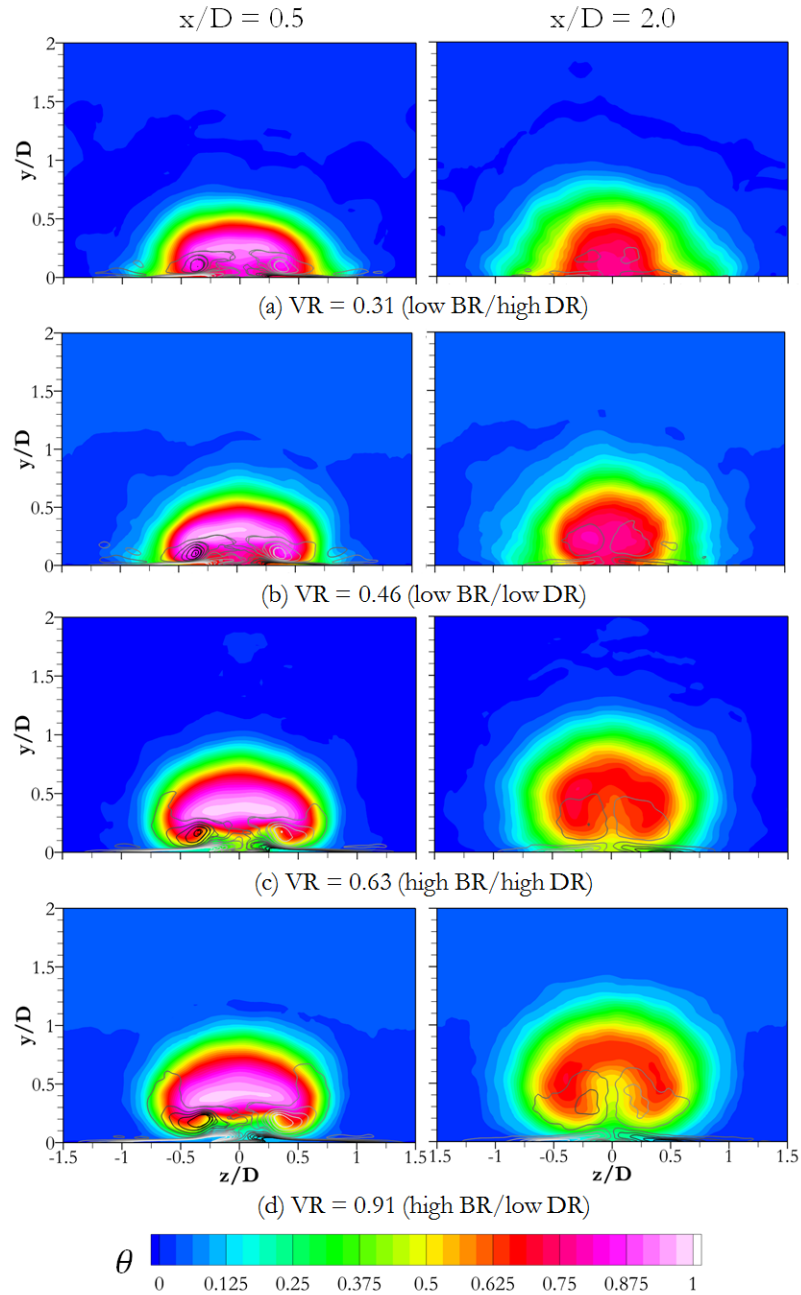


Figure 2.12.: Time-averaged non-dimensional temperature with ω_x contour lines at $x/D = 0.5$ and 2. a) case 1; b) case 2; c) case 3; d) case 4.

the magnitude of $\widetilde{u''u''}$ in the middle of the jet continues to increase; however, the slight magnitude decrease from Fig. 2.13b to Fig. 2.13c can be attributed to the

x -velocities between the upstream side of the jet and crossflow boundary layer being closely matched. A similar trend is seen in $\widetilde{v''v''}$, where the profile both constricts and grows in magnitude as VR increases. In $\widetilde{w''w''}$, at the lowest VR, there are two distinct regions where z -velocity fluctuations are highest, which correspond to the lateral sides of the jet. As VR increases there is again a constriction of the profile and a growth in the magnitude of the stress under the jet at $z/D = 0$. This magnitude increase under the jet corresponds to the increase in strength of the CRVP, and as expected it continues to increase with VR. This figure shows that the Reynolds normal stresses in film-cooling scale with VR.

The Favre-averaged Reynolds shear stresses ($\widetilde{u''v''}$, $\widetilde{u''w''}$, $\widetilde{v''w''}$) are plotted in Fig. 2.14. At the lowest VR, $\widetilde{u''v''}$ is positively correlated under the jet at the wall and negatively correlated in the shear layer between the jet and crossflow. As the VR increases, the positive correlation lifts up at $z/D = 0$ in accordance with a strengthening CRVP. Also, as was seen in the normal stresses, the weakening negative correlation in the shear layer between Fig. 2.14b and Fig. 2.14c is due to similar x -velocities where the crossflow and jet meet. Interestingly, at the highest VR, $\widetilde{u''v''}$ becomes positive on top of the jet as well as a clear negative region under the jet nearest the wall. This is the result of the change in vorticity that was highlighted in Figs. 2.9 and 2.10. In $\widetilde{u''w''}$ it is evident that there are large z -velocity fluctuations towards the center of the jet as flow is entrained by the CRVP. At low VRs the magnitude is low, with a relatively wide profile, as the VR continues to increase the magnitude also increases. At the highest VR, the magnitude at the wall is highest, but there is also very strong correlations within the jet itself at $y/D \approx 1$ and opposite correlations on the lateral edges of the jet. Finally, $\widetilde{v''w''}$ is also related to the motion of the CRVP with the y -velocity and z -velocity fluctuations being correlated with flow going up towards the jet and in towards the center of the jet, then down towards the wall and out towards the edge of the jet. Both the $\widetilde{u''w''}$ and $\widetilde{v''w''}$ stresses are linked to the spreading of the jet, but note that the magnitudes are different; if these magnitude differences are not captured in turbulence models then entrainment

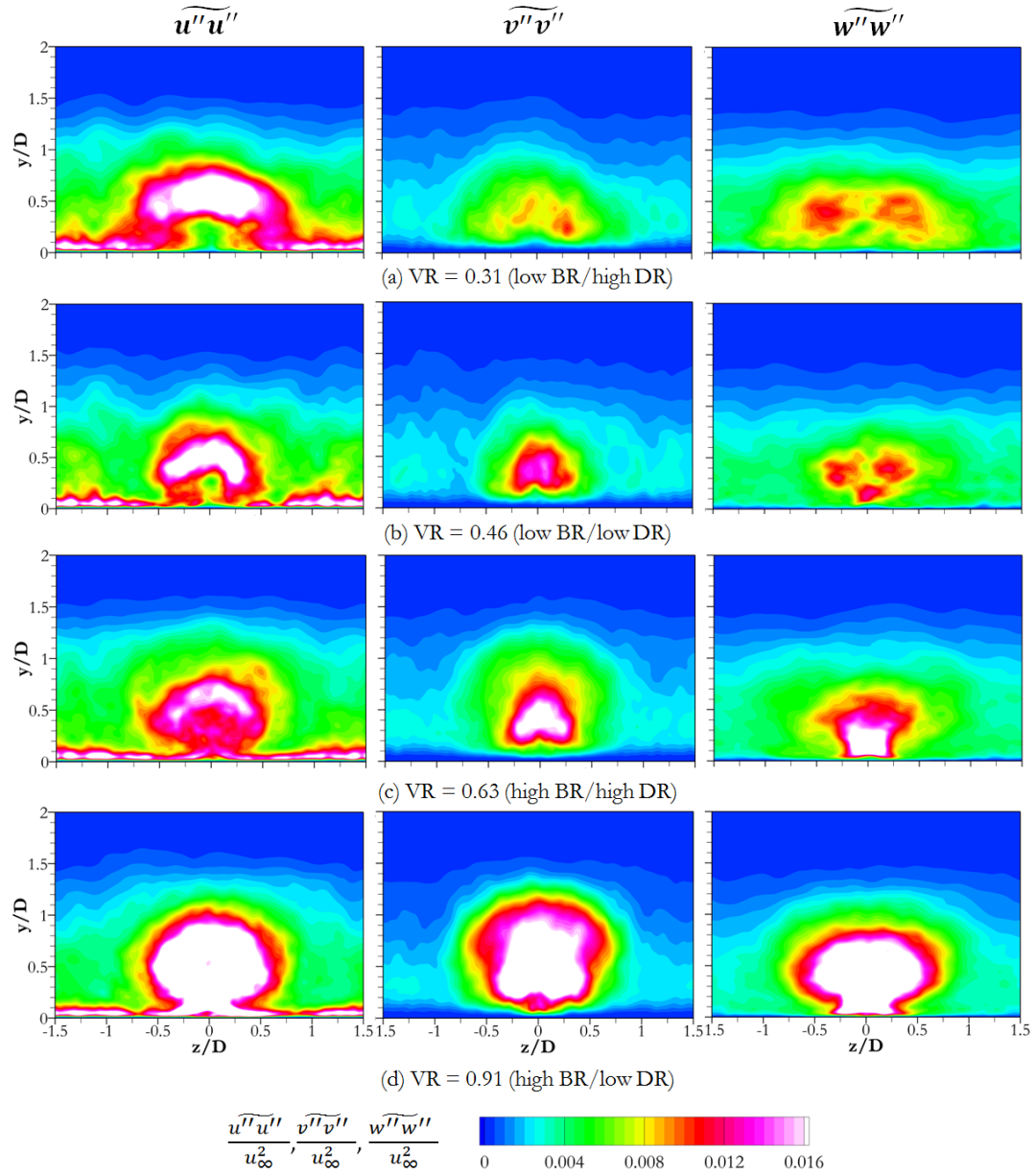


Figure 2.13.: Favre-averaged non-dimensional Reynolds normal stresses at $x/D = 2$.
 a) case 1; b) case 2; c) case 3; d) case 4.

and spreading of the jet will not be predicted correctly. The trend in these shear stresses also indicates that VR is an important parameter in predicting film-cooling performance since large changes in the turbulence are seen to take place at the same BR (Figs. 2.14c and 2.14d). Indeed, higher VRs show increases in turbulent mixing

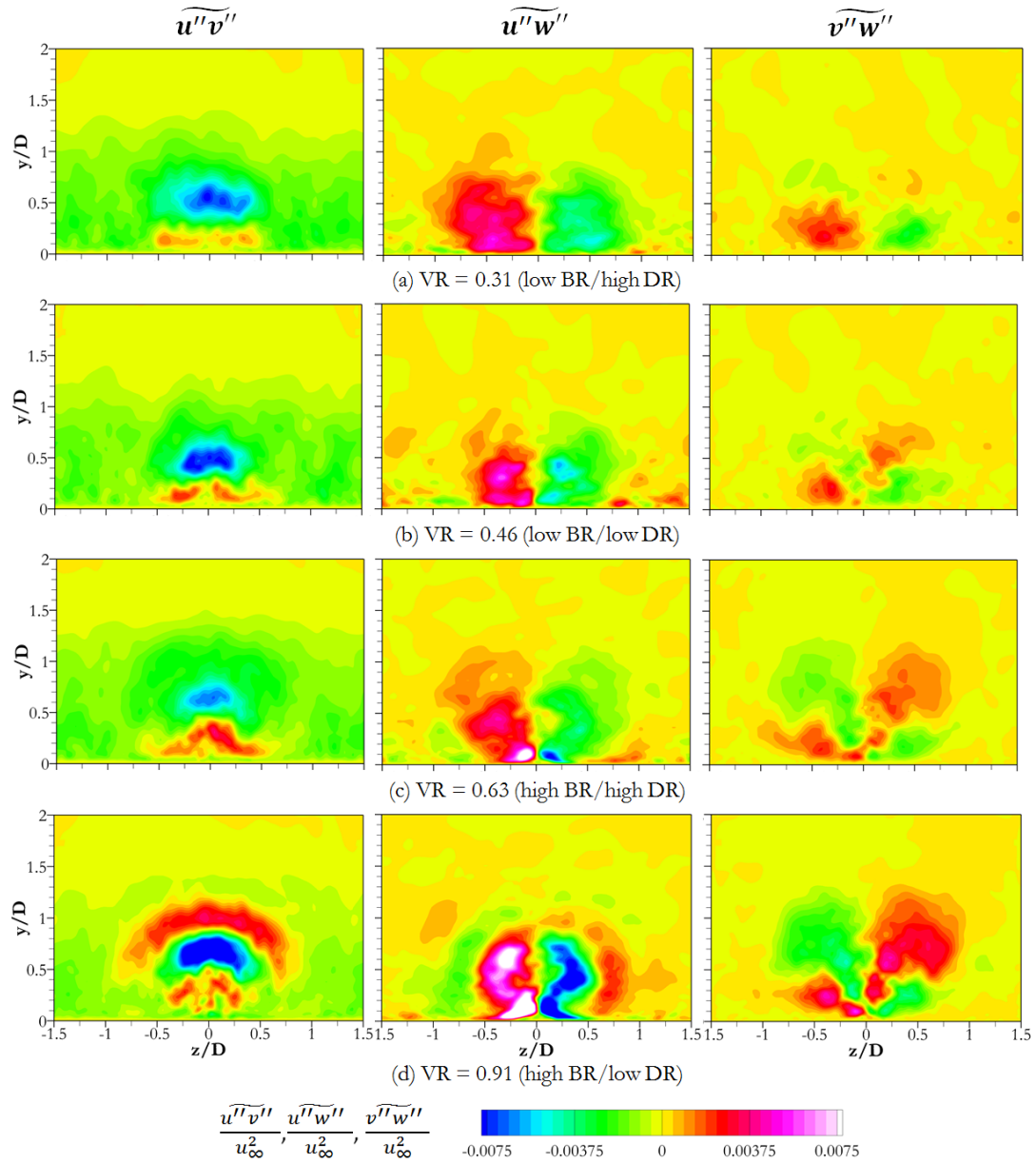


Figure 2.14.: Favre-averaged non-dimensional Reynolds shear stresses at $x/D = 2$.
 a) case 1; b) case 2; c) case 3; d) case 4.

(seen as increases in the Reynolds stress magnitudes) directly under the jet and this directly correlates with lower adiabatic effectiveness measurements (Fig. 2.7).

The Favre-averaged non-dimensional turbulent heat fluxes ($\widetilde{u''\theta''}$, $\widetilde{v''\theta''}$, $\widetilde{w''\theta''}$) are plotted in Fig. 2.15. The turbulent heat flux gives the direction and magni-

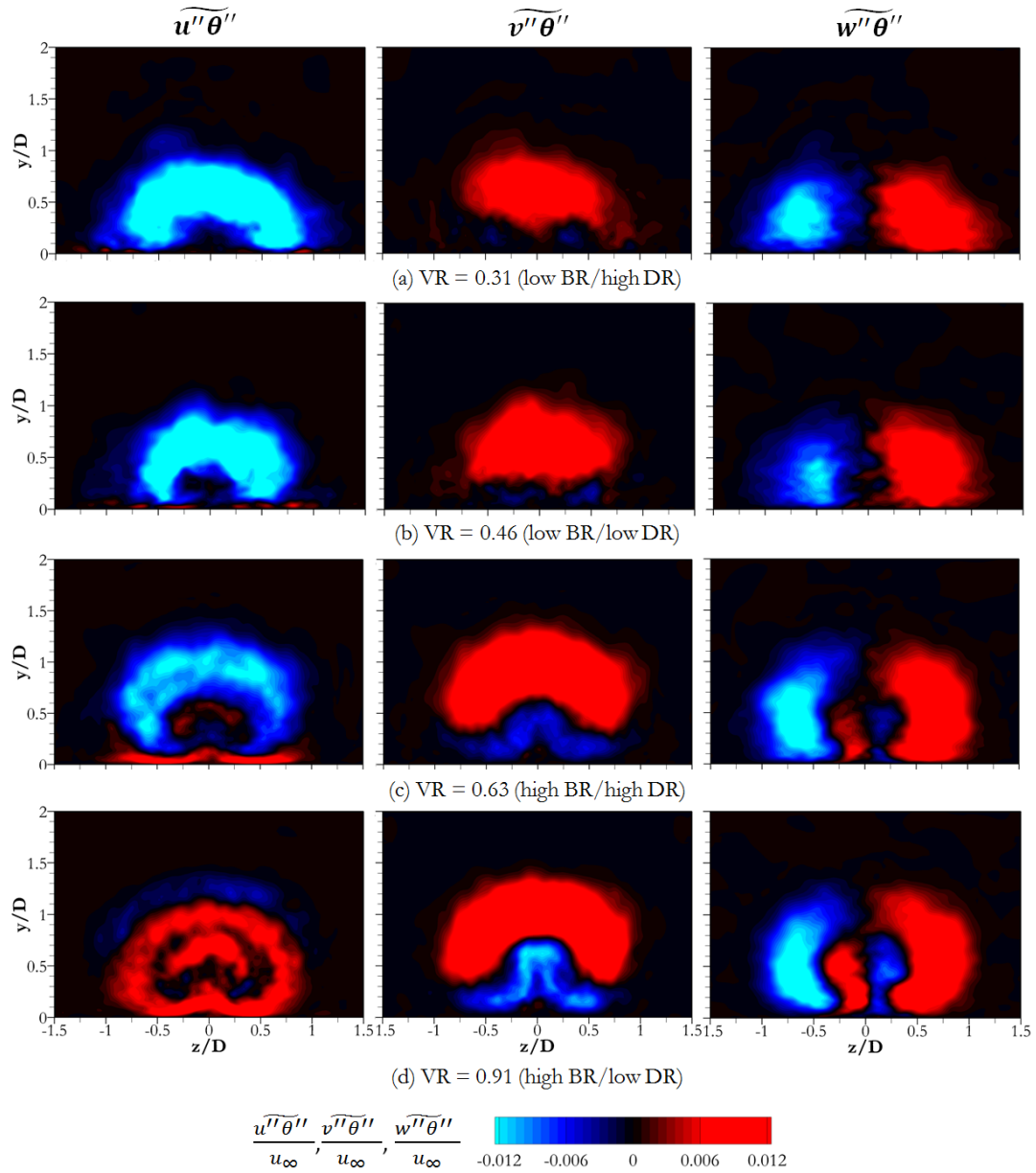


Figure 2.15.: Favre-averaged non-dimensional turbulent heat fluxes at $x/D = 2$. a) case 1; b) case 2; c) case 3; d) case 4.

tude of the turbulent transport of temperature. Note that the temperature is non-dimensionalized such that $\theta = 1$ in the cool gas. At low VRs, $\widetilde{u''\theta''}$ is negative in the shear layer between the jet and crossflow, with a small positive region near the wall. This positive region grows as VR increases because more hot-gas is entrained. Like

other correlations involving x -velocity, there is a decrease in the negative correlation as the crossflow and jet velocities become matched at the interface. At the highest VR there is again a very abrupt change in the turbulence, where $\widetilde{u''\theta''}$ becomes positive in the majority of the jet with only a small negative region in the shear layer on top of the jet. This phenomena is attributed to the large-scale interaction between the shear layer vortices (Figs. 2.9d and 2.10b) and the strong CRVP. The $\widetilde{v''\theta''}$ flux shows that turbulence transports the hot-gas into the jet mainly through the shear layer at low VRs. As more lift off occurs and the CRVP becomes stronger at higher VRs this transport occurs on all sides of the jet. A similar trend is seen in the $\widetilde{w''\theta''}$ flux, where the lateral sides of the jet exhibit enhanced turbulent heat transfer at low VRs. At higher VRs heat is transferred through both the sides and middle of the jet as the CRVP brings hot-gas to the middle.

2.4.4 Mean Boundary Layer vs. Resolved Turbulent Boundary Layer

The adiabatic effectiveness for the mean and resolved boundary layers were plotted in Fig. 2.7. The trend in these plots showed that at $BR = 0.5$ the mean boundary layer overestimated the cooling, and at $BR = 1$ it had little to no effect on the cooling performance. One consequence of using a mean boundary layer is the formation of a horseshoe vortex on the upstream side of the hole that wraps around the jet. This vortex entrains coolant and spreads it over the plate, which can be seen clearly at $BR = 1$ in Fig. 2.7. The non-dimensional temperature is plotted in Fig. 2.16 which shows the effect of the boundary layer at high and low VRs. At the low VR there is a significant increase in spreading, with the horseshoe vortex structure helping to pull cool fluid from the jet, out towards the wall. With a turbulent boundary layer there is unsteady flow hitting the jet, in turn, a coherent horseshoe vortex is not formed. Figure. 2.17 demonstrates this concept clearly, where the horseshoe vortex wrapping around the hole in Fig. 2.17a disappears in Fig. 2.17b. Additionally, the turbulence enhances mixing at the edges of the jet, reducing the spread of the coolant. At the

high VR there is very little change in the temperature profile when a mean boundary layer is used versus a resolved turbulent boundary layer. Noticeably, the horseshoe vortex is not seen at $x/D = 2$, this is because it is much weaker than the CRVP at this VR and is actually entrained by the jet; Fig. 2.7 shows some evidence of this, as the coolant entrained by the horseshoe vortex curves towards the jet.

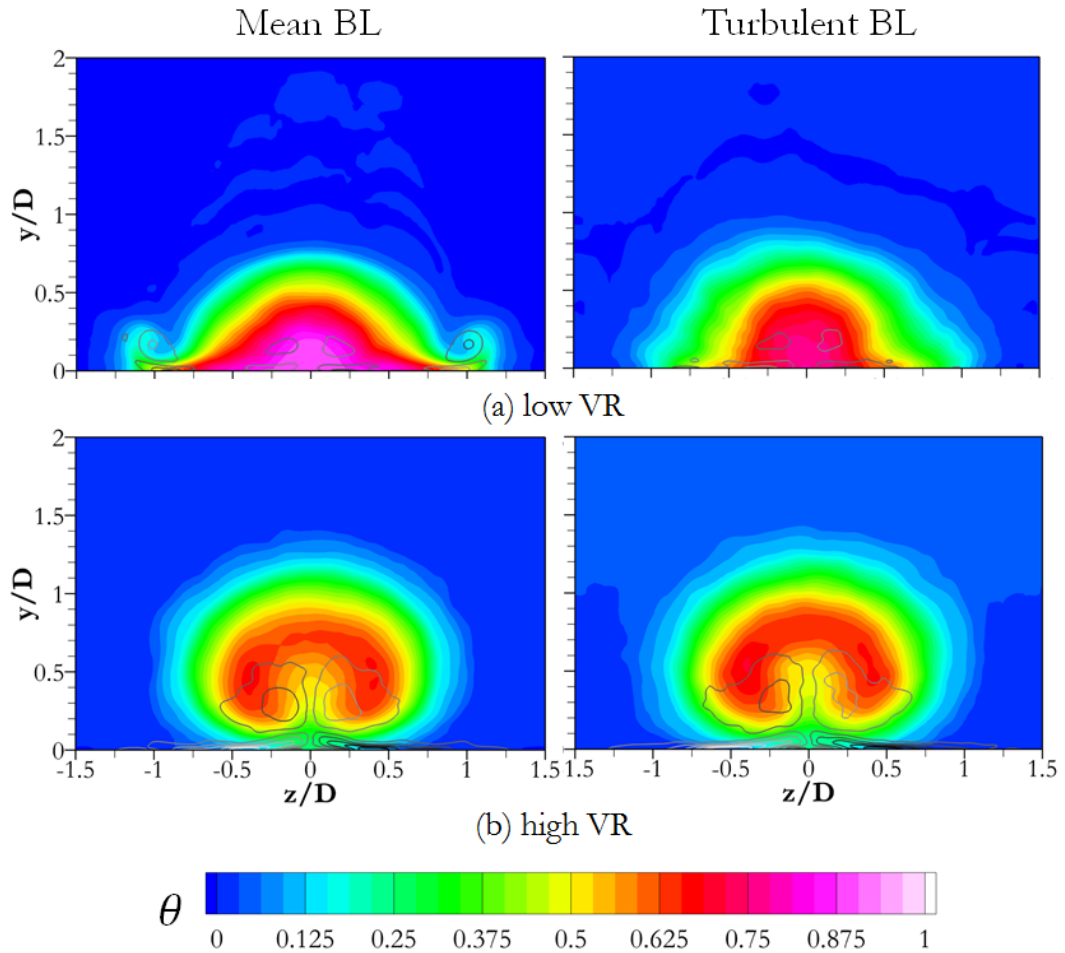
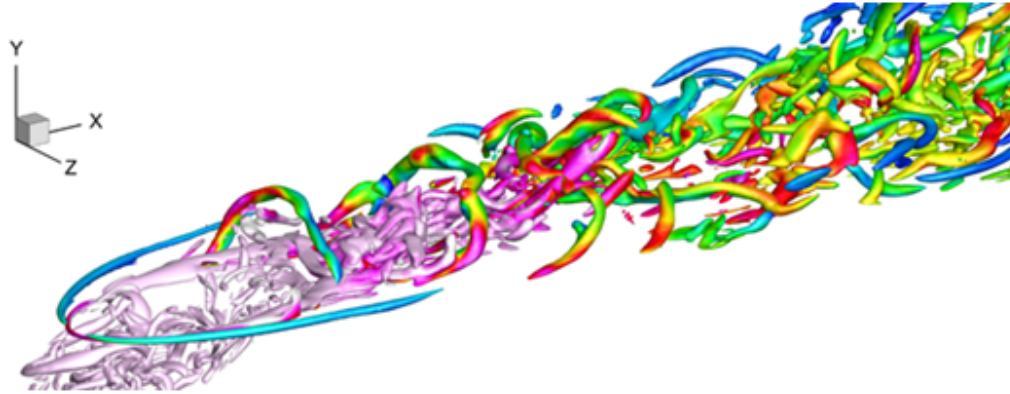
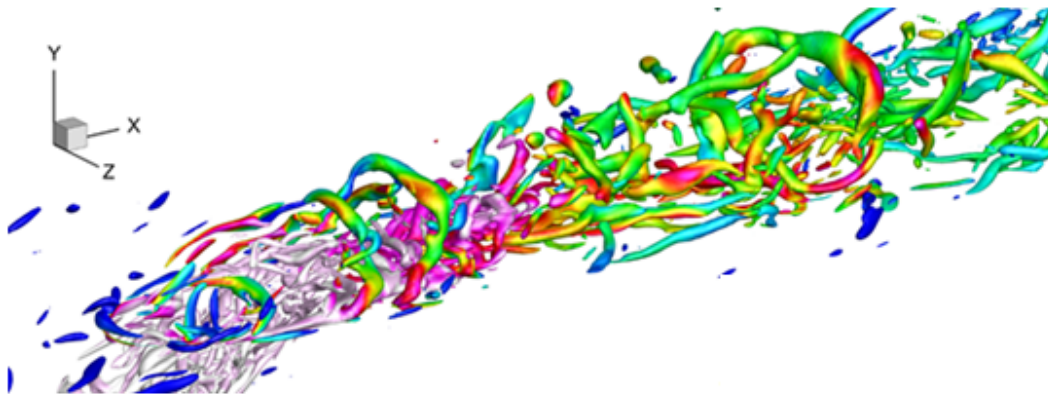


Figure 2.16.: Time-averaged non-dimensional temperature with ω_x contour lines at $x/D = 2$ for a mean and turbulent boundary layer. a) cases 1 and 5; b) cases 4 and 8.

To get a better sense of the impact of the turbulence, the turbulent kinetic energy (k) is plotted in Fig. 2.18 which shows the effect of the boundary layer at high and



(a) Mean boundary layer



(b) Resolved turbulent boundary layer

Figure 2.17.: Q-criterion iso-surfaces, colored by θ , for $VR = 0.31$ (cases 1 and 5).

low VRs. This figure shows there is no turbulent kinetic energy in the boundary layer, so at the low VR the energy in the horseshoe vortex is seen clearly. However, the magnitude of k in the horseshoe vortex, as well as the edge of the jet, is similar to that of the boundary layer so these relatively weak structures get overwhelmed by the turbulent energy in the boundary layer. Additionally, the increase in k in the shear layer indicates more turbulent mixing. At the high VR, with a mean boundary layer, the high k at the wall is associated with the the entrainment of the horseshoe vortex. With a turbulent boundary layer, the horseshoe vortex does not form, and thus this region of high k near the wall is no longer present. Additionally at the

high VR, the jet itself contains so much turbulent energy that it is not affected by the relatively weak turbulence in the boundary layer. This results in the resolved turbulent boundary having little impact on the cooling performance.

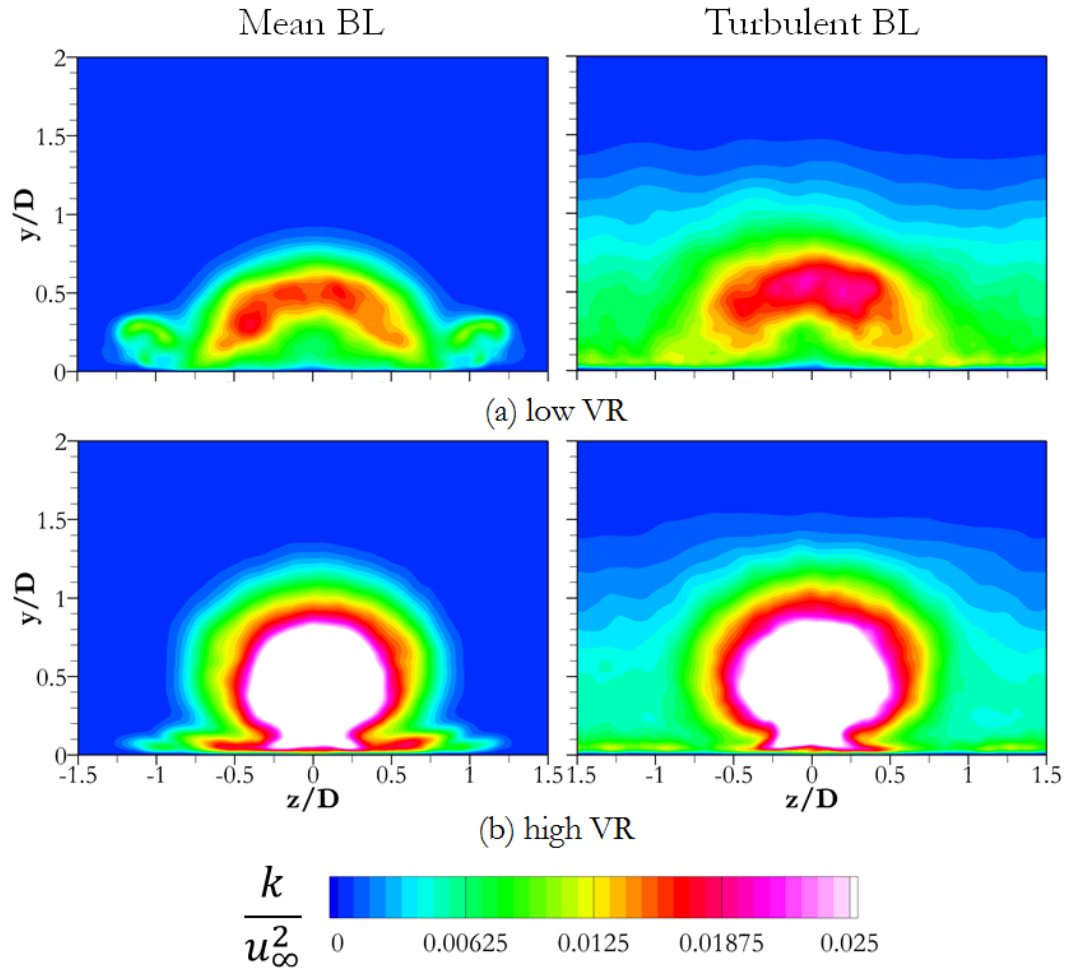


Figure 2.18.: Non-dimensional turbulent kinetic energy at $x/D = 2$. a) cases 1 and 5; b) cases 4 and 8.

Resolving the unsteady turbulent boundary layer is the best approach for replicating realistic film-cooling flows. However, this can be computationally expensive and additional work is required to set up the boundary layer trip with the correct strength and location. This study shows that approximating the boundary layer with just a mean boundary layer profile, such as a $1/7^{th}$ power-law profile, without any

imposed turbulence may be sufficient for predicting the adiabatic effectiveness for $VR > 0.6$. However, for lower VRs the turbulence in the boundary layer is required to get accurate cooling predictions.

2.5 Summary

An LES study was performed to understand the effects of DR and BR on the turbulent structure and effectiveness for film cooling of a flat plate through round holes. Additionally, the effect of the inlet boundary condition is evaluated. The adiabatic effectiveness and velocity profiles were validated against experimental measurements. Good agreement was found between the LES simulations employing a resolved turbulent boundary layer, whereas the LES simulations with a mean profile exhibited good agreement at high VRs, but tended to overestimate cooling at low VRs.

The instantaneous flow results showed how the shear layer between the jet and crossflow became more unstable as the VR increased. At a low VR the shear layer vortex exhibited a negative z -vorticity, while a high VR showed a positive z -vorticity. The impact of this change in vorticity manifested itself most noticeably in the $\widetilde{u''v''}$ and $\widetilde{u''\theta''}$ statistics, which highlight a shift in the nature of the large-scale mixing.

Analysis of the non-dimensional temperature, vorticity, Reynolds stresses, and turbulent heat flux reveal that the strength of the CRVP and turbulent mixing scales with VR. Increasing DR at a fixed BR is effectively reducing the VR. Consequently, the CRVP and turbulent mixing weakens resulting in less entrainment of hot crossflow gas and higher film-cooling effectiveness.

The effect of a mean boundary layer versus a resolved turbulent boundary layer was investigated. At low VR it was found that the horseshoe vortex that forms in the mean boundary layer cases helps to pull cool fluid from the jet outwards toward the wall. The unsteadiness in a resolved turbulent boundary layer inhibits the formation of a horseshoe vortex and the increased mixing reduces the spreading of the coolant. At a high VR it was found that the horseshoe vortex forms for a mean

boundary layer, but it gets entrained into the jet and does not enhance the cooling performance. The relatively low turbulent kinetic energy in the jet at a low VR tends to become enhanced in the presence of a resolved turbulent boundary layer, while at a high VR the jet is already quite energetic and tends not to be affected by the turbulent boundary layer. In general, both a mean and resolved turbulent boundary layer provide sufficient cooling predictions at $VR > 0.6$, but at low VRs the upstream boundary layer should be resolved to accurately predict the cooling performance.

3. IDENTIFYING WEAKNESSES IN EDDY-VISCOSITY MODELS FOR PREDICTING FILM COOLING BY MEANS OF LARGE-EDDY SIMULATION

In this chapter, the LES and RANS results are presented that address the third objective. First, the film-cooling problem is described. Next, the governing equations, numerical method, and setup for RANS are presented. Finally, the simulation results including verification and validation, thermal and turbulent flow field, and analysis of the Boussinesq and gradient-diffusion hypotheses are shown. Parts of this chapter are adapted from the journal publication by Stratton and Shih [76].

3.1 Problem Description

The problem studied is identical to that studied by LES in Chapter 2, it is shown in Fig. 3.1. It consists of a flat plate film cooled by jets issuing from a plenum through one row of circular holes. Each hole has diameter, $D = 2.6$ mm, and length, $L = 4.7D$, and is inclined at 35° with respect to the plate. The holes along the row are spaced $3D$ apart.

The turbulent boundary layer, measured $5D$ upstream of the hole, has a boundary layer thickness of $\delta = 1.2D$ and momentum thickness of $\delta_{mom} = 0.13D$, which corresponds to a $Re_{\delta_{mom}} = 670$. The LES results used in this chapter correspond to those with a resolved turbulent boundary layer. The RANS cases use either the realizable k - ϵ or k - ω SST turbulence models. A summary of cases studied is given in Table 3.1.

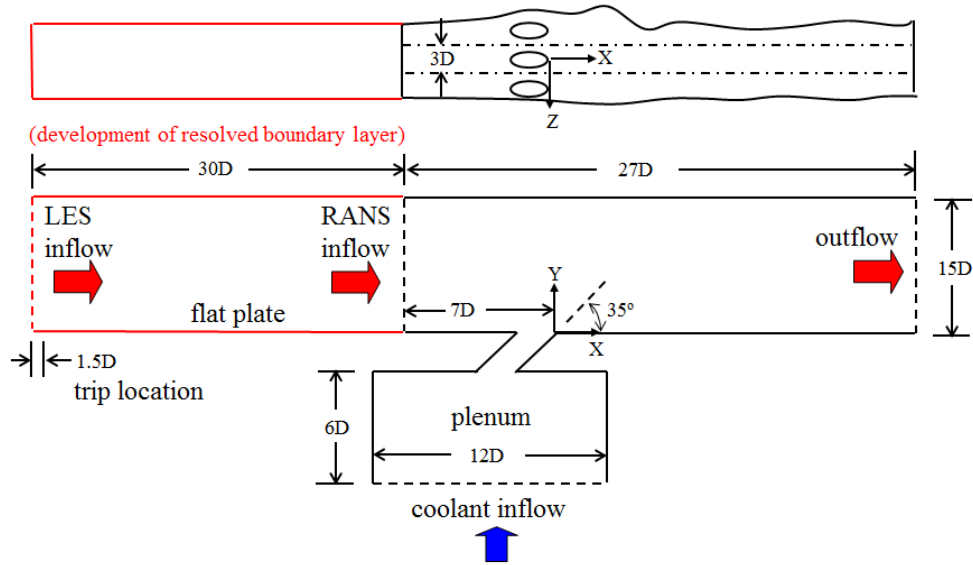


Figure 3.1.: Computational model.

Table 3.1.: Summary of cases.

Case	Turbulence Model	DR	BR	VR	MR	$T_c(K)$	$T_\infty(K)$
1	Realizable $k-\epsilon$	1.6	0.5	0.313	0.156	203	329
2	Realizable $k-\epsilon$	1.1	0.5	0.455	0.227	269	296
3	Realizable $k-\epsilon$	1.6	1.0	0.625	0.625	203	329
4	Realizable $k-\epsilon$	1.1	1.0	0.909	0.909	269	296
5	$k-\omega$ SST	1.6	0.5	0.313	0.156	203	329
6	$k-\omega$ SST	1.1	0.5	0.455	0.227	269	296
7	$k-\omega$ SST	1.6	1.0	0.625	0.625	203	329
8	$k-\omega$ SST	1.1	1.0	0.909	0.909	269	296

3.2 Governing Equations

For the RANS simulations, the governing equations are the Favre-averaged (density-weighted) continuity, momentum (Navier-Stokes), and total energy equations. Favre-

averaging is used because the flow is compressible due to the large temperature variations in the flow field. The Favre-averaged flow variables are denoted by a tilde. For instance, $\tilde{u}_i = \overline{\rho u_i} / \bar{\rho}$, where the overbar denotes the Reynolds average [77]. The Favre-averaged equations used are as follows:

$$\frac{\partial \bar{\rho}}{\partial t} + \frac{\partial}{\partial x_i} (\bar{\rho} \tilde{u}_i) = 0 \quad (3.1)$$

$$\frac{\partial}{\partial t} (\bar{\rho} \tilde{u}_i) + \frac{\partial}{\partial x_j} (\bar{\rho} \tilde{u}_j \tilde{u}_i) = -\frac{\partial p}{\partial x_i} + \frac{\partial}{\partial x_j} [\bar{t}_{ji} - \overline{\rho u_j'' u_i''}] \quad (3.2)$$

$$\begin{aligned} \frac{\partial}{\partial t} \left[\bar{\rho} \left(\tilde{e} + \frac{\tilde{u}_i \tilde{u}_i}{2} \right) + \frac{\overline{\rho u_i'' u_i''}}{2} \right] + \frac{\partial}{\partial x_j} \left[\bar{\rho} \tilde{u}_j \left(\tilde{h} + \frac{\tilde{u}_i \tilde{u}_i}{2} \right) + \tilde{u}_j \frac{\overline{\rho u_i'' u_i''}}{2} \right] \\ = \frac{\partial}{\partial x_j} \left[-q_{Lj} - \overline{\rho u_j'' h''} + \bar{t}_{ji} u_i'' - \overline{\rho u_j'' \frac{1}{2} u_i'' u_i''} \right] \\ + \frac{\partial}{\partial x_j} [\tilde{u}_i (\bar{t}_{ij} - \overline{\rho u_j'' u_i''})] \end{aligned} \quad (3.3)$$

In the above equations, $q_{Lj} = -\frac{\mu}{Pr} \frac{\partial h}{\partial x_j}$ is the laminar heat-flux vector; $h = c_p T$ is the specific enthalpy; and $\bar{t}_{ij} = 2\mu S_{ij} - \frac{2}{3}\mu \frac{\partial \tilde{u}_k}{\partial x_k} \delta_{ij}$ is the viscous stress tensor where $S_{ij} = \frac{1}{2} \left(\frac{\partial \tilde{u}_i}{\partial x_j} + \frac{\partial \tilde{u}_j}{\partial x_i} \right)$ is the strain rate tensor. Pressure, density and temperature were related by the thermally perfect gas law, $p = \bar{\rho} R \tilde{T}$. Sutherland's law was used for viscosity, and Stokes hypothesis for bulk viscosity was assumed.

The Favre-averaged equations require models for the Reynolds stresses, the turbulent heat flux, the turbulent diffusion, and the turbulent transport terms. The Reynolds stress is modeled by the Boussinesq hypothesis given by

$$\widetilde{u_i'' u_j''} = -2\nu_t \left(S_{ij} - \frac{1}{3} \frac{\partial \tilde{u}_k}{\partial x_k} \delta_{ij} \right) + \frac{2}{3} k \delta_{ij} \quad (3.4)$$

where ν_t is the eddy viscosity and k is the turbulent kinetic energy. The turbulent heat flux, turbulent diffusion, and turbulent transport terms are modeled with forms of the gradient diffusion hypothesis given by

$$\overline{\rho u_j'' h''} = -\frac{\bar{\rho} \nu_t}{Pr_t} \frac{\partial \tilde{h}}{\partial x_j} \quad (3.5)$$

$$\overline{t_{ji}u_i''} - \overline{\rho u_j'' \frac{1}{2} u_i'' u_i''} = \left(\mu + \frac{\bar{\rho} \nu_t}{\sigma_k} \right) \frac{\partial k}{\partial x_j} \quad (3.6)$$

where σ_k is a model constant. To obtain ν_t and k to close these models, two different turbulence models were studied. The first is the shear-stress transport (SST) model [78]. With this model, all equations can be integrated to the wall through the viscous sub-layer. The second is the realizable k - ϵ model [79] with the two-layer model of Chen and Patel [80] in the near-wall region. The rotation and curvature correction of Spalart and Shur [81] was applied to both models.

3.3 Numerical Method and Setup

The RANS simulations were performed by using the commercial solver FLUENT version 17.1. A pressure-based segregated solver, SIMPLE, was used to generate solutions. The fluxes for all equations at the cell faces were interpolated by using the second-order upwind scheme. Pressure was computed using second-order accuracy.

In the RANS simulations, a turbulent boundary layer profile with $Re_{\delta_{mom}} = 670$ was directly specified at the inflow boundary along with k and ϵ (or ω) profiles. Because of the symmetry, only half of the hole was simulated with the symmetry boundary condition imposed at the two symmetry planes. At the outflow boundary above the plate, the static pressure was set at 1 atm. At the plenum inlet, a mass-flow rate and temperature yielding the desired blowing ratio and density ratio were specified. The walls had adiabatic and no-slip conditions imposed.

For all computations, iterations were continued until all residuals plateaued to ensure convergence to a steady-state. At convergence, residuals were below 10^{-5} for continuity and 10^{-6} for momentum, energy, and turbulence quantities. An unstructured mesh, consisting of 7.5×10^6 hexahedral cells, was used for the computation. The mesh is shown in Fig. 3.2. For this mesh, y^+ is less than one for the cell next to all walls.

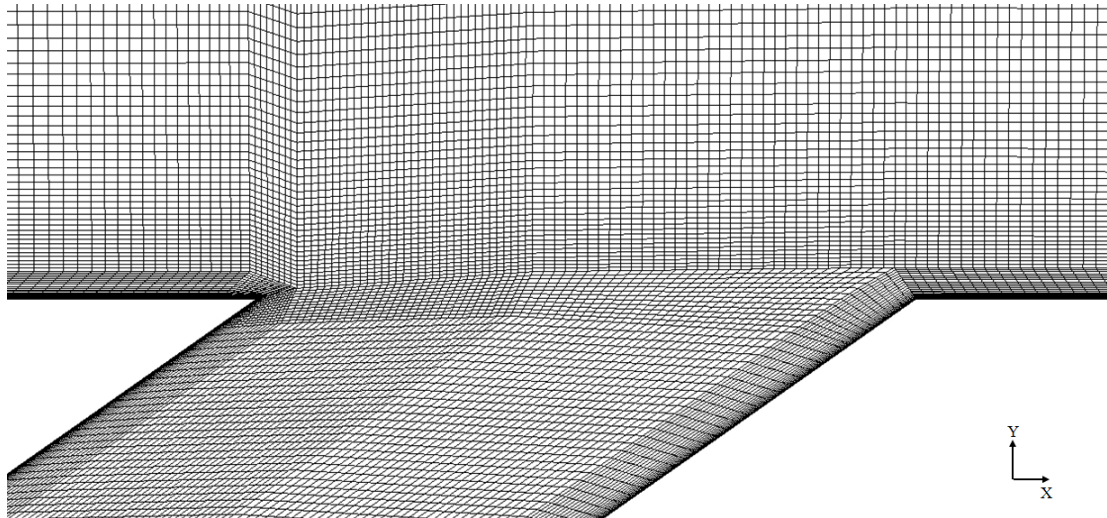


Figure 3.2.: RANS computational mesh.

3.4 Results

The results of this study are organized as follows. First, the meaningfulness of the RANS solutions are examined through grid-sensitivity studies. Afterwards, the adiabatic effectiveness and velocities computed on the optimal grids are compared with experimental measurements. Next, the thermal and turbulent flow field are investigated to understand the differences between LES and RANS. This is followed by analysis of the Boussinesq hypothesis to understand its strengths and weaknesses for film cooling flows. Finally, the gradient-diffusion hypothesis and turbulent Prandtl number are analyzed by using the LES data to understand where in the flow field this model can be applied and where it requires improvement.

3.4.1 Verification and Validation

To ensure the grid is sufficient for the RANS to generate meaningful solutions, the computed centerline and laterally averaged adiabatic effectiveness are compared for grid sizes of 2.5×10^6 , 7.5×10^6 , and 10.5×10^6 . The y^+ for all cells next to the wall is less than one for all grids used. The adiabatic effectiveness obtained by using

the three grid sizes are plotted in Figs. 3.3 and 3.4. Both turbulence models were verified for a high and low BR and DR. Based on the results shown in Figs. 3.3 and 3.4, the grid consisting of 7.5 million grid points was used for the RANS simulations in this study.

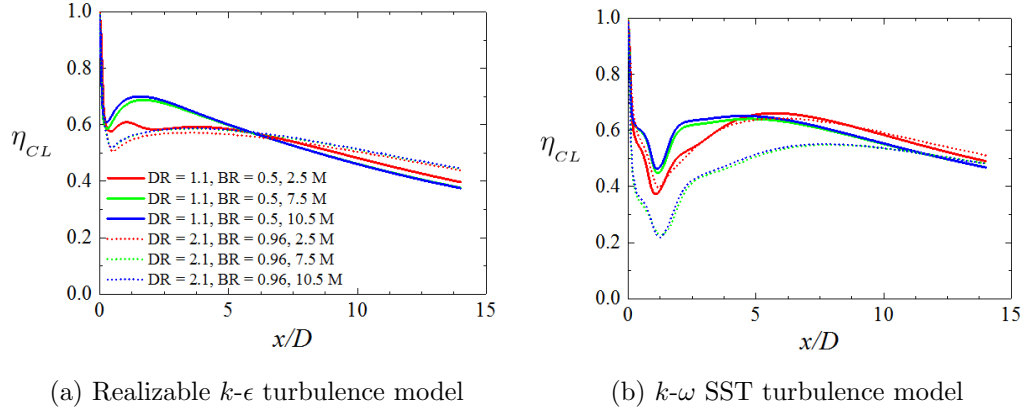


Figure 3.3.: RANS grid independence for centerline adiabatic effectiveness.

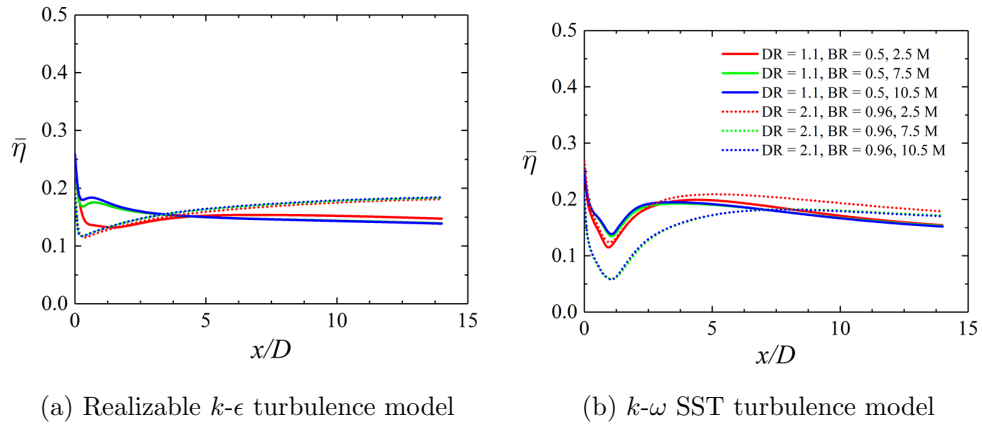


Figure 3.4.: RANS grid independence for laterally averaged adiabatic effectiveness.

The validation with the experiment, by measured adiabatic effectiveness is given in Fig. 3.5. This figure shows the adiabatic effectiveness contours on the wall ($y/D = 0$) along with the hole centerline ($z/D = 0$) and laterally averaged adiabatic effectiveness plots from experiments, LES and RANS. While the LES results match well with the

experimental data, RANS results do not because it is generally unable to capture the correct spreading and dissipation of the jet, especially at low VR. The SST model in particular overestimates the separation of the jet with the flat plate. The centerline plot shows that LES slightly overestimates the adiabatic effectiveness at this location, which may be related to the lower than expected values of non-dimensional temperature ejected from the holes by the experiment, as seen by the darker pink in the experimental contours directly above the hole. This leads to a slight overestimation of the laterally averaged adiabatic effectiveness in some locations, but in general the structure, spreading, and trends are captured correctly. On the other hand, RANS tends to underestimate the laterally averaged adiabatic effectiveness largely due to the lack of lateral spreading and mixing.

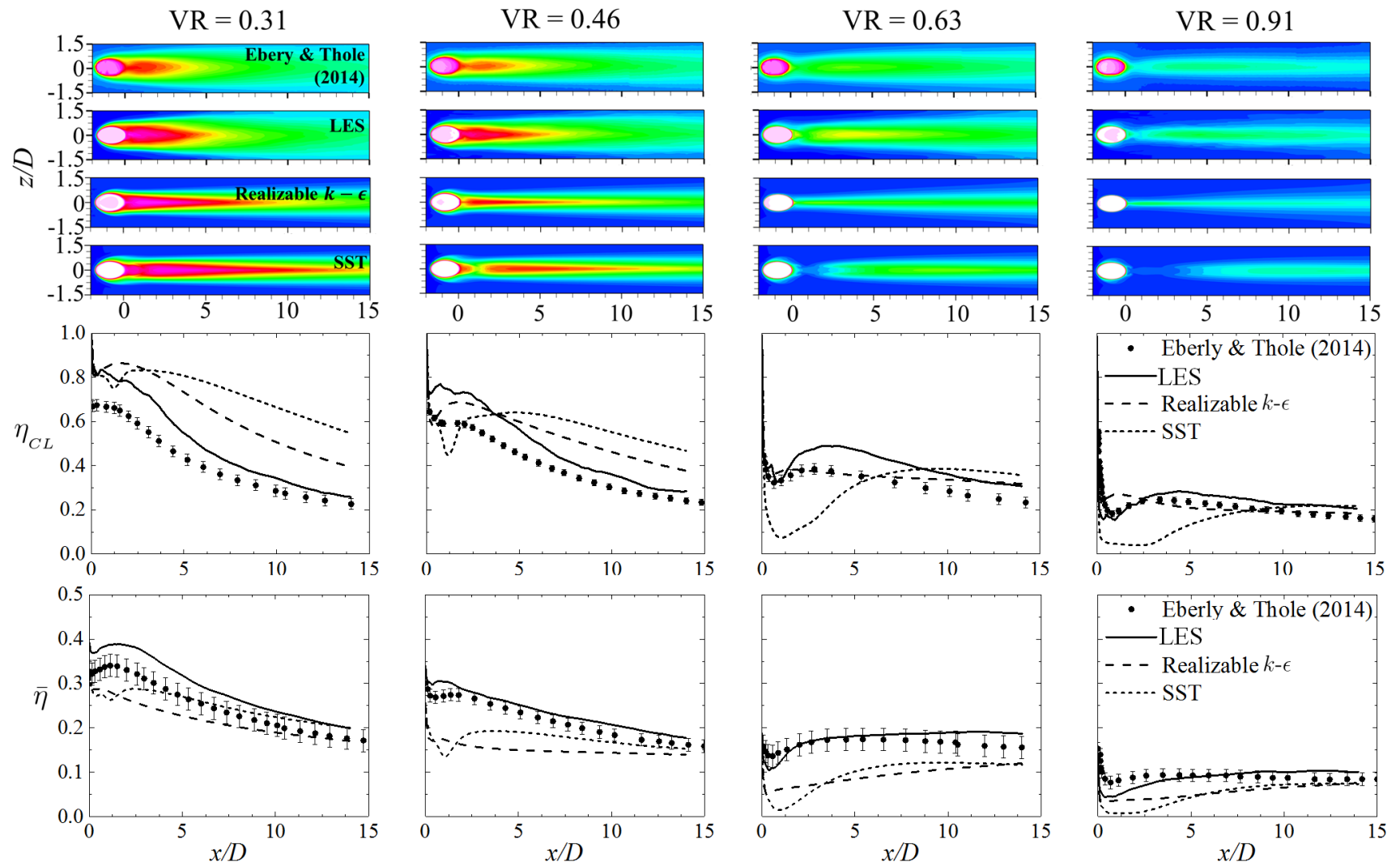


Figure 3.5.: Adiabatic effectiveness measurements experiment, LES, and RANS.

Centerline velocity profiles at $3D$ and $6D$ downstream of the hole are compared in Fig. 3.6. LES can match the experimental data well, whereas $k-\epsilon$ is unable to capture the curvature of the profile and SST tends to underestimate the velocity.

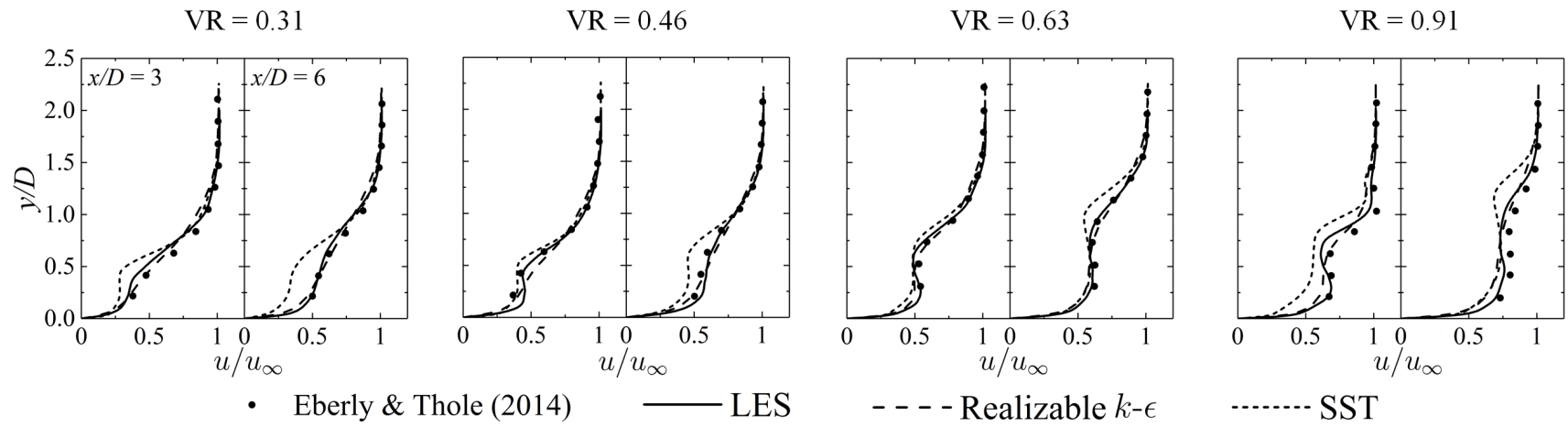


Figure 3.6.: Velocity measurements along $z/D = 0$ at $x/D = 3$ and 6.

3.4.2 Thermal and Turbulent Field

To understand the thermal and turbulent flow field downstream of the cooling jet, three flow variables were analyzed: (1) The non-dimensional temperature to show how the coolant spreads as it mixes with the cross flow; (2) The streamwise vorticity (ω_x) to show the strength and position of the CRVP; (3) The turbulent kinetic energy to give a sense of the turbulent mixing between the jet and oncoming boundary layer. In the following analysis, it is the highly-resolved LES results that were used to provide details of the true nature of the film-cooling flow and highlight regions where the RANS models lack accuracy.

The non-dimensional temperature superimposed with contour lines of ω_x is shown in Fig. 3.7. Additionally, labeled contours of vorticity are included to better visualize the CRVP. In general, neither RANS model can correctly capture the spreading of the jet, especially at $BR = 0.5$ and $DR = 1.6$ ($VR = 0.31$). Realizable $k-\epsilon$ generally captures the temperature gradient at the edge of the jet better than SST. The CRVP is a critical part of the JICF interaction and neither model can capture the strength. SST overestimates the strength, while $k-\epsilon$ tends to underestimate the strength. The $k-\epsilon$ model also shows the point of maximum vorticity to be closer to the wall compared to LES, while SST predicts it to be farther away. The structure of the streamwise vorticity predicted by $k-\epsilon$ more closely matches LES, while SST predicts very concentrated vorticity that dissipates rapidly in space. Interestingly, the lower CRVP strength does not translate to higher spreading of the coolant. RANS does show that the CRVP scales with VR, but the magnitude is incorrect.

The turbulent kinetic energy is plotted in Fig. 3.8. Realizable $k-\epsilon$ can predict the magnitude of k , but cannot capture the curvature induced by the CRVP. SST fails to capture the magnitude, and tends to predict very low k in the middle of the jet near the wall. RANS can capture the scaling of k with VR, but underpredicts k near the wall.

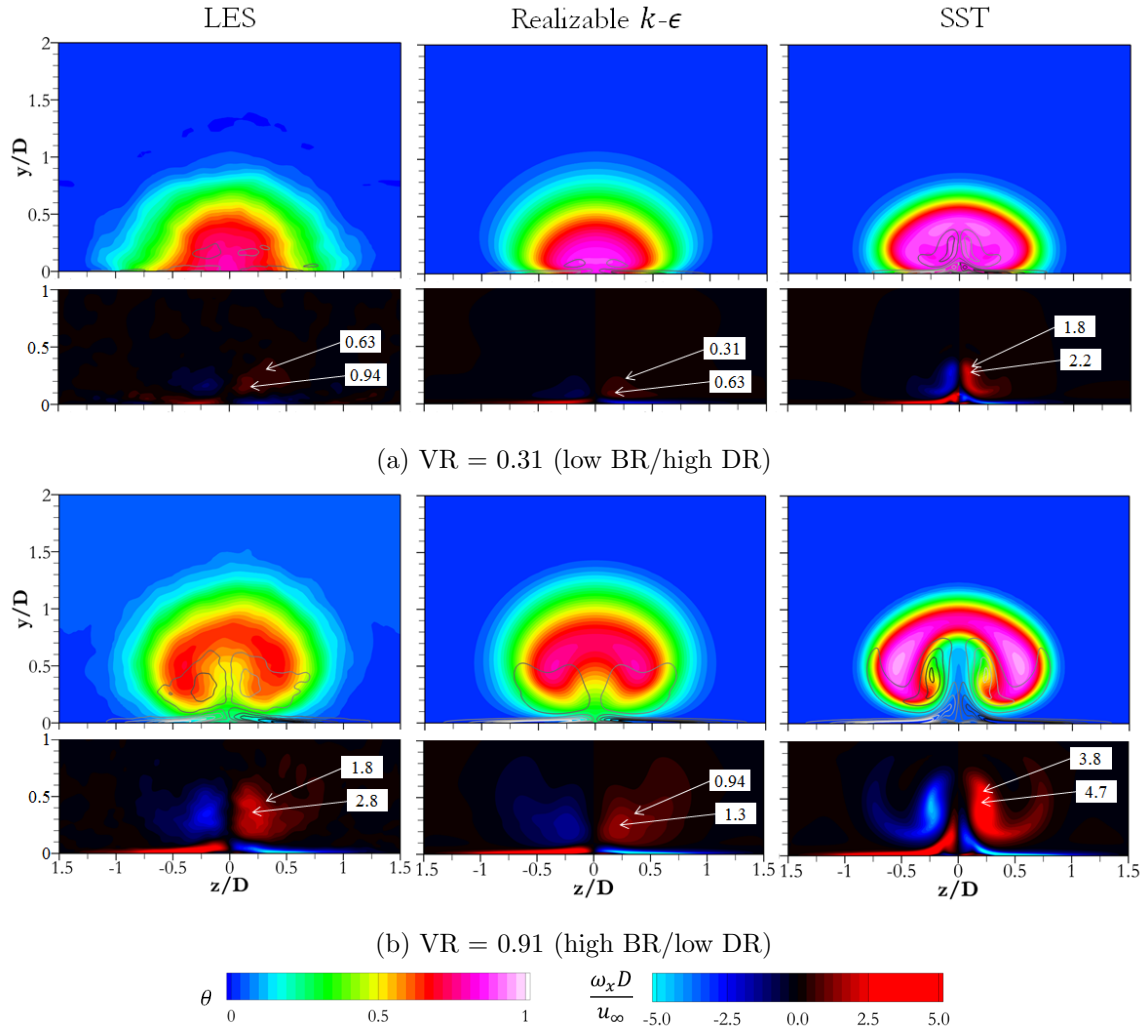


Figure 3.7.: Non-dimensional temperature and ω_x contours at $x/D = 2$.

3.4.3 Boussinesq Hypothesis and Eddy Viscosity

The Boussinesq hypothesis is given by Eq. 3.4. The Boussinesq hypothesis is a linear relationship between the stress and strain and is the main assumption that two-equation turbulence models utilize. Contained within this hypothesis is the eddy viscosity (ν_t), a function of k and ϵ (or ω) that is used to scale the strain rate. The validity of the linear assumption can be evaluated by plotting contours of stress and strain by using the LES data and visually inspecting if a scalar eddy viscosity is

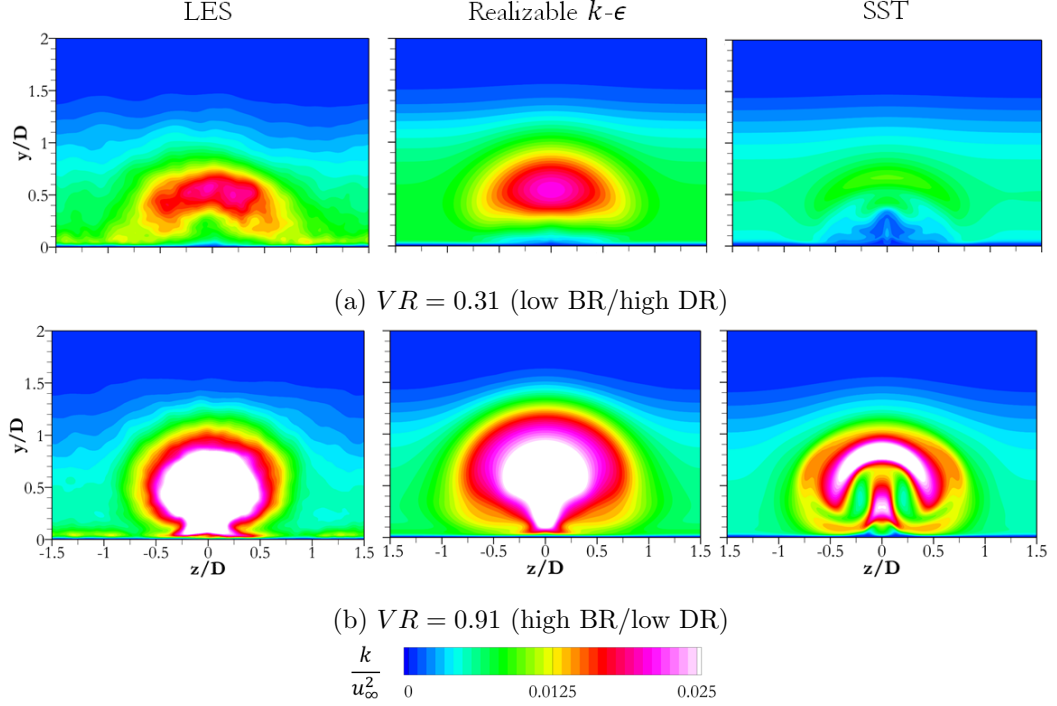


Figure 3.8.: Turbulent kinetic energy (k) at $x/D = 2$.

appropriate. If the linear relationship is appropriate then the stress and strain contour colors and lines should match, though the magnitudes could differ. Figure 3.9 shows the stress and strain contours for the shear-stress components of Eq. 3.4 for $VR = 0.91$ at $x/D = 0$; where blue indicates negative values and red indicates positive values. The location, $x/D = 0$, was chosen because it is just downstream of the film-cooling hole, where the initial mixing with the crossflow takes place, and the mixing here is important as it will influence the behaviour downstream. From Fig. 3.9, it can be seen that all shear-stress components are, in general, aligned with the strain when $y/D > 0.2$. The exception is $\widetilde{v''w''}$ which shows some misalignment and is described below. This suggests that the Boussinesq hypothesis could perform well when $y/D > 0.2$. In the near wall region, the $\widetilde{u''v''}$ and $\widetilde{v''w''}$ stresses are near zero, but the corresponding strain rates are non-zero. However, the $\widetilde{u''w''}$ component is generally aligned with the strain, even at the wall. Coping with this discrepancy is a challenge for models utilizing the Boussinesq hypothesis, which will become more

clear when analyzing the eddy viscosity. To further complicate matters, the counter-rotating vortex pair causes the flow to rotate in the stream-wise direction. Along these rotating streamlines, there is a point of maximum strain, and Eq. 3.4 assumes this is also the point of maximum stress. However, the $\widetilde{v''w''}$ and S_{23} contours make it clear that the point of maximum stress occurs at a further downstream location along the streamline. This lag is not uncommon in turbulent swirling flows, and indicates that curvature-correction should be applied to the RANS equations for this flow. This particular misalignment is most notable at the highest VR, where the CRVP is strongest.

By using the least-squares approach, it is possible to solve for a scalar eddy viscosity based on the Boussinesq hypothesis. This allows for the calculation of eddy viscosity from the LES data as follows:

$$\nu_{t_{LES}} = \frac{-\widetilde{u''_i u''_j} \left(S_{ij} - \frac{1}{3} \frac{\partial \widetilde{u}_k}{\partial x_k} \delta_{ij} \right) + \frac{2}{3} k \delta_{ij} \left(S_{ij} - \frac{1}{3} \frac{\partial \widetilde{u}_k}{\partial x_k} \delta_{ij} \right)}{2 \left(S_{lm} - \frac{1}{3} \frac{\partial \widetilde{u}_k}{\partial x_k} \delta_{lm} \right) \left(S_{lm} - \frac{1}{3} \frac{\partial \widetilde{u}_k}{\partial x_k} \delta_{lm} \right)}. \quad (3.7)$$

This can be used to evaluate the RANS results, as seen in Fig. 3.10. Note that the contours are clipped by $\theta = 0.05$, as Eq. 3.7 is not applicable in the freestream where gradients are very low. From this figure, it can be seen that k - ϵ tends to overpredict ν_t , whereas SST tends to underpredict ν_t . Earlier, it was noted that k - ϵ tends to underpredict the strength of the counter-rotating vortex pair, whereas SST tends to overpredict the strength of the counter-rotating vortex pair. Thus, these parameters are directly correlated.

One particular weakness of the Boussinesq hypothesis is that a single eddy viscosity must apply equally to each Reynolds-stress component. However, in Fig. 3.9, the near-wall region suggests that a single eddy viscosity is incapable of manipulating each strain component to yield the correct Reynolds stress. For instance, the Boussinesq approximation simplifies the $\widetilde{u''w''}$ component to

$$\widetilde{u''w''} = -2\nu_t S_{13}. \quad (3.8)$$

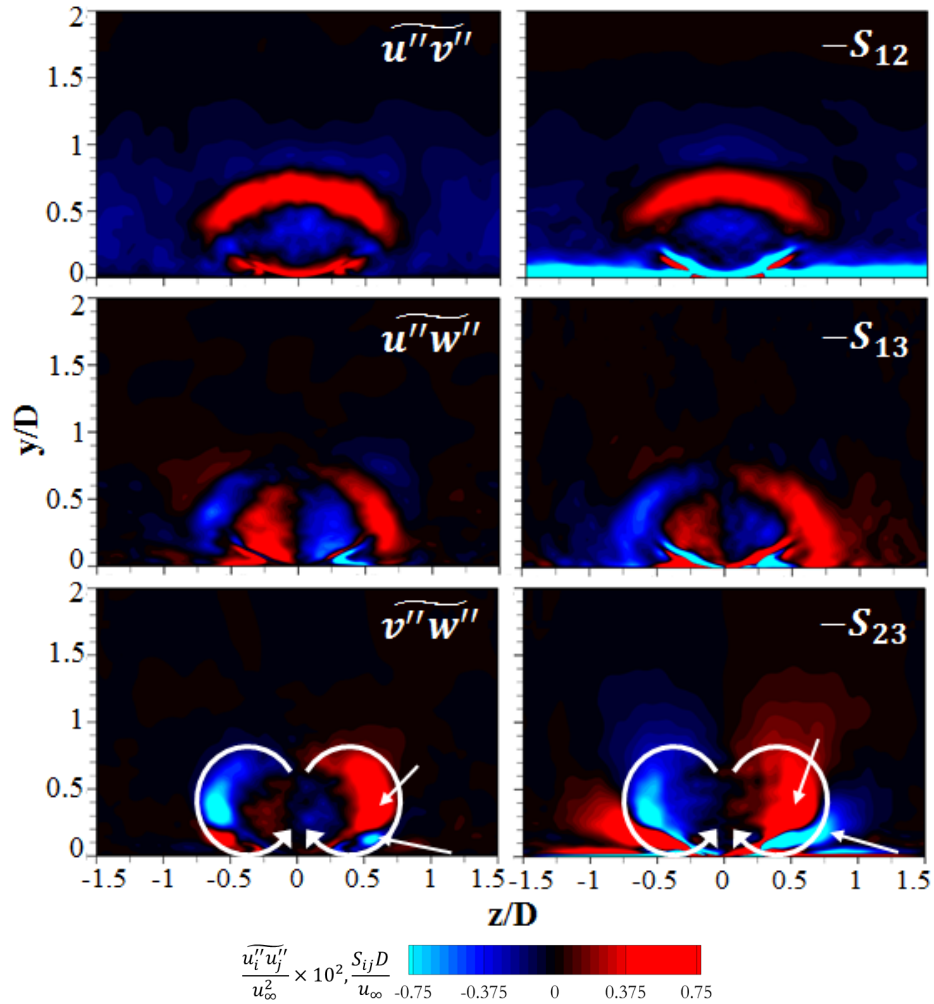


Figure 3.9.: Stress and strain alignment for $VR = 0.91$ (high BR/low DR) at $x/D = 0$ computed with LES data.

The plot of $\widetilde{u''w''}$ is shown in Fig. 3.11. The LES results show that $\widetilde{u''w''}$ acts much closer to the wall than is suggested by the right-hand side of Eq. 3.8. This is due to eddy viscosity approaching zero further away from the wall as seen in Fig. 3.10. So the large S_{12} magnitude near the wall is getting scaled to the near-zero values seen in Fig. 3.9 by the eddy viscosity and, consequently, this scaling degrades the prediction of $\widetilde{u''w''}$ and $\widetilde{v''w''}$. Thus, solving RANS equations with an “optimal” scalar eddy viscosity as suggested by LES, would still yield unsatisfactory results

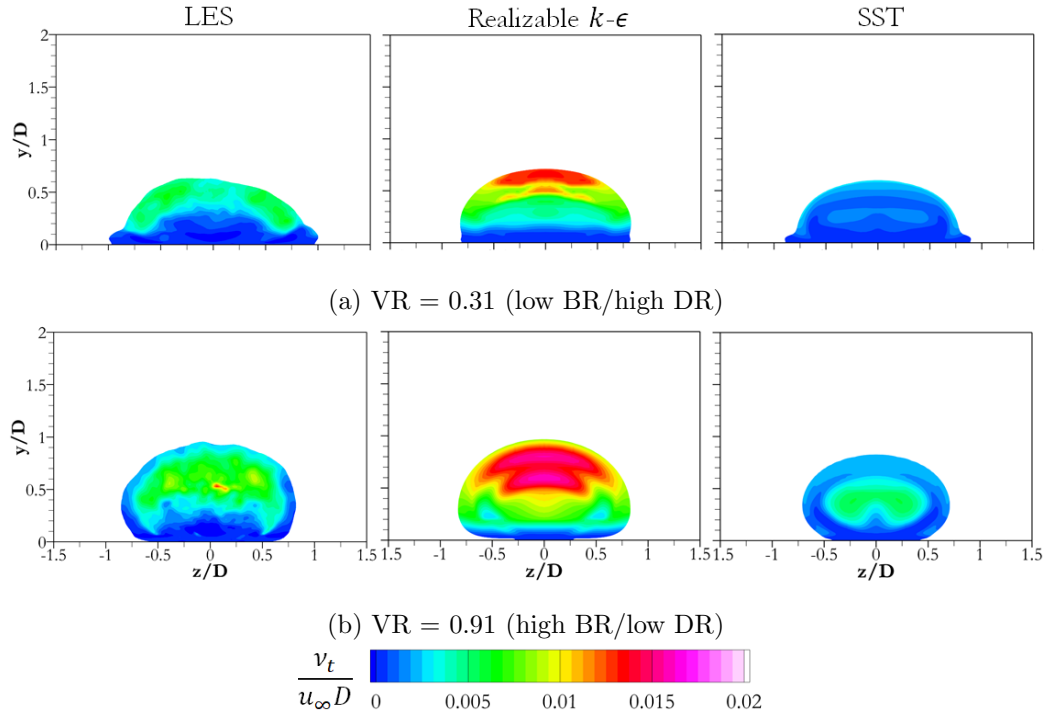


Figure 3.10.: LES and RANS contours of eddy viscosity at $x/D = 0$.

in terms of modeling the Reynolds stresses. However, matching the magnitude of the eddy viscosity predicted by LES could yield more accurate predictions of the CRVP strength. Above the wall ($y/D \gtrsim 0.2$), the scalar eddy-viscosity assumption is generally applicable as discussed earlier. This means that a two-layer model that can accurately capture the near-wall anisotropy could yield much improved results (such as by using a tensor eddy viscosity), and is the reason why the model developed by Lakehal [45] showed much improved results over standard models.

3.4.4 Gradient-Diffusion Hypothesis and Turbulent Prandtl Number

Two-equation RANS models use the gradient-diffusion hypothesis (GDH) to model the turbulent heat flux, and it is given by

$$\widetilde{u_i''\theta''} = -\frac{\nu_t}{Pr_t} \frac{\partial \widetilde{\theta}}{\partial x_i}, \quad (3.9)$$

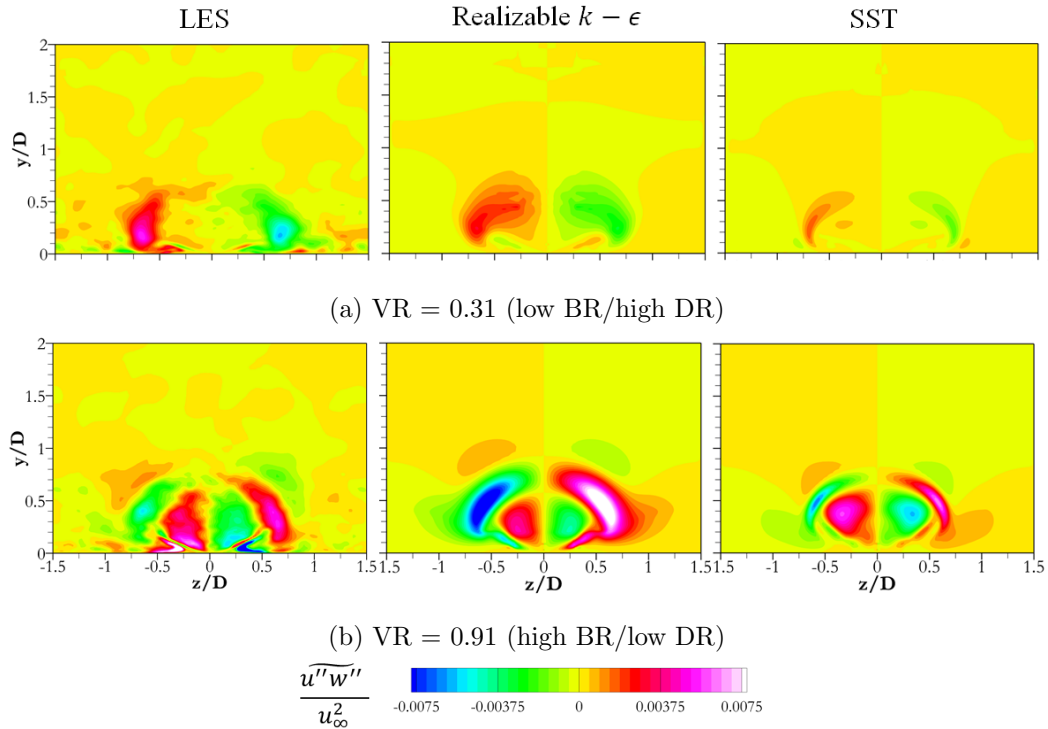


Figure 3.11.: LES and RANS contours of $\widetilde{u''w''}$ at $x/D = 0$.

which is the same model as the one given in Eq. 3.5. The eddy diffusivity (α_t) is ν_t/Pr_t . Like the Boussinesq hypothesis, both sides of the equation can be plotted using LES and inspected visually to evaluate the appropriateness of the linear assumption. According to Eq. 3.9, the turbulence is assumed to transport heat in the direction of the temperature gradient. The turbulent heat flux and temperature gradient are plotted in Fig. 3.12. From this figure, it can be seen that the turbulent heat flux and temperature gradient are generally aligned at all but the highest VR. Thus, like the Boussinesq hypothesis, the gradient diffusion hypothesis is generally reasonable. However, the near-wall region puts the hypothesis in a precarious position. As shown in Fig. 3.12 (particularly the zoomed regions), there are regions of the flow where the heat fluxes and temperature gradients are not the same color, primarily near the wall. This phenomenon is termed counter-gradient diffusion, and it contradicts the basic assumption of this model. This phenomenon generally appears in the

presence of large-scale mixing. In this case, it is between the shear-layer vortices and counter-rotating vortex pair. This is especially evident at the highest VR, where the counter-gradient diffusion even occurs in the shear layer near the top of the jet.

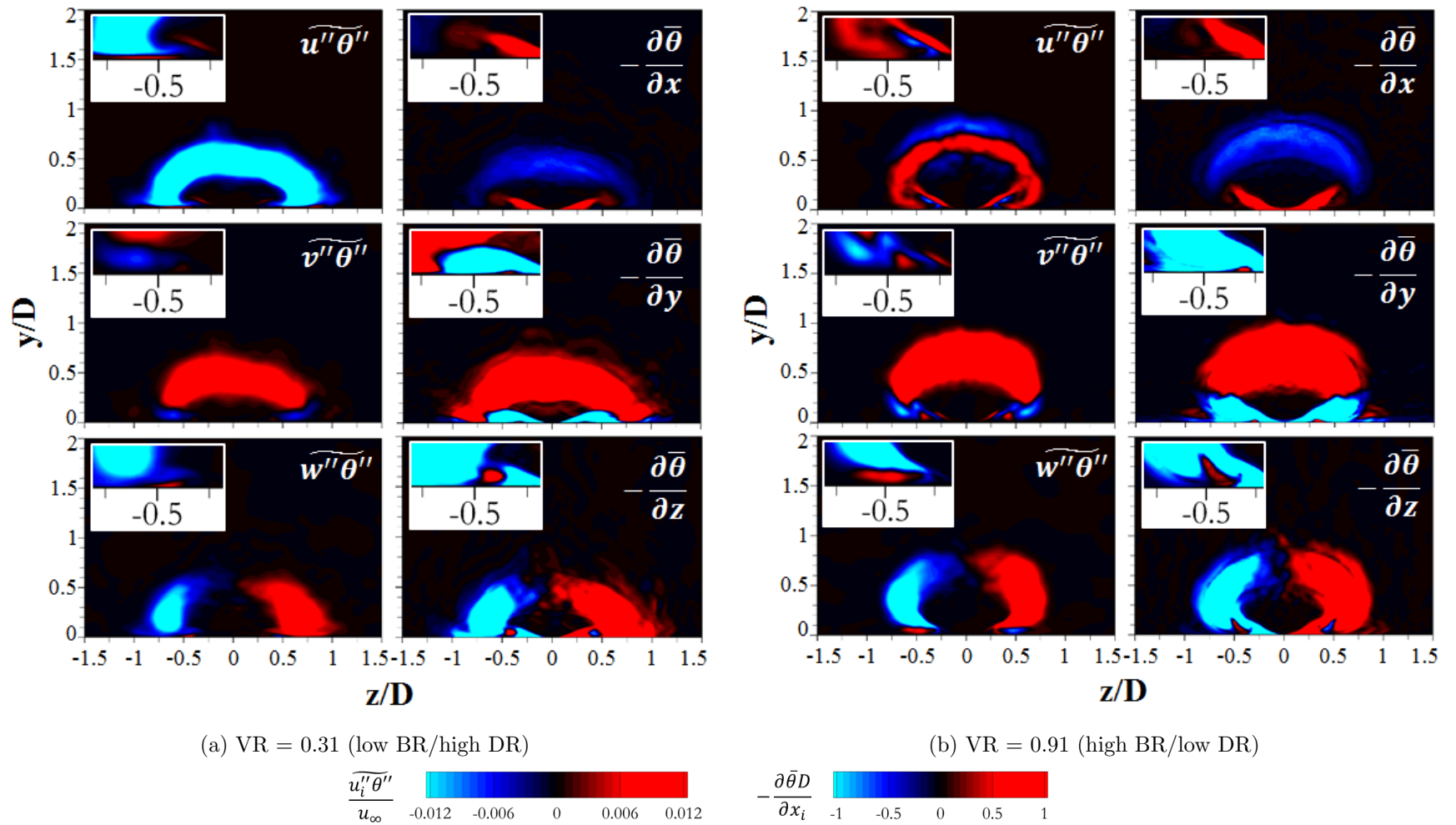


Figure 3.12.: Turbulent heat flux and non-dimensional temperature gradient at $x/D = 0$ computed with LES data.

To scale the temperature gradient to the appropriate turbulent heat flux, the GDH utilizes the eddy diffusivity, which is just the eddy viscosity scaled by a turbulent Prandtl number. RANS simulations typically assume Pr_t to be a constant with a value around 0.85. The LES data can be used to approximate the Prandtl number by first using a least-squares method to solve for the eddy diffusivity as follows:

$$\alpha_{t_{LES}} = \frac{-\widetilde{u_i''\theta''} \frac{\partial \widetilde{\theta}}{\partial x_i}}{\frac{\partial \widetilde{\theta}}{\partial x_j} \frac{\partial \widetilde{\theta}}{\partial x_j}} \quad (3.10)$$

Then the turbulent Prandtl number is

$$Pr_{t_{LES}} = \frac{\nu_{t_{LES}}}{\alpha_{t_{LES}}}. \quad (3.11)$$

Contours of $Pr_{t_{LES}}$ in the jet region are plotted in Fig. 3.13 along with the contours of $\alpha_{t_{LES}}$. Like ν_t , $Pr_{t_{LES}}$ is not well defined where the gradients are near zero. Here it can be seen that Pr_t approaches ~ 0.1 near the wall at the edge of the jet. Also, there are small regions of negative Pr_t . This is indeed possible as it can help account for the counter-gradient diffusion. In the body of the jet, Pr_t increases to ~ 0.5 , but remains well below the value of 0.85 imposed by RANS. The corresponding contours of α_t show the result of scaling ν_t by the calculated Pr_t . In the center of the jet near the wall, α_t is near zero to ensure the turbulent heat flux is low there, as it should be. At the outer edge of the jet near the wall, α_t increases slightly to account for turbulent heat flux. Note, that this behavior is due to the spatially varying Pr_t . If a constant Pr_t were imposed, then the near wall α_t would be near zero throughout as indicated by the earlier ν_t contours, which would eliminate the turbulent heat flux all together.

Interestingly, the behavior of α_t remains similar over the range of VRs, despite a clear evolution of the turbulent heat flux. This weakness is rooted in the simplicity of the GDH model. Despite the improvement of utilizing low values of Pr_t near the wall, the scalar eddy diffusivity cannot capture the subtle differences in the turbulent heat-flux components over a range of VRs. The misalignment between the turbulent

heat flux and the temperature gradient could be further improved by accounting for the anisotropy of the eddy diffusivity.

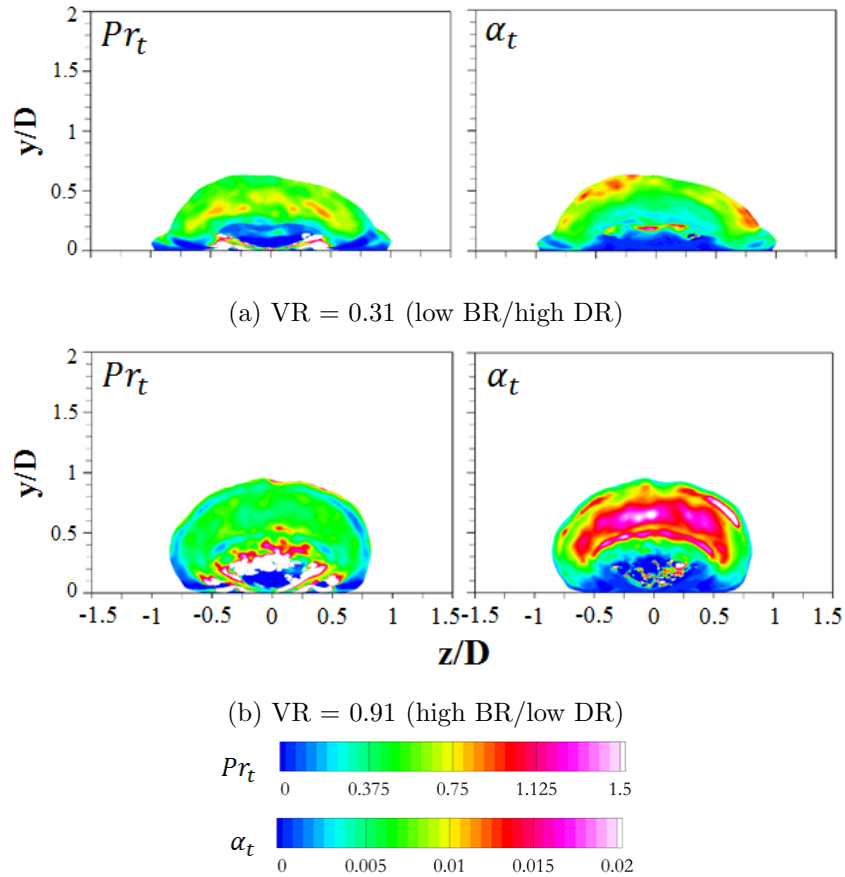


Figure 3.13.: Turbulent Prandtl number and eddy diffusivity at $x/D = 0$ computed with LES data.

3.5 Summary

A computational study based on LES and RANS was performed to examine the limitations of two RANS turbulence models, realizable $k-\epsilon$ and SST, in predicting film-cooling flows through round holes. In general, RANS can predict the scaling of turbulent kinetic energy and CRVP strength with VR. However, $k-\epsilon$ tends to underpredict the CRVP strength, whereas SST tends to overpredict the CRVP strength.

Matching the eddy viscosity predicted by LES could yield more accurate predictions of the CRVP strength in RANS simulations. RANS also underpredicts the near wall temperature gradient, this leads to the noticeable lack of lateral spreading of the coolant.

The LES data was used to examine the Boussinesq hypothesis. In general, the assumed linear relationship between stress and strain fields is reasonable for $y/D \gtrsim 0.2$, especially for lower VRs. There is some evidence of misalignment of the stress and strain at higher VRs due to the curvature in the streamline induced by the strong CRVP, suggesting that a curvature correction should be utilized. However, in the near wall region ($y/D \lesssim 0.2$), there are non-zero strain rates that are difficult to scale to near-zero stresses, notably S_{12} and S_{23} . Using the method of least-squares an “ideal” scalar eddy viscosity was solved for by using the LES data. This eddy viscosity showed that realizable $k-\epsilon$ overpredicted the eddy viscosity while SST underpredicted it. This result correlates with the relative strengths of the CRVP predicted by each model. However, the eddy viscosity from LES approaches zero too far from the wall. Further analysis reveals that this leads to incorrect predictions of Reynolds stresses near the wall, notably $\widetilde{u''w''}$, which influences spreading of the flow laterally over the wall. Thus, anisotropy must be accounted for in the near-wall region, since a scalar eddy viscosity cannot account for the behavior of $\widetilde{u''w''}$ and $\widetilde{u''v''}$ simultaneously.

The gradient-diffusion hypothesis was evaluated with LES data, showing that film-cooling flow exhibits counter-gradient diffusion near the wall at all VRs as well as in the shear layer at the top of the jet at the highest VR. This directly violates the assumption of the gradient-diffusion hypothesis. However, manipulating the eddy diffusivity or Pr_t could offer possible work-arounds. The Pr_t was estimated with LES data using the method of least-squares, and it was found to decrease to values near 0.1 near the wall, much less than the constant 0.85 that RANS assumes. These results suggest Pr_t should vary spatially, or a non-scalar eddy diffusivity should be utilized near the wall in order to apply the gradient-diffusion hypothesis to film-cooling flow.

4. EFFECTS OF VELOCITY RATIO ON TRENDS IN FILM-COOLING ADIABATIC EFFECTIVENESS AND TURBULENCE

The previous two chapters showed that the turbulence tends to scale with VR and several effects of VR on turbulence modeling were addressed. However, by fixing the VR, the effects of BR, DR, and MR on adiabatic effectiveness and turbulence trends can be examined. Additionally, the previous two chapters described the LES and RANS governing equations, numerical method and setup, and verification, thus, the details are omitted in this chapter.

In this chapter, the LES and RANS results are presented that address the fourth objective. First, the film-cooling problem is described. Next, the simulation results including adiabatic effectiveness trends, turbulent kinetic energy, Reynolds stresses, and turbulent heat flux are analyzed. Parts of this chapter are adapted from an upcoming conference presentation by Stratton and Shih [82].

4.1 Problem Description

The problem studied is identical to that studied in Chapter 3, it is shown in Fig. 4.1, for reference. It consists of a flat plate film cooled by jets issuing from a plenum through one row of circular holes. Each hole has diameter, $D = 2.6$ mm, and length, $L = 4.7D$, and is inclined at 35° with respect to the plate. The holes along the row are spaced $3D$ apart.

The turbulent boundary layer, measured $5D$ upstream of the hole, has a boundary layer thickness of $\delta = 1.2D$ and momentum thickness of $\delta_{mom} = 0.13D$, which corresponds to a $Re_{\delta_{mom}} = 670$. The LES results used in this chapter correspond

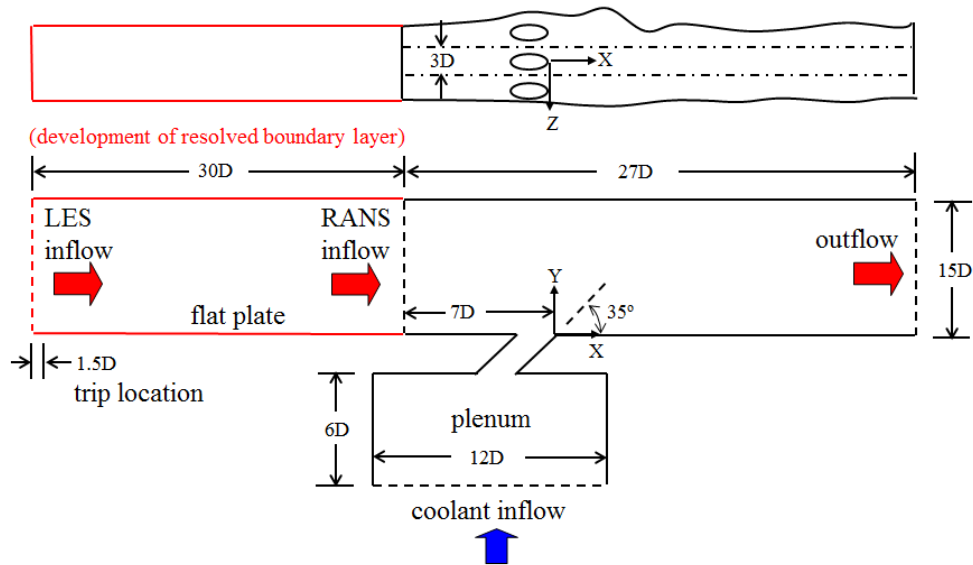


Figure 4.1.: Computational Model.

to those with a resolved turbulent boundary layer. The RANS cases use either the realizable $k-\epsilon$ or $k-\omega$ SST turbulence models. Two different VRs are studied, 0.46 and 0.63. For each VR, three different DRs, BRs, and MRs are studied; this gives a total of six unique cases. Two of these six cases were studied in Chapters 2 and 3. The additional cases introduce three new BRs (0.68, 0.73, 1.3) and one new DR (2.1). The Reynolds numbers for DR = 1.1, 1.6, and 2.1, based on hole diameter and freestream velocity and viscosity, are $Re = 6160$, $Re = 5135$, and $Re = 4112$, respectively. A summary of cases studied is given in Table 4.1.

4.2 Results

The results of this study are organized as follows. First, the adiabatic effectiveness trends are evaluated for the LES and compared to the RANS and available experimental data. Next, the turbulent kinetic energy is analyzed for a fixed VR. Finally, the Reynolds stresses and turbulent heat flux predicted by RANS are evaluated with

Table 4.1.: Summary of cases.

Turbulence Method	DR	BR	VR	MR	$T_c(K)$	$T_\infty(K)$
LES	1.1	0.5	0.46	0.23	269	296
LES	1.6	0.73	0.46	0.33	203	329
LES	2.1	0.96	0.46	0.43	175	375
LES	1.1	0.68	0.63	0.42	269	296
LES	1.6	1.0	0.63	0.63	203	329
LES	2.1	1.3	0.63	0.80	175	375
Realizable $k-\epsilon$	1.1	0.5	0.46	0.23	269	296
Realizable $k-\epsilon$	1.6	0.73	0.46	0.33	203	329
Realizable $k-\epsilon$	2.1	0.96	0.46	0.43	175	375
Realizable $k-\epsilon$	1.1	0.68	0.63	0.42	269	296
Realizable $k-\epsilon$	1.6	1.0	0.63	0.63	203	329
Realizable $k-\epsilon$	2.1	1.3	0.63	0.80	175	375
$k-\omega$ SST	1.1	0.5	0.46	0.23	269	296
$k-\omega$ SST	1.6	0.73	0.46	0.33	203	329
$k-\omega$ SST	2.1	0.96	0.46	0.43	175	375
$k-\omega$ SST	1.1	0.68	0.63	0.42	269	296
$k-\omega$ SST	1.6	1.0	0.63	0.63	203	329
$k-\omega$ SST	2.1	1.3	0.63	0.80	175	375

respect to the LES data to determine how well the models capture trends when VR is fixed.

4.2.1 Adiabatic Effectiveness Trends

The CFD results have been validated by comparing with infrared camera data of Eberly and Thole [38]. The experimental and CFD data for the laterally-averaged

adiabatic effectiveness is shown in Figs. 4.2 and 4.3. To study the effect of a fixed VR, additional cases were included in which corresponding experimental data was unavailable. Therefore, only one experimental data set is included for each VR.

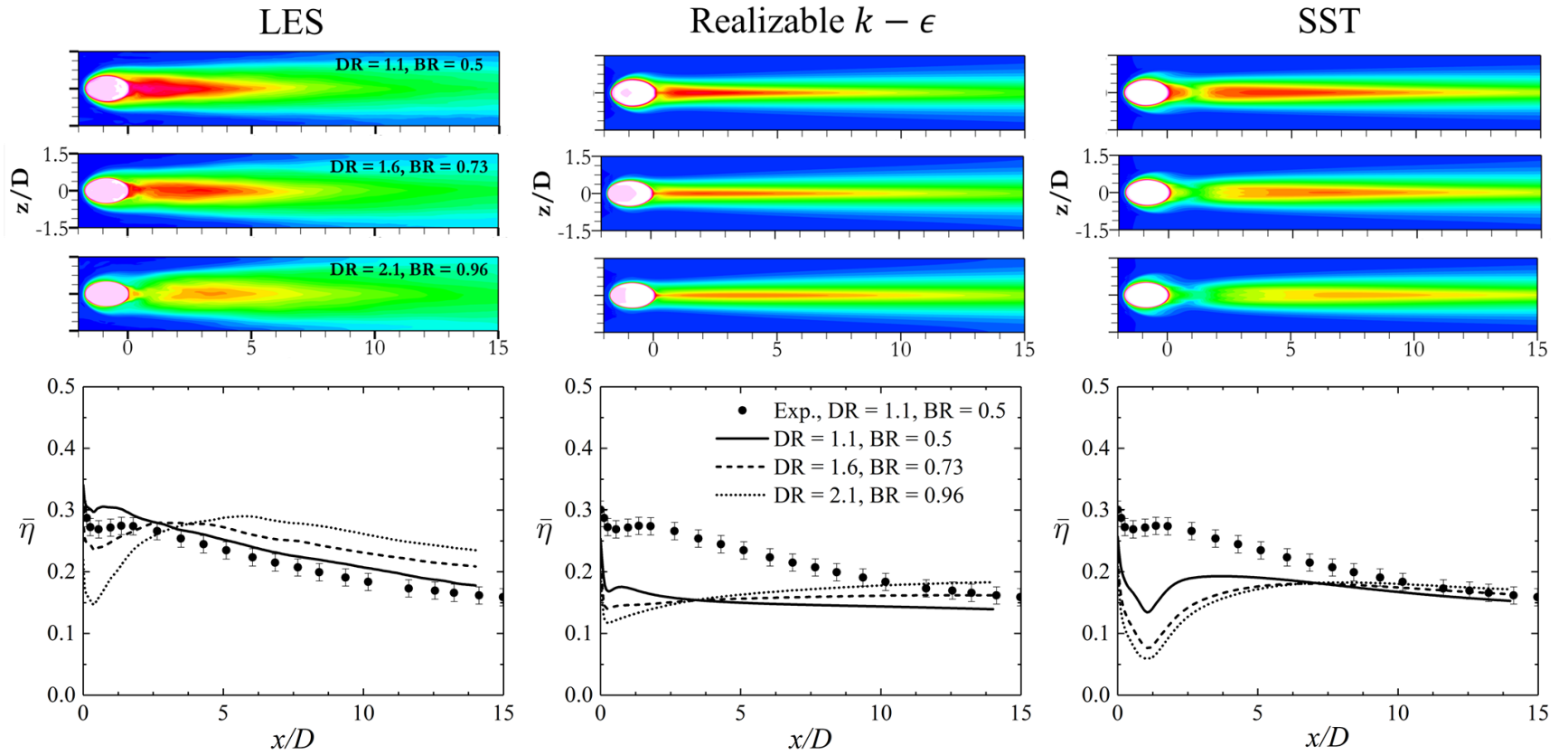


Figure 4.2.: Adiabatic effectiveness measurements for $VR = 0.46$

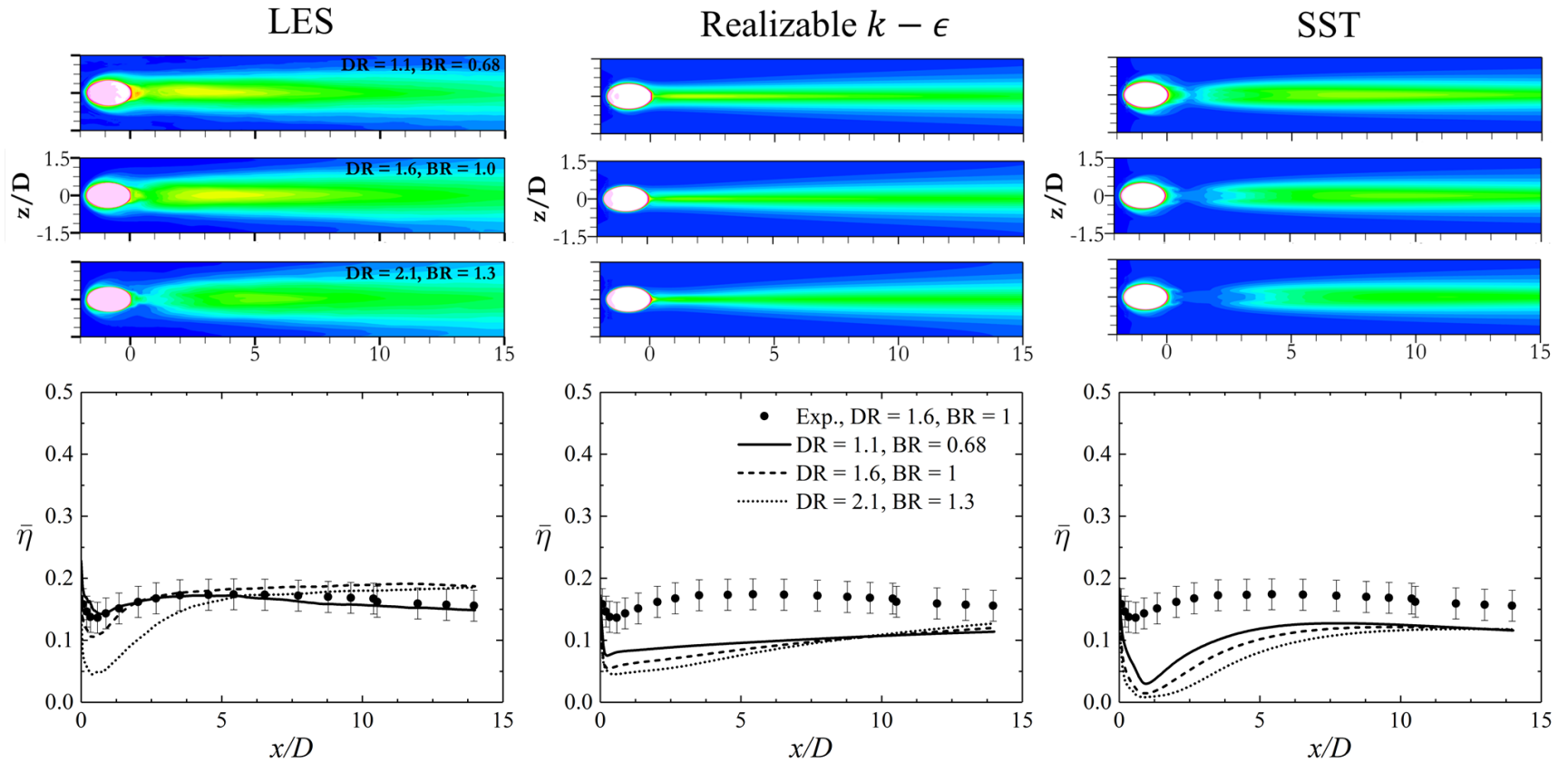


Figure 4.3.: Adiabatic effectiveness measurements for $VR = 0.63$

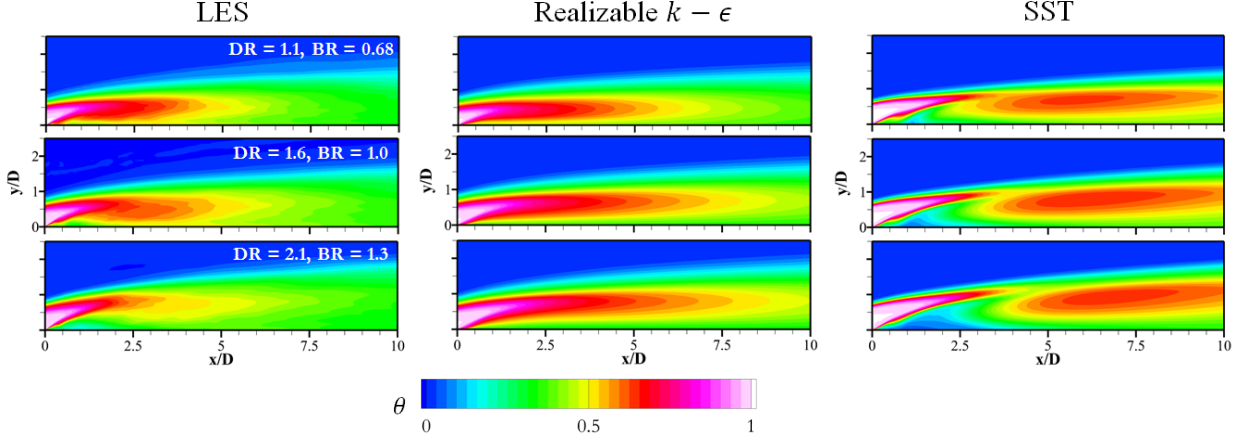


Figure 4.4.: Non-dimensional temperature at $z/D = 0$ for $VR = 0.63$

Figures 4.2 and 4.3 show that RANS underestimates the adiabatic effectiveness in all cases, with the separation and spreading being predicted incorrectly. This is an expected result that highlights the difficulty in predicting adiabatic effectiveness with RANS models. However, since the LES results in this study provide a detailed turbulence benchmark that most experiments cannot provide we can gain greater insight into how different turbulence quantities are related to the trends in the adiabatic effectiveness.

The LES results in Figs. 4.2 and 4.3 show how adiabatic effectiveness changes when BR, DR, and MR increase for a fixed VR. Notably, the jet separation from the flat plate increases as MR increases which can be seen as a reduction in η downstream of the hole. For $VR = 0.46$ this results in a 50% drop of $\bar{\eta}$ from 0.3 to 0.15, and for $VR = 0.63$, a 66% drop from 0.15 to 0.05. While MR increases, the DR and BR are also increasing, resulting in more spreading on the flat plate. So, for $VR = 0.46$, while the separation reduces cooling near the hole, it recovers such that by $x/D = 5$, the high DR/BR case provides the most cooling, in a laterally-averaged sense. At the higher VR, again the high DR/BR case recovers significantly downstream, but tends to match the performance of the DR = 1.6 and BR = 1.0 case. This suggests that spreading increases with DR, but as BR and MR continue to increase there is

a point where excessive separation hurts the downstream recovery. Additionally, at the higher VR, the η decreases in all cases.

The separation between the cooling jet and flat plate can be seen clearly on the $z/D = 0$ plane which is shown in Fig. 4.4 for VR = 0.63. When DR/BR increases the coolant penetrates further into the freestream resulting in less cooling just downstream of the jet. The recovery occurs when the coolant spreads after mixing with the crossflow which results in a rise in cooling downstream. For example, in LES for DR = 1.6 the coolant reattaches at $x/D = 1.5$.

While Figs. 4.2 and 4.3 show RANS to significantly underestimate adiabatic effectiveness and the effect of MR, there are several positive notes. The trends that we want to capture with RANS include the separation, spreading, recovery, and overall adiabatic effectiveness scaling with VR. First, realizable $k-\epsilon$ and SST are both predicting increased separation as MR increases, however the drop in η downstream of the hole is much smaller between different MRs. In terms of the spreading of η , both turbulence models show little evidence that increasing BR and DR is increasing the spreading. The combined effect of the separation and spreading inaccuracies leads to cooling predictions that are very similar. For instance, SST at VR = 0.46 shows that $\bar{\eta}$ changes minimally between DR = 1.6 and 2.1; likewise, at VR = 0.63 both realizable $k-\epsilon$ and SST predict very small changes in $\bar{\eta}$. This makes it challenging for designers to find optimal cooling configurations. In general, the turbulence models both capture the recovery of the cooling downstream to be greatest for the case of DR = 2.1. However, LES shows an absolute difference in $\bar{\eta}$ between the low and high points for DR = 2.1 to be ~ 0.15 for both VRs; $k-\epsilon$ predicts ~ 0.07 , while SST predicts ~ 0.1 . Conversely, at DR = 1.1 there should be little separation, but SST tends to overpredict this separation, resulting in unnecessarily large recoveries downstream at both VRs. Finally, while $\bar{\eta}$ is underpredicted by RANS, the scaling of the cooling with VR is captured by both turbulence models, with η decreasing for all cases as VR increases.

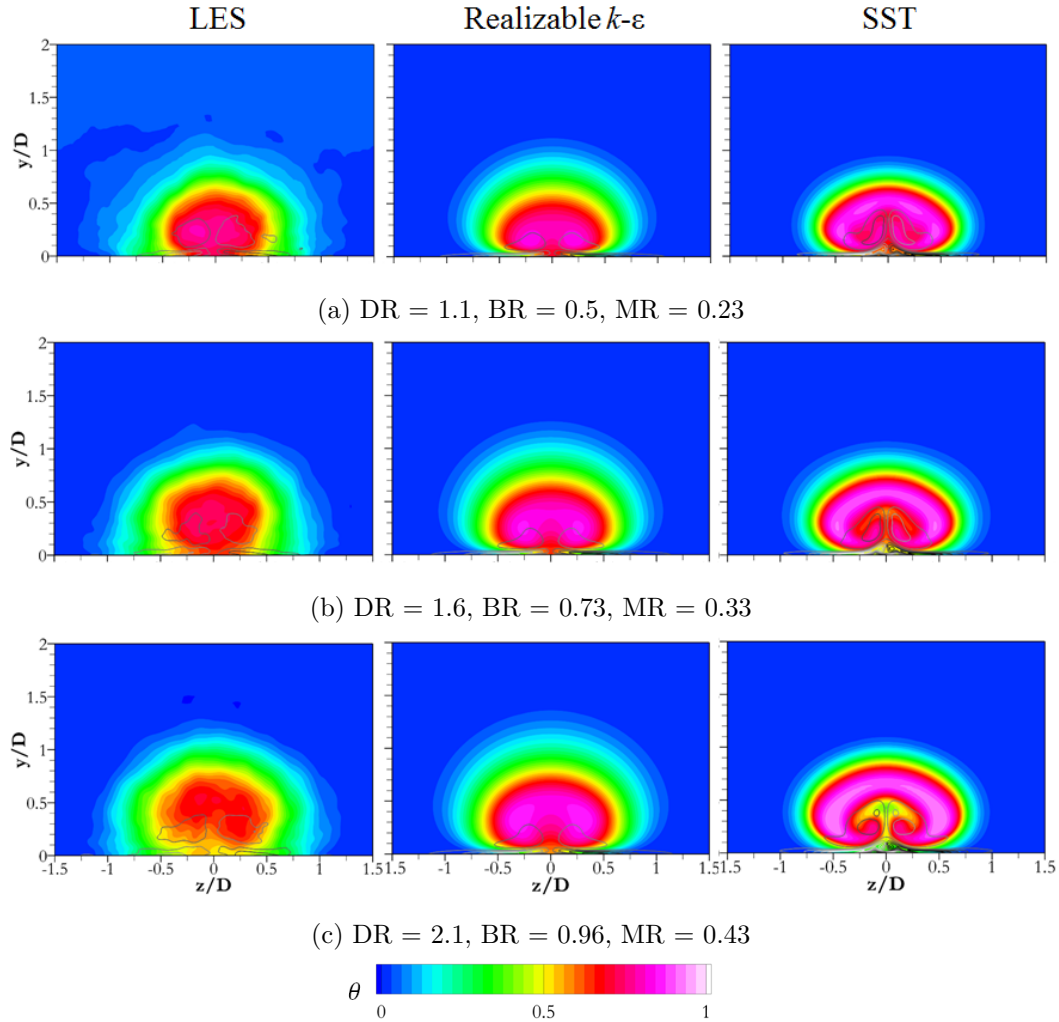


Figure 4.5.: Non-dimensional temperature with ω_x contour lines at $x/D = 2$ for $VR = 0.46$

To better understand how the coolant spreads three-dimensionally, Figs. 4.5 and 4.6 show contours of non-dimensional temperature at $x/D = 2$ superimposed with contour lines of the x -vorticity. The most notable difference is RANS's inability to capture the near-wall diffusion, both in the shear layer as well as the core region. However, $k-\epsilon$ model captures diffusion better than SST above the wall. For a given VR , the strength of the CRVP is relatively constant, with minimal scaling with MR . The CRVP is responsible for deforming the coolant profile into a kidney-shape. Again,

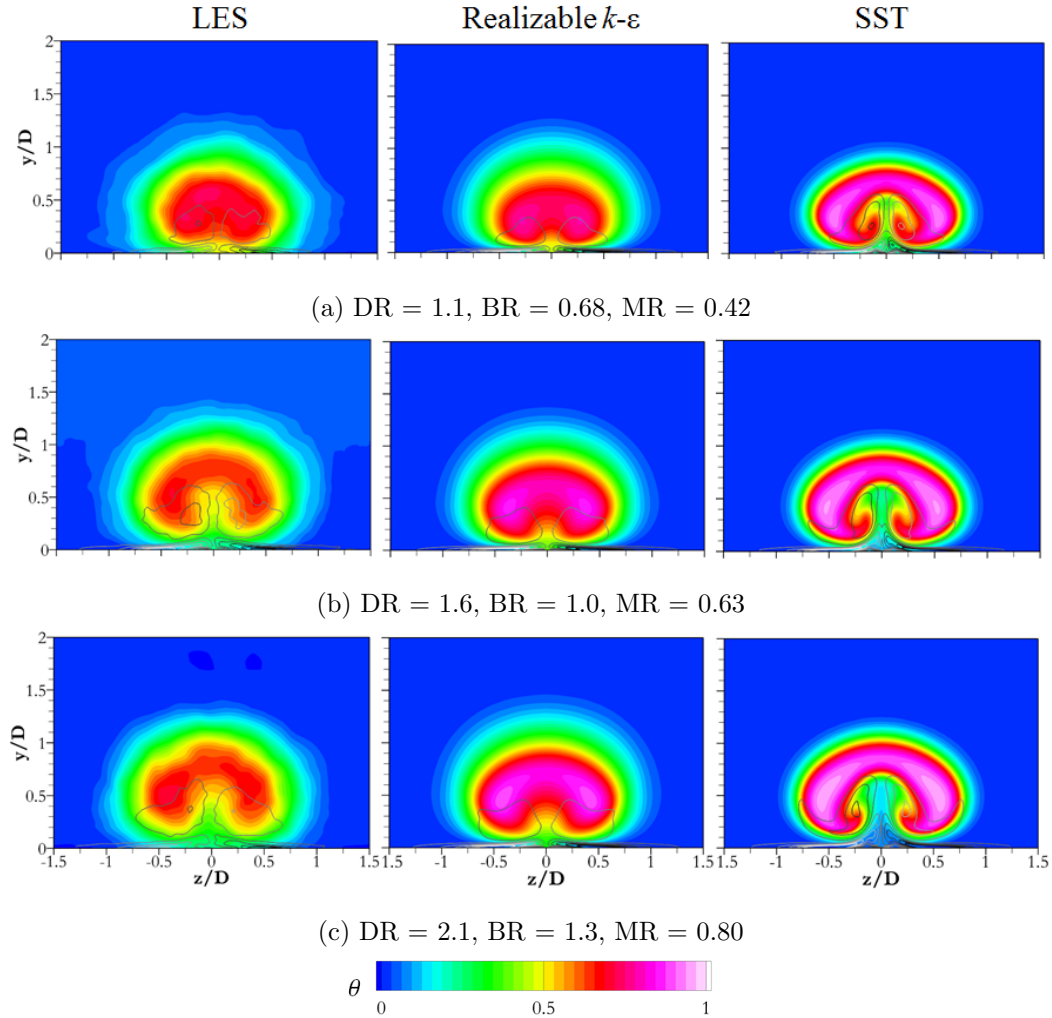


Figure 4.6.: Non-dimensional temperature with ω_x contour lines at $x/D = 2$ for $VR = 0.63$

$k-\epsilon$ captures this better than SST, which significantly overestimates the change in CRVP strength with MR. Also, note that MR increases from 0.23 to 0.43 for $VR = 0.46$, but from 0.42 to 0.80 for $VR = 63$. This larger absolute difference explains the relatively larger change in θ for $VR = 0.63$.

4.2.2 Turbulent Kinetic Energy

The turbulent kinetic energy can show regions of enhanced turbulent mixing as well as the intensity of the mixing. In two-equation RANS models, a transport equation is solved to directly find k and this is the value that is analyzed here. However, k can also be defined in terms of Reynolds stresses as $\frac{1}{2}(\overline{u''u''} + \overline{v''v''} + \overline{w''w''})$, which is how the LES value is calculated. Figures 4.7 and 4.8 show k at $x/D = 0$ for LES and RANS. This position was chosen to examine the mixing as soon as the jet exits the hole, as this will influence the downstream behaviour of the cooling jet. Interestingly, the LES shows that the magnitude of k tends to scale with MR at a fixed VR, while the VR tends to influence the structure of the mixing. At VR = 0.46, the k is highest at the sides of the jet near the wall. This location corresponds to the mixing by means of the shear layer between the crossflow and the jet, as well as the mixing by means of the CRVP, these are two large scale interactions that result in high turbulent energy. This behaviour would certainly enhance the mixing and help spread the coolant near the wall as was seen in Figs. 4.5 and 4.6. At VR = 0.63, there is still higher k at the sides of the jet near the wall, but additionally there is higher k near the center of the jet as well.

Interestingly, the structure of k cannot be replicated by either turbulence model. Realizable k - ϵ can capture the increasing magnitude of k with MR and it also captures the general structural change when VR = 0.63. However, it predicts very low levels of k at the sides of the jet, near the wall, and instead concentrates most of the turbulent mixing in the shear layer on the top of the jet. The predictions by SST are slightly worse, since it shows k is opposite of what LES predicts, with exceptionally low values where it should be highest. Additionally, the magnitude of k is not changing with MR. The only trend that SST captures is the structural change when going from VR = 0.46 to 0.63. Overall, LES shows that k should be concentrated near the sides of the jet and the magnitude should change with MR; capturing this effect could help RANS models better predict differences in η when VR is fixed.

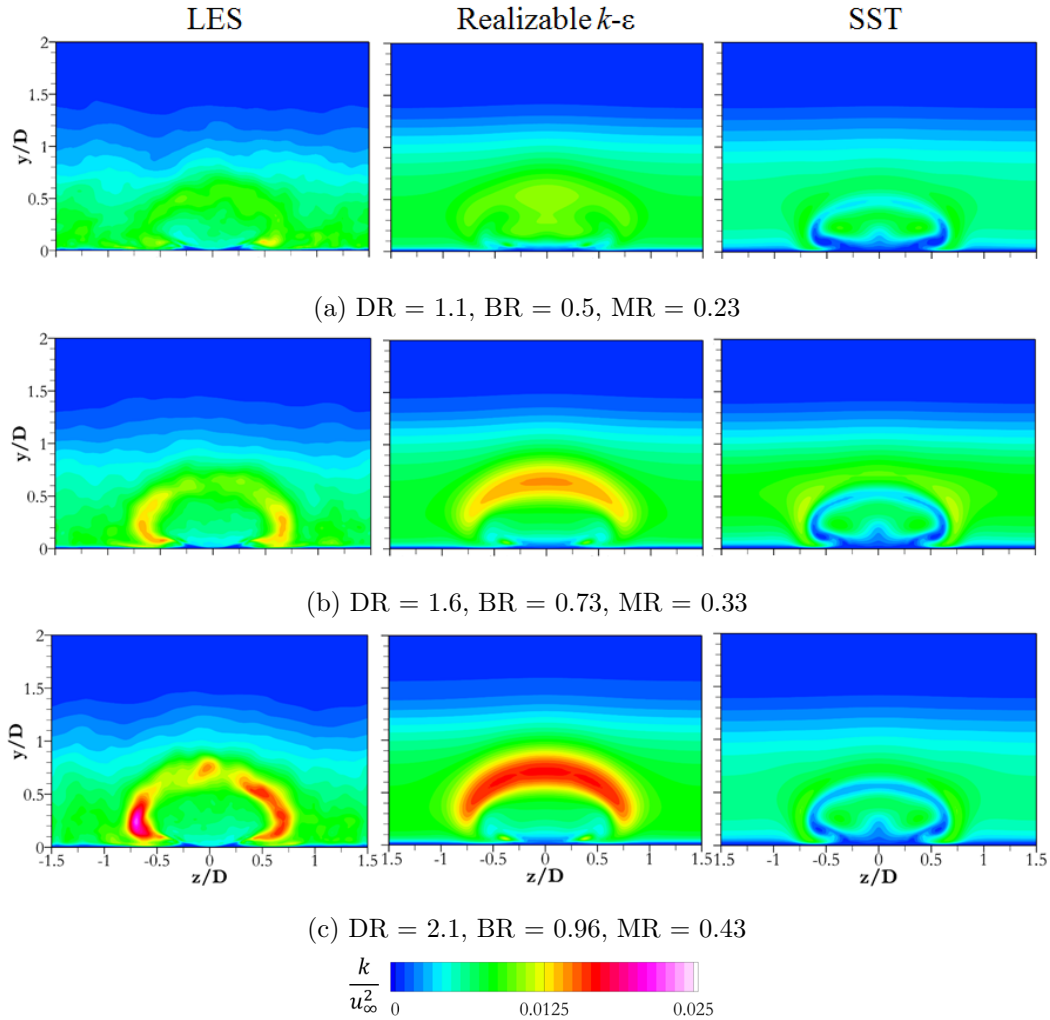


Figure 4.7.: Non-dimensional turbulent kinetic energy at $x/D = 0$ for $VR = 0.46$

4.2.3 Reynolds Stresses

When the Navier-Stokes equations undergo Reynolds averaging, the resulting equations, called RANS, have an unknown term, $\widetilde{u_i''u_j''}$. This term is the Reynolds stress and it must be modeled. One such model proposes that much like how the viscous stresses are taken to be proportional to the rate of deformation of fluid elements, the Reynolds stresses might be proportional to mean rates of deformation; this is the Boussinesq hypothesis. The Boussinesq hypothesis is a linear relationship between

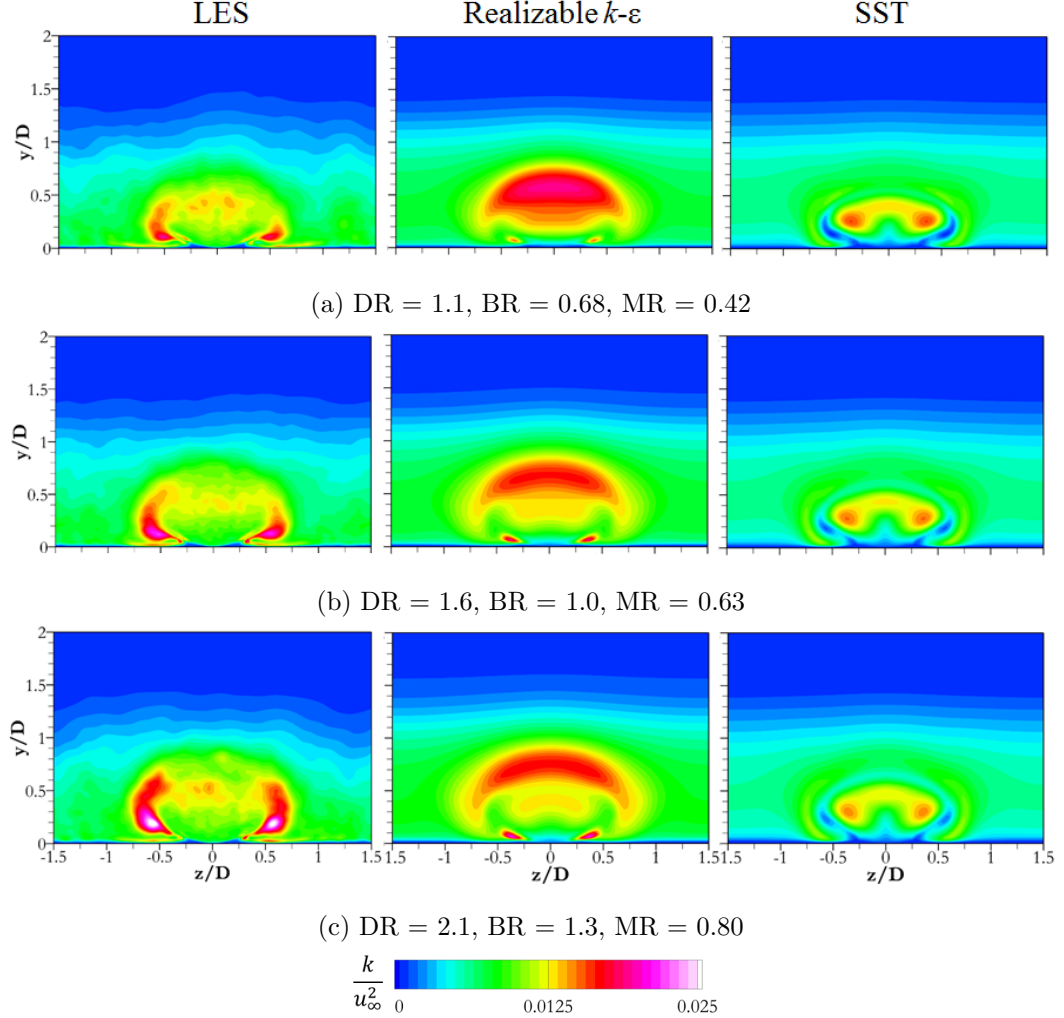


Figure 4.8.: Non-dimensional turbulent kinetic energy at $x/D = 0$ for $VR = 0.63$

the stress and strain and is the main assumption that two-equation turbulence models utilize to define the Reynolds stresses; it is defined as follows:

$$\widetilde{u_i'' u_j''} = -2\nu_t \left(S_{ij} - \frac{1}{3} \frac{\partial \widetilde{u}_k}{\partial x_k} \delta_{ij} \right) + \frac{2}{3} k \delta_{ij} \quad (4.1)$$

where ν_t is the eddy viscosity, $S_{ij} = \frac{1}{2} \left(\frac{\partial \widetilde{u}_i}{\partial x_j} + \frac{\partial \widetilde{u}_j}{\partial x_i} \right)$ is the strain rate tensor, and δ_{ij} is the Kronecker delta. The eddy viscosity is computed from the turbulent kinetic energy and the dissipation rate. One particular weakness of this approach is that the anisotropy of the Reynolds stress tensor is simply a copy of the anisotropy of the

strain rate tensor. In complex flows that exhibit high degrees of anisotropy, such as a jet-in-crossflow, this treatment may be too simplistic. Using Eq. 4.1 the Reynolds stress components predicted by RANS can be compared directly to the LES results. Note that LES resolves the turbulent fluctuations, therefore the Reynolds stresses are computed directly without the need of any model. As was shown in Chapter 3, the $\widetilde{u''w''}$ component is difficult for RANS to predict accurately over varying VRs. Figure 4.9 plots contours of this component at $x/D = 0$ to determine how it scales when VR is fixed at 0.46. The LES results show that the magnitude increases with MR, especially near the wall, where $\widetilde{u''w''}$ from the sides of the jet curves around underneath the jet. While RANS predicts an increase in magnitude with MR, it predicts very little change in $\widetilde{u''w''}$ near the wall. In fact, both models predict $\widetilde{u''w''}$ values near zero too far off the wall.

4.2.4 Turbulent Heat Flux

Two-equation RANS models use the gradient-diffusion hypothesis (GDH) to model the turbulent heat flux, and it is given by

$$\widetilde{u_i''\theta''} = -\frac{\nu_t}{Pr_t} \frac{\partial \widetilde{\theta}}{\partial x_i}, \quad (4.2)$$

where Pr_t is the turbulent Prandtl number ($Pr_t = 0.85$ in the RANS simulations). The turbulent heat flux gives the direction and magnitude of the turbulent transport of heat. The gradient-diffusion hypothesis assumes that turbulence transports heat in the direction of the temperature gradient. When it comes to improving turbulence models, it is generally this model along with the Boussinesq hypothesis that receive the most attention. This is where LES, which resolves these terms directly without models, can provide invaluable insight. Figures 4.10 - 4.12, show each component of Eq. 4.2 at $x/D = 0$ for VR = 0.46. The high contrast contours highlight the positive and negative components. While the $\widetilde{v''\theta''}$ and $\widetilde{w''\theta''}$ show similar magnitudes between the LES and RANS, the $\widetilde{u''\theta''}$ component is underpredicted, especially at the wall. In general, RANS struggles to capture the near wall region, as was seen in the turbulent

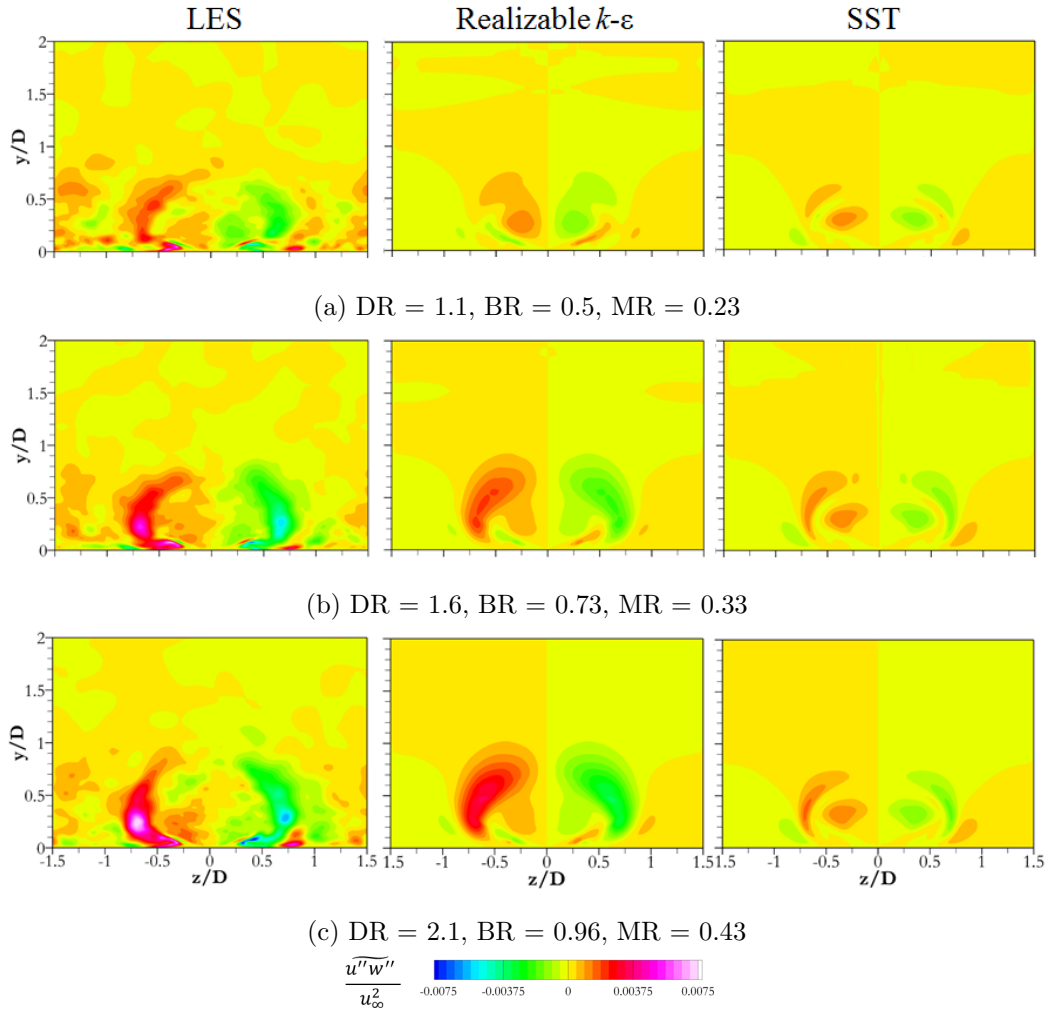


Figure 4.9.: Non-dimensional $\widetilde{u''w''}$ at $x/D = 0$ for VR = 0.46

kinetic energy and Reynolds stresses as well. However, above the wall, realizable k - ϵ more closely resembles the LES contours.

Interestingly, the LES shows in Figs. 4.10 - 4.12 that the magnitude in all components of the turbulent heat flux only increases ~ 1.5 times between the lowest and highest MRs, with the structure remaining relatively constant. This is significant, because turbulent kinetic energy and $\widetilde{u''w''}$ was shown to increase ~ 2.5 times between the lowest and highest MR for a fixed VR. Previous studies [58] have shown that improving the turbulent heat flux model can improve lateral spreading in film cooling.

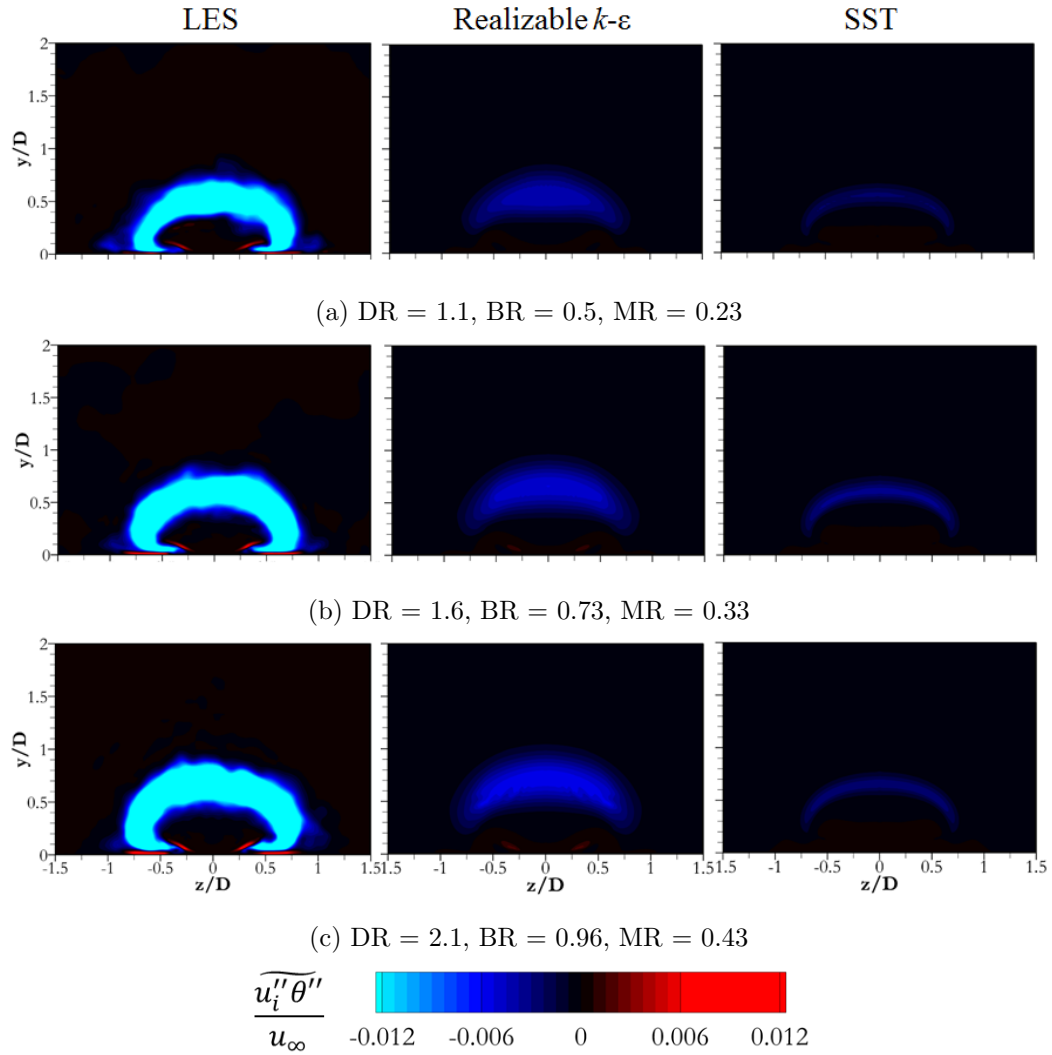


Figure 4.10.: Non-dimensional $\widetilde{u''\theta''}$ at $x/D = 0$ for VR = 0.46

However, these results suggest that Reynolds stresses play a larger role than turbulent heat flux when it comes to predicting cooling trends and the scaling of cooling with MR.

Summary

A computational study based on LES was performed to examine how adiabatic effectiveness and turbulence quantities scale with BR, DR, and MR when the VR

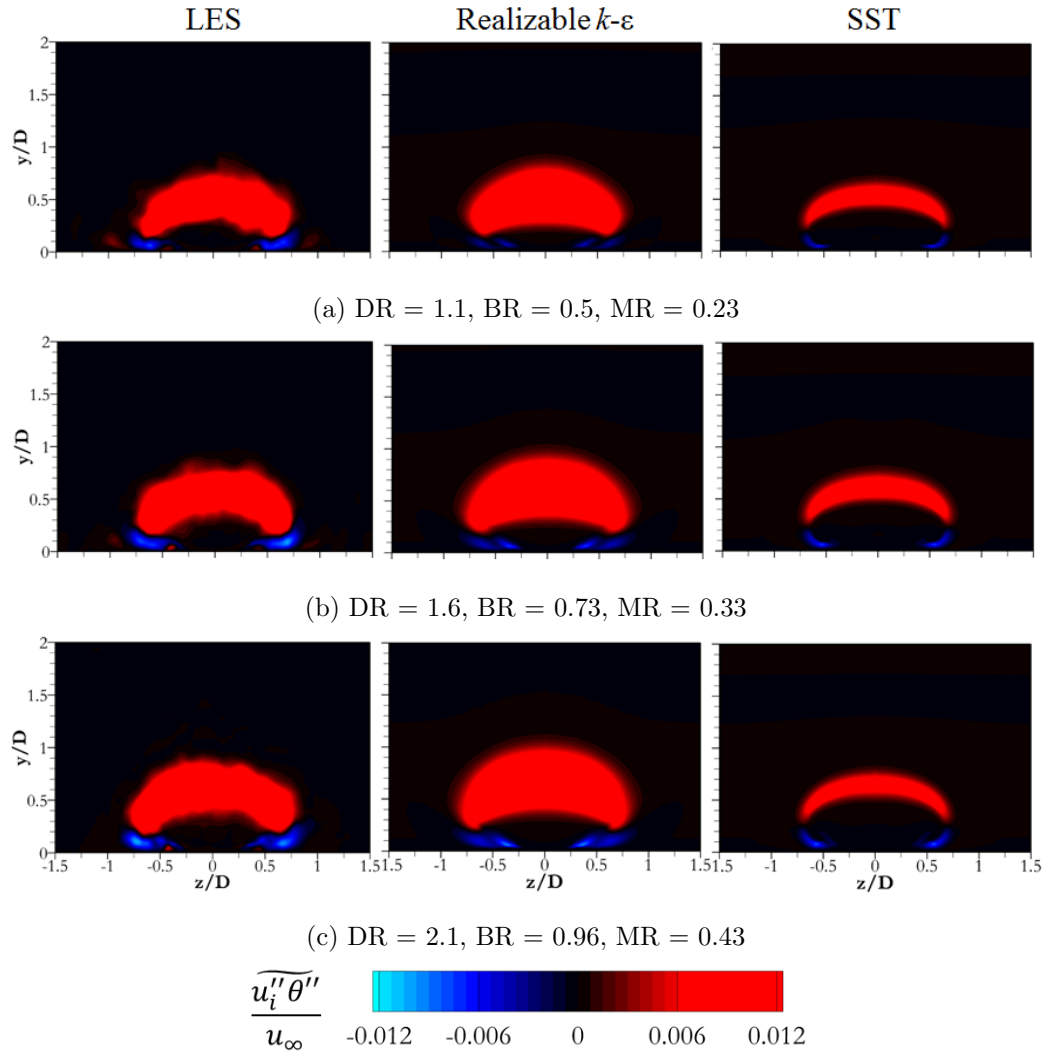


Figure 4.11.: Non-dimensional $\widetilde{v''\theta''}$ at $x/D = 0$ for VR = 0.46

is fixed. Additionally, two RANS turbulence models, realizable $k-\epsilon$ and SST, were evaluated to determine how well they predict trends in adiabatic effectiveness and which modeled terms most impact these trends.

For a fixed VR, the cooling directly downstream of the hole drops and separation increases as MR increases. For VR = 0.46, this results in higher cooling near the hole for smaller MR, but lower cooling downstream compared to higher MR. For the higher VR, a similar trend is seen near the hole, but further downstream, the highest MR no longer outperforms the lower MRs. Additionally, overall cooling drops when

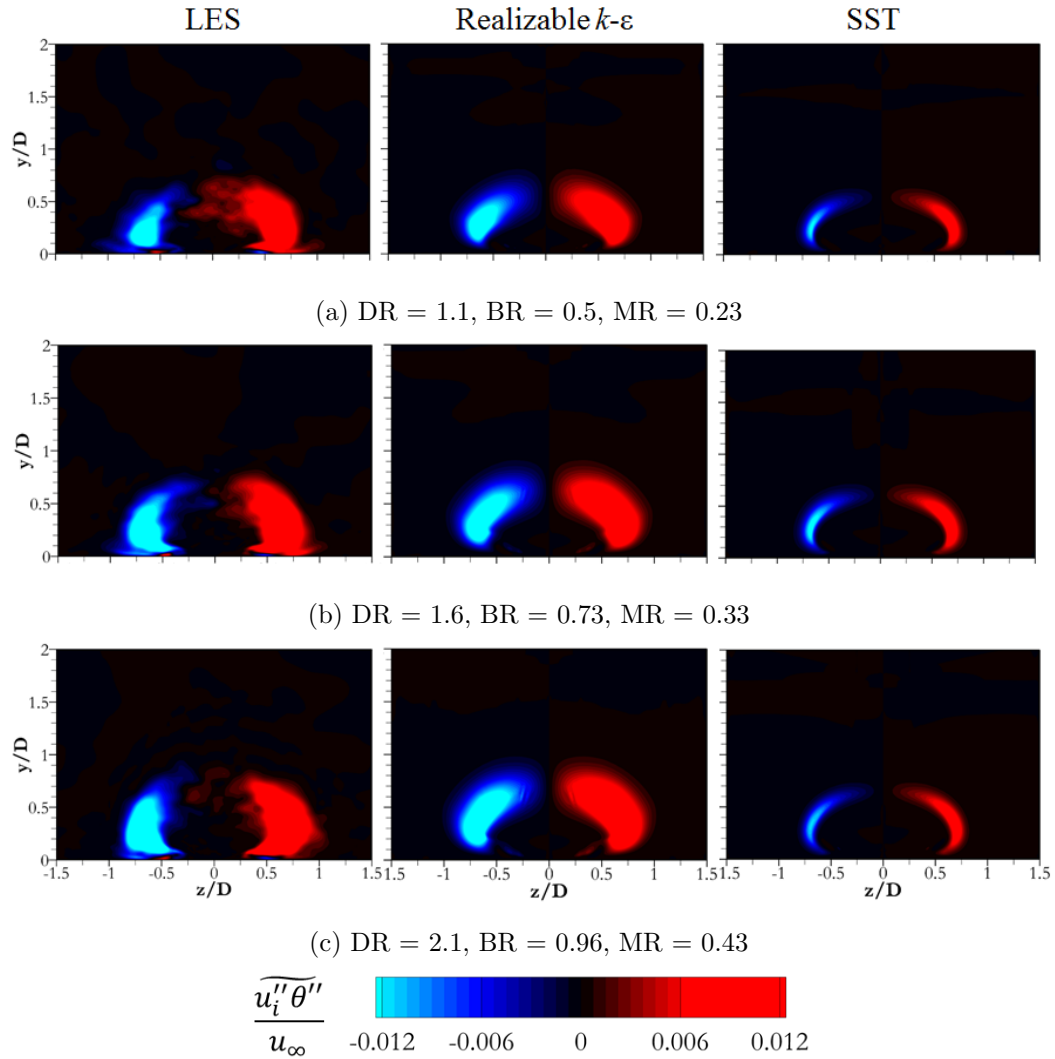


Figure 4.12.: Non-dimensional $\widetilde{w''\theta''}$ at $x/D = 0$ for VR = 0.46

VR increases. RANS can predict lower cooling near the hole as MR increases, but the magnitude of the cooling drop is underpredicted. Further downstream, both RANS models fail to predict the expected differences in adiabatic effectiveness for different MRs. However, RANS does show that overall adiabatic effectiveness drops when VR increases.

The turbulent kinetic energy is found to increase near the hole with MR for a fixed VR. The structure of k reveals that that turbulence mixing is most intense on the sides of the jet near the wall. However, both RANS models significantly under-

predict k at this location. The $\widetilde{u''w''}$ component of Reynolds stress was shown to increase in magnitude with MR, however, the RANS models were found to significantly underpredict the near wall values over the range of MRs. The final turbulence quantity that was evaluated was the turbulent heat flux. This term again was found to be underpredicted by RANS near the walls, and the $\widetilde{u''\theta''}$ terms was underpredicted throughout the entire jet region. However, while the LES showed that the Reynolds stresses and turbulent kinetic energy scaled noticeably with MR, all components of the turbulent heat flux show very little change over a range of MRs. This suggests that the Reynolds stresses play a larger role than turbulent heat flux when it comes to predicting trends in film cooling, especially when the VR is fixed.

5. CONCLUSIONS AND RECOMMENDATIONS

5.1 Summary of Research and Findings

An LES study was performed to understand the effects of VR on the turbulent structure and effectiveness for film cooling of a flat plate through round holes. Additionally, the effect of the inlet boundary condition was evaluated. The implicit LES results were verified by comparing the turbulent boundary layer profiles and velocity spectra on different grids. The adiabatic effectiveness and velocity profiles were validated by comparing with experimental measurements.

- The implicit LES approach was shown to resolve 99.95% of energy-containing eddies and agreed within 5% of DNS and experimental turbulent boundary layer measurements at $Re_{\delta_{mom}} = 670$.
- The instantaneous flow results showed how the shear layer between the jet and crossflow became more unstable as the VR increased. At a low VR the shear layer vortex exhibited a negative z -vorticity, while a high VR showed a positive z -vorticity. The impact of this change in vorticity manifested itself most noticeably in the $\widetilde{u''v''}$ and $\widetilde{u''\theta''}$ statistics, which highlight a shift in the nature of the large-scale mixing.
- Analysis of the non-dimensional temperature, vorticity, Reynolds stresses, and turbulent heat flux reveal that the strength of the CRVP and turbulent mixing scales with VR. Increasing DR at a fixed BR is effectively reducing the VR. Consequently, the CRVP and turbulent mixing weakens resulting in less entrainment of hot crossflow gas and higher film-cooling effectiveness.
- Good agreement with experimental thermal and PIV measurements was found between the LES simulations employing a resolved turbulent boundary layer,

whereas the LES simulations with a mean profile exhibited good agreement at high VRs, but tended to overestimate cooling at low VRs. The mean profile at low VRs resulted in a horseshoe vortex forming upstream of the film-cooling hole which helps to pull cool fluid from the jet outwards toward the wall. The unsteadiness in a resolved turbulent boundary layer inhibits the formation of a horseshoe vortex and the increased mixing reduces the spreading of the coolant. At a high VR it was found that the horseshoe vortex forms for a mean boundary layer, but it gets entrained into the jet and does not enhance the cooling performance. The relatively low turbulent kinetic energy in the jet at a low VR tends to become enhanced in the presence of a resolved turbulent boundary layer, while at a high VRs the jet is already quite energetic and tends not to be affected by the turbulent boundary layer. In general, both a mean and resolved turbulent boundary layer provide sufficient cooling predictions at $VR > 0.6$, but at low VRs the upstream boundary layer should be resolved to accurately predict the cooling performance.

The LES results generated provided new insights into turbulence scaling in film cooling. This data can also be used to find weaknesses in popular turbulence models for film cooling. To get baseline turbulence modeling data for film cooling, two RANS turbulence models were studied: realizable $k-\epsilon$ and $k-\omega$ SST. These RANS simulations were studied for the same geometry and flow conditions as the LES. The thermal and turbulent flow field, Boussinesq hypothesis and gradient-diffusion hypothesis were evaluated.

- In general, RANS can predict the scaling of turbulent kinetic energy and CRVP strength with VR. However, $k-\epsilon$ tends to underpredict the CRVP strength, whereas SST tends to overpredict the CRVP strength. Matching the eddy viscosity predicted by LES could yield more accurate predictions of the CRVP strength in RANS simulations. RANS also underpredicts the near wall temperature gradient, this leads to the noticeable lack of lateral spreading of the coolant.

- The LES data was used to examine the Boussinesq hypothesis. In general, the assumed linear relationship between stress and strain fields is reasonable for $y/D \gtrsim 0.2$, especially for lower VRs. There is some evidence of misalignment of the stress and strain at higher VRs due to the curvature in the streamline induced by the strong CRVP, suggesting that a curvature correction should be utilized.
- In the near wall region ($y/D \lesssim 0.2$), there are non-zero strain rates that are difficult to scale to near-zero stresses, notably S_{12} and S_{23} . Using the method of least-squares an “ideal” scalar eddy viscosity was solved for by using the LES data. This eddy viscosity showed that realizable k - ϵ overpredicted the eddy viscosity while SST underpredicted it. This result correlates with the relative strengths of the CRVP predicted by each model. However, the eddy viscosity from LES approaches zero too far from the wall. Further analysis reveals that this leads to incorrect predictions of Reynolds stresses near the wall, notably $\widetilde{u''w''}$, which influences spreading of the flow laterally over the wall. Thus, anisotropy must be accounted for in the near-wall region, since a scalar eddy viscosity cannot account for the behavior of $\widetilde{u''w''}$ and $\widetilde{u''v''}$ simultaneously.
- The gradient-diffusion hypothesis was evaluated with LES data, showing that film-cooling flow exhibits counter-gradient diffusion near the wall at all VRs as well as in the shear layer at the top of the jet at the highest VR. This directly violates the assumption of the gradient-diffusion hypothesis. However, manipulating the eddy diffusivity or Pr_t could offer possible work-arounds. The Pr_t was estimated with LES data using the method of least-squares, and it was found to decrease to values near 0.1 near the wall, much less than the constant 0.85 that RANS assumes. These results suggest Pr_t should vary spatially, or a non-scalar eddy diffusivity should be utilized near the wall in order to apply the gradient-diffusion hypothesis to film-cooling flow.

The findings thus far have shown that turbulence tends to scale with VR and several effects of VR on turbulence modeling were addressed. However, it is also of interest to understand how turbulence scales with BR, DR, MR when VR is fixed. The LES results continue to provide guidance regarding errors in realizable k - ϵ and k - ω SST turbulence models, specifically regarding trends in cooling and mixing. The adiabatic effectiveness trends, turbulent kinetic energy, Reynolds stresses, and turbulent heat flux were analyzed.

- For a fixed VR, the cooling directly downstream of the hole drops and separation increases as MR increases. For VR = 0.46, this results in higher cooling near the hole for smaller MR, but lower cooling downstream compared to higher MR. For the higher VR, a similar trend is seen near the hole, but further downstream, the highest MR no longer outperforms the lower MRs. Additionally, overall cooling drops when VR increases. RANS can predict lower cooling near the hole as MR increases, but the magnitude of the cooling drop is underpredicted. Further downstream, both RANS models fail to predict the expected differences in adiabatic effectiveness for different MRs. However, RANS does show that overall adiabatic effectiveness drops when VR increases.
- The turbulent kinetic energy is found to increase near the hole with MR for a fixed VR. The structure of k reveals that that turbulence mixing is most intense on the sides of the jet near the wall. However, both RANS models significantly underpredict k at this location.
- The $\widetilde{u''w''}$ component of Reynolds stress was shown to increase in magnitude with MR, however, the RANS models were found to significantly underpredict the near wall values over the range of MRs.
- The turbulent heat flux was found to be underpredicted by RANS near the walls, and the $\widetilde{u''\theta''}$ terms was underpredicted throughout the entire jet region.

- The LES showed that the Reynolds stresses and turbulent kinetic energy scaled noticeably with MR, whereas all components of the turbulent heat flux show very little change over a range of MRs. This suggests that the Reynolds stresses play a larger role than turbulent heat flux when it comes to predicting trends in film cooling, especially when the VR is fixed.

5.2 Recommendation for Future Studies

There are several possibilities for future research based on this work.

- This study offers the most comprehensive turbulence data for film cooling to date. However, there is continued industry interest in determining whether the conclusions presented for round holes hold for shaped holes or compound-angle holes. In particular, jets issued through shaped holes can remain attached at much higher VRs compared to round holes. In compound-angle holes, the CRVP becomes biased resulting in one large dominant vortex. The effect of these special considerations on turbulence scaling is of interest.
- This study makes several conclusions regarding modeling weaknesses. Notably, the near wall region ($y/D < 0.2$) downstream of the film-cooling hole is the most inaccurate. This suggests that a two-layer approach, similar to Lakehal [45], may be the most direct solution. Lakehal used DNS data from channel and boundary layer flows to inform the model. However, the recent improvements in computer power has increased the availability of high resolution LES film-cooling data. This model could account for anisotropy by allowing tensor forms of eddy viscosity and eddy diffusivity in the near wall region.
- The availability of DNS and LES data sets has also increased the popularity of machine learning for turbulence modeling of film-cooling. Several findings from this work are directly applicable to machine learning studies: (1) The change in mixing physics (see Chapter 2) at higher VR must be considered when

training the model; (2) The near wall region shows the largest modeling errors, thus this region must be well resolved; (3) Careful attention must be paid that the model improves capturing film cooling trends, Chapter 4 highlights regions where significant adiabatic effectiveness trends react to MR when changes in turbulent heat flux are minimal.

REFERENCES

REFERENCES

- [1] S. Burd and R. Kaszeta. *What is Film Cooling?* <http://www.me.umn.edu/labs/tcht/measurements/what.html>.
- [2] K. Aainsqatsi. Turbofan Operation, 2008. http://en.wikipedia.org/wiki/File:Turbofan_operation.svg.
- [3] J.C. Han and J.S. Park. Heat Transfer and Pressure Drop in Blade Cooling Channels With Turbulence Promoters (Report No. NASA-CR-3837). Technical report, NASA; Lewis Research Center, 1984.
- [4] R.M. Kelso, T.T. Lim, and A.E. Perry. An Experimental Study of Round Jets in Cross-Flow. *Journal of Fluid Mechanics*, 306:111–144, 1996.
- [5] T.F. Fric and A. Roshko. Vortical Structure in the Wake of a Transverse Jet. *Journal of Fluid Mechanics*, 279:1–47, 1994.
- [6] Krishnan Mahesh. The Interaction of Jets with Crossflow. *Annual Review of Fluid Mechanics*, 45:379–407, 2012.
- [7] D. G. Bogard and K. A. Thole. Gas Turbine Film Cooling. *Journal of Propulsion and Power*, 22(2):249–270, 2006.
- [8] Sumanta Acharya. Film Cooling Simulation and Control. *Heat Transfer Research*, 41(6):601–626, 2010.
- [9] D.K. Walters and J.H. Leylek. A Systematic Computational Methodology Applied to a Three-Dimensional Film-Cooling Flowfield. *Journal of Turbomachinery*, 119(4):777–785, 1997.
- [10] J.D. Ferguson, D.K. Walters, and J.H. Leylek. Performance of Turbulence Models and Near-Wall Treatments in Discrete Jet Film Cooling Simulations. In *ASME 98-GT-438. Turbo Expo: Power for Land, Sea, and Air, Volume 4: Heat Transfer; Electric Power; Industrial and Cogeneration*, 1998.
- [11] Asif Hoda and Sumanta Acharya. Predictions of a Film Coolant Jet in Crossflow With Different Turbulence Models. *Journal of Turbomachinery*, 122(3):558, 2000.
- [12] Mayank Tyagi and Sumanta Acharya. Large Eddy Simulation of Film Cooling Flow From an Inclined Cylindrical Jet. *Journal of Turbomachinery*, 125(4):734–742, 2003.
- [13] C. Dai, L. Jia, J. Zhang, Z. Shu, and J. Mi. On the Flow Structure of an Inclined Jet in Crossflow at Low Velocity Ratios. *International Journal of Heat and Fluid Flow*, 58:11–18, 2016.

- [14] E. Sakai, T. Takahashi, and H. Watanabe. Large-Eddy Simulation of an Inclined Round Jet Issuing Into a Crossflow. *International Journal of Heat and Mass Transfer*, 69:300–311, 2014.
- [15] Lingxu Zhong, Chao Zhou, and Shiyi Chen. Effects of Approaching Main Flow Boundary Layer on Flow and Cooling Performance of an Inclined Jet in Cross Flow. *International Journal of Heat and Mass Transfer*, 103:572–581, 2016.
- [16] Jorg Ziefle and Leonhard Kleiser. Assessment of a Film-Cooling Flow Structure by Large-Eddy Simulation. *Journal of Turbulence*, 9(29):37–41, 2008.
- [17] Jorg Ziefle and Leonhard Kleiser. Numerical Investigation of a Film-Cooling Flow Structure: Effect of Crossflow Turbulence. *Journal of Heat Transfer*, 135(4), 2013.
- [18] Prasad Kalghatgi and Sumanta Acharya. Modal Analysis of Inclined Film Cooling Jet Flow. *Journal of Turbomachinery*, 136(August):081007, 2014.
- [19] P. Renze, W. Schröder, and M. Meinke. Large-Eddy Simulation of Film Cooling Flows at Density Gradients. *International Journal of Heat and Fluid Flow*, 29(1):18–34, 2008.
- [20] Eiji Sakai and Toshihiko Takahashi. Numerical Study on Effects of Density Ratio on Film Cooling Flow Structure and Film Cooling Effectiveness. In *GT2017-63168, Proceedings of ASME Turbo Expo 2017: Turbomachinery Technical Conference and Exposition*, 2017.
- [21] Zachary T. Stratton and Tom I-P. Shih. Effects of Crossflow in an Internal-Cooling Channel on Film Cooling of a Flat Plate Through Compound-Angle Holes. In *GT2015-42771, Proceedings of ASME Turbo Expo 2015: Turbine Technical Conference and Exposition*, 2015.
- [22] Gregory Rodebaugh and Zachary Stratton. Assessment of Large Eddy Simulation Predictive Capability for Compound Angle Round Film Holes. In *GT2015-43602, Proceedings of ASME Turbo Expo 2015: Turbine Technical Conference and Exposition*, 2015.
- [23] X. Guo, W. Schröder, and M. Meinke. Large-eddy simulations of film cooling flows. *Computers and Fluids*, 35(6):587–606, 2006.
- [24] Frank Muldoon and Sumanta Acharya. Analysis of k and epsilon Budgets for Film Cooling Using Direct Numerical Simulation. *AIAA Journal*, 44(12):3010–3021, 2006.
- [25] Yulia V. Peet. *Film Cooling From Inclined Cylindrical Holes Using Large Eddy Simulations*. PhD thesis, Stanford University, Stanford, CA, USA, 2006.
- [26] Ioulia Iourokina and Sanjiva Lele. Large Eddy Simulation of Film-Cooling Above the Flat Surface with a Large Plenum and Short Exit Holes. *44th AIAA Aerospace Sciences Meeting and Exhibit*, pages 1–16, 2006.
- [27] F. Coletti, M. J. Benson, J. Ling, C. J. Elkins, and J. K. Eaton. Turbulent Transport in an Inclined Jet in Crossflow. *International Journal of Heat and Fluid Flow*, 43:149–160, 2013.

- [28] J. Bodart, F. Coletti, I. Bermejo-Moreno, and J. Eaton. High-Fidelity Simulation of a Turbulent Inclined Jet in a Crossflow. *CTR Annual Research Briefs*, pages 263–275, 2013.
- [29] N.W. Foster and D. Lampard. Effects of Density and Velocity Ratio on Discrete Hole Film Cooling. *AIAA Journal*, 13(8):1112–1114, 1975.
- [30] R.J. Goldstein, R.G. Eckert, and D.R. Pedersen. Film Cooling With Large Density Differences Between the Mainstream and the Secondary Fluid Measured by the Heat-Mass Transfer Analogy. *Journal of Heat Transfer*, 99(4):620–627, 1977.
- [31] J. Pietrzyk, D. Bogard, and M. Crawford. Hydrodynamics Measurements of Jets in Crossflow for Gas Turbine Film-Cooling Applications. *Journal of Turbomachinery*, 111(2):139–145, 1989.
- [32] J. Pietrzyk, D. Bogard, and M. Crawford. Effects of Density Ratio on the Hydrodynamics of Film Cooling. *Journal of Turbomachinery*, 112(3):437–443, 1990.
- [33] A.K. Sinha, D.G. Bogard, and M.E. Crawford. Film-Cooling Effectiveness Downstream of a Single Row of Holes With Variable Density Ratio. *Journal of Turbomachinery*, 113(3):442 – 449, 1991.
- [34] Blake Johnson, Wei Tian, Kai Zhang, and Hui Hu. An experimental study of density ratio effects on the film cooling injection from discrete holes by using PIV and PSP techniques. *International Journal of Heat and Mass Transfer*, 76:337–349, 2014.
- [35] Wenwu Zhou, Blake Johnson, and Hui Hu. Effects of Flow Compressibility and Density Ratio on Film Cooling Performance. *Journal of Propulsion and Power*, 33(4):964–974, 2016.
- [36] Kyle R. Vinton, Travis B. Watson, Lesley M. Wright, Daniel C. Crites, Mark C. Morris, and Ardeshir Riahi. Combined Effects of Freestream Pressure Gradient and Density Ratio on the Film Cooling Effectiveness of Round and Shaped Holes on a Flat Plate. *Journal of Turbomachinery*, 139(4), 2017.
- [37] M.K. Eberly. *Time-Resolved Studies of High Density Ratio Film-Cooling Flows*. Ms thesis, The Pennsylvania State University, University Park, Pennsylvania, 2012.
- [38] Molly K. Eberly and Karen A. Thole. Time-Resolved Film-Cooling Flows at High and Low Density Ratios. *Journal of Turbomachinery*, 136(6), 2014.
- [39] Gregory M. Laskowski, James Kopriva, Vittorio Michelassi, Sriram Shankaran, Umesh Paliath, Rathakrishnan Bhaskaran, Qiqi Wang, Chaitanya Talnikar, Zhi J. Wang, and Feilin Jia. Future Directions of High Fidelity CFD for Aerothermal Turbomachinery Analysis and Design. In *46th AIAA Fluid Dynamics Conference*, pages 1–30, 2016.
- [40] Chunhua Wang, Jingzhou Zhang, and Junhui Zhou. Optimization of a Fan-shaped Hole to Improve Film Cooling Performance by RBF Neural Network and Genetic Algorithm. *Aerospace Science and Technology*, 58:18–25, 2016.

- [41] Paul A. Durbin. Some Recent Developments in Turbulence Closure Modeling. *Annual Review of Fluid Mechanics*, 50(1):77–103, 2018.
- [42] G. Bergeles, A. D. Gosman, and B. E. Launder. The Turbulent Jet in a Cross Stream at Low Injection Rates: A Three-Dimensional Numerical Treatment. *Numerical Heat Transfer*, 1(2):217–242, 1978.
- [43] D. Lakehal, G. S. Theodoridis, and W. Rodi. Three-dimensional Flow and Heat Transfer Calculations of Film Cooling at the Leading Edge of a Symmetrical Turbine Blade Model. *International Journal of Heat and Fluid Flow*, 22(2):113–122, 2001.
- [44] A. Azzi and D. Lakehal. Perspectives in Modeling Film Cooling of Turbine Blades by Transcending Conventional Two-Equation Turbulence Models. *Journal of Turbomachinery*, 124(3):472–484, 2002.
- [45] Djamel Lakehal. Near-Wall Modeling of Turbulent Convective Heat Transport in Film Cooling of Turbine Blades With the Aid of Direct Numerical Simulation Data. *Journal of Turbomachinery*, 124(3):485–498, 2002.
- [46] R. Jones, S. Acharya, and A. Harvey. Improved Turbulence Modeling of Film Cooling Flow and Heat Transfer. *Transactions on State of the Art in Science and Engineering*, 15:103–134, 2005.
- [47] Cun Liang Liu, Hui R. Zhu, and Jiang T. Bai. Effect of Turbulent Prandtl Number on the Computation of Film-Cooling Effectiveness. *International Journal of Heat and Mass Transfer*, 51(25-26):6208–6218, 2008.
- [48] Cun Liang Liu, Hui Ren Zhu, and Jiang Tao Bai. New Development of the Turbulent Prandtl Number Models for the Computation of Film Cooling Effectiveness. *International Journal of Heat and Mass Transfer*, 54(4):874–886, 2011.
- [49] Xueying Li, Yanmin Qin, Jing Ren, and Hongde Jiang. Algebraic Anisotropic Turbulence Modeling of Compound Angled Film Cooling Validated by Particle Image Velocimetry and Pressure Sensitive Paint Measurements. *Journal of Heat Transfer*, 136(3), 2013.
- [50] Xueying Li, Jing Ren, and Hongde Jiang. Film Cooling Modeling of Turbine Blades Using Algebraic Anisotropic Turbulence Models. *Journal of Turbomachinery*, 136(11), 2014.
- [51] Karthik Duraisamy, Gianluca Iaccarino, and Heng Xiao. Turbulence Modeling in the Age of Data. *Annual Review of Fluid Mechanics*, 51:357–377, 2019.
- [52] J. Ling and J. Templeton. Evaluation of Machine Learning Algorithms for Prediction of Regions of High Reynolds Averaged Navier Stokes Uncertainty. *Physics of Fluids*, 27(8), 2015.
- [53] J. Weatheritt and R. D. Sandberg. The Development of Algebraic Stress Models Using a Novel Evolutionary Algorithm. *International Journal of Heat and Fluid Flow*, 68(April):298–318, 2017.
- [54] Julia Ling, Andrew Kurzawski, and Jeremy Templeton. Reynolds Averaged Turbulence Modelling Using Deep Neural Networks with Embedded Invariance. *Journal of Fluid Mechanics*, 807:155–166, 2016.

- [55] J. Nathan Kutz. Deep Learning in Fluid Dynamics. *Journal of Fluid Mechanics*, 814:1–4, 2017.
- [56] R. D. Sandberg, R. Tan, J. Weatheritt, A. Ooi, A. Haghiri, V. Michelassi, and G. Laskowski. Applying Machine Learnt Explicit Algebraic Stress and Scalar Flux Models to a Fundamental Trailing Edge Slot. *Journal of Turbomachinery*, 140(10):101008, 2018.
- [57] Pedro M. Milani, Julia Ling, Gonzalo Saez-Mischlich, Julien Bodart, and John K. Eaton. A Machine Learning Approach for Determining the Turbulent Diffusivity in Film Cooling Flows. *Journal of Turbomachinery*, 140(2), 2017.
- [58] Julia Ling, Kevin Ryan, Julien Bodart, and John Eaton. Analysis of Turbulent Scalar Flux Models for a Discrete Hole Film Cooling Flow. *Journal of Turbomachinery*, 138(1), 2016.
- [59] Julia Ling, Anthony Ruiz, Guilhem Lacaze, and Joseph Oefelein. Uncertainty Analysis and Data-Driven Model Advances for a Jet-in-Crossflow. *Journal of Turbomachinery*, 139(2), 2016.
- [60] Zachary T. Stratton and Tom I-P. Shih. Effects of Density and Blowing Ratios on the Turbulent Structure and Effectiveness of Film-Cooling. *Journal of Turbomachinery*, 140(10):1–12, 2018.
- [61] Datta Gaitonde and Miguel Visbal. *High-Order Schemes for Navier-Stokes Equations: Algorithm and Implementation into FDL3DI (Report No. AFRL-VA-WP-TR-1998-3060)*. Air Vehicles Directorate; Air Force Research Laboratory, 1998.
- [62] Miguel R. Visbal and Datta V. Gaitonde. High-Order-Accurate Methods for Complex Unsteady Subsonic Flows. *AIAA Journal*, 37(10):1231–1239, 1999.
- [63] Sanjiva K. Lele. Compact Finite Difference Schemes with Spectral-like Resolution. *Journal of Computational Physics*, 103:16–42, 1992.
- [64] R. M. Beam and R. F. Warming. An Implicit Factored Scheme for the Compressible Navier-Stokes Equations. *AIAA Journal*, 16(4):393–402, 1978.
- [65] T.H. Pulliam and D.S. Chaussee. A Diagonal Form of an Implicit Approximate-Factorization Algorithm. *Journal of Computational Physics*, 39:347–363, 1981.
- [66] M. R. Visbal and D. P. Rizzetta. Large-Eddy Simulation on Curvilinear Grids Using Compact Differencing and Filtering Schemes. *Journal of Fluids Engineering*, 124(4):836–847, 2002.
- [67] Miguel R Visbal and Datta V Gaitonde. On the Use of Higher-Order Finite-Difference Schemes on Curvilinear and Deforming Meshes. *Journal of Computational Physics*, 181:155–185, 2002.
- [68] Daniel J. Garmann, Miguel R. Visbal, and Paul D. Orkwis. Comparative Study of Implicit and Subgrid-Scale Model Large-Eddy Simulation Techniques for Low-Reynolds Number Airfoil Applications. *International Journal for Numerical Methods in Fluids*, 71:1546–1565, 2013.
- [69] Jonathan Poggie, Nicholas J. Bisek, and Ryan Gosse. Resolution Effects in Compressible, Turbulent Boundary Layer Simulations. *Computers & Fluids*, 120:57–69, 2015.

- [70] Scott E. Sherer, Miguel R. Visbal, and Raymond E. Gordnier. A High-Order Overset-Grid Approach for Large Eddy Simulations. In *FEDSM2007-37615, Proceedings of FEDSM2007 ASME/JSME 2007 5th Joint Fluids Engineering Conference*, San Diego, California, 2007.
- [71] Scott E. Sherer and Miguel R. Visbal. Implicit Large Eddy Simulations Using a High-Order Overset Grid Solver. In *AIAA 2004-2530, 34th AIAA Fluid Dynamics Conference and Exhibit*, Portland, Oregon, 2004.
- [72] P. Schlatter and R. Örlü. Assessment of Direct Numerical Simulation Data of Turbulent Boundary Layers. *Journal of Fluid Mechanics*, 659:116–126, 2010.
- [73] P. Schlatter and R. Örlü. Turbulent Boundary Layers at Moderate Reynolds Numbers: Inflow Length and Tripping Effects. *Journal of Fluid Mechanics*, 710:5–34, 2012.
- [74] Stephen B. Pope. *Turbulent Flows*. Cambridge University Press, Cambridge, UK, 2000.
- [75] Seyed G. Saddoughi and Srinivas V. Veeravalli. Local Isotropy in Turbulent Boundary Layers at High Reynolds Number. *Journal of Fluid Mechanics*, 268:333–372, 1994.
- [76] Zachary Stratton and Tom Shih. Identifying Weaknesses in Eddy-Viscosity Models for Predicting Film Cooling via Large-Eddy Simulations. *Journal of Propulsion and Power*, Advance online publication, 2019.
- [77] David C. Wilcox. *Turbulence Modeling for CFD*. DCW Industries, Inc., 3rd edition, 2006.
- [78] F. R. Menter. Two-equation Eddy-Viscosity Turbulence Models for Engineering Applications. *AIAA Journal*, 32(8):1598–1605, 1994.
- [79] T-H. Shih, A Liou, A. Shabbir, Z. Yang, and J. Zhu. *A New k-ε Eddy Viscosity Model for High Reynolds Number Turbulent Flows - Model Development and Validation (Report No. E-9087)*. National Aeronautics and Space Administration, 1994.
- [80] H. C. Chen and V. C. Patel. Near-Wall Turbulence Models for Complex Flows Including Separation. *AIAA Journal*, 26(6):641–648, 1988.
- [81] P.R. Spalart and M. Shur. On the Sensitization of Turbulence Models to Rotation and Curvature. *Aerospace Science and Technology*, 1(5):297–302, 1997.
- [82] Zachary T. Stratton and Tom I-P. Shih. Effects of Velocity Ratio on Trends in Film-Cooling Adiabatic Effectiveness and Turbulence. In *GT2019-90943, ASME Turbo Expo 2019: Turbomachinery Technical Conference and Exposition*, Phoenix, AZ, 2019.

APPENDIX

A. POPE'S MODEL SPECTRUM

This appendix provides details regarding Pope's model spectrum [74] used in Chapter 2 including additional equations and sample code. Note that in this appendix η is the Kolmogorov length scale.

Recall the dimensional equations:

$$E(\kappa) = C\epsilon^{2/3}\kappa^{-5/3}f_L(\kappa L)f_\eta(\kappa\eta) \quad (\text{A.1})$$

$$f_L(\kappa L) = \left[\frac{\kappa L}{\sqrt{(\kappa L)^2 + c_L}} \right]^{5/3+p_0} \quad (\text{A.2})$$

$$f_\eta(\kappa\eta) = \exp(-\beta[(\kappa\eta)^4 + c_\eta^4]^{1/4} - c_\eta) \quad (\text{A.3})$$

$$k = \int_0^\infty E(\kappa) d\kappa \quad (\text{A.4})$$

$$\epsilon = 2\nu \int_0^\infty \kappa^2 E(\kappa) d\kappa. \quad (\text{A.5})$$

$$E_{11}(\kappa_1) = \int_{\kappa_1}^\infty \frac{E(\kappa)}{\kappa} \left(1 - \frac{\kappa_1^2}{\kappa^2} \right) d\kappa \quad (\text{A.6})$$

The non-dimensional energy spectra is

$$\frac{E(\kappa\eta)}{(\nu^5\epsilon)^{1/4}} = C(\kappa\eta)^{-5/3}f_L(\kappa L)f_\eta(\kappa\eta). \quad (\text{A.7})$$

where $\kappa L = \kappa\eta Re_L^{3/4}$.

The non-dimensional turbulent kinetic energy equation is

$$\sqrt{Re_L} = \int_0^\infty \frac{E(\kappa\eta)}{(\nu^5\epsilon)^{1/4}} d(\kappa\eta). \quad (\text{A.8})$$

The non-dimensional dissipation equation is

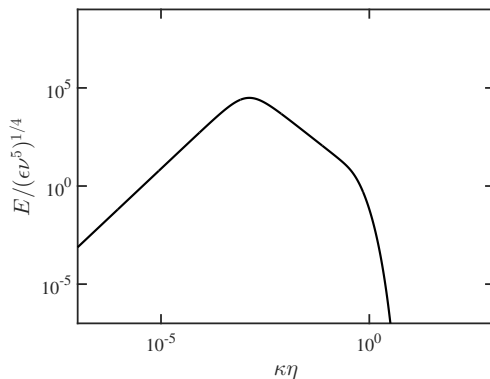
$$\frac{1}{2} = \int_0^\infty (\kappa\eta)^2 \frac{E(\kappa\eta)}{(\nu^5\epsilon)^{1/4}} d(\kappa\eta). \quad (\text{A.9})$$

The non-dimensional 1-D longitudinal spectra is

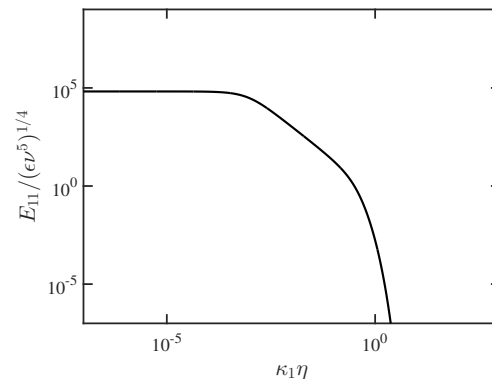
$$\frac{E_{11}(\kappa_1\eta)}{(\nu^5\epsilon)^{1/4}} = \int_{\kappa_1\eta}^\infty \left[\frac{E(\kappa\eta)}{(\nu^5\epsilon)^{1/4}} \right] \frac{1}{\kappa\eta} \left(1 - \frac{(\kappa_1\eta)^2}{(\kappa\eta)^2} \right) d(\kappa\eta) \quad (\text{A.10})$$

A.1 Code and Output

The Matlab script to solve the non-dimensional equations at a desired Re_L is given below. The three-dimensional and one-dimensional longitudinal spectra are plotted in Fig. A.1 using Saddoughi and Veeravalli's [75] turbulent boundary layer data.



(a) Three-dimensional spectra



(b) One-dimensional longitudinal spectra

Figure A.1.: Sample output for Pope's model spectra, $Re_L = 26700$.

```

1 %%%%%%%%%%
2 % Compute Popes Model Spectrum – Non-dimensionalized
3 % Zachary Stratton
4 % Ph.D. Dissertation Appendix A
5 % 2019
6 %%%%%%%%%%

```

```

7
8  clc;
9  clear all;
10 close all;
11
12 %Example: Saddoughi & Veeravalli for Low speed, y = 515
13 tke = 0.73/2; %m^2/s^2
14 epsilon = 0.33; %m^2/s^3
15 kolm_scale = 0.32/1000; %m
16 nu = 1.512e-5; %m^2/s
17
18 Re_L = tke^2/(epsilon*nu)
19 %Re_L = 20000000
20
21 %Model Constants
22 C = 1.5;
23 beta = 5.2;
24 p_0 = 2;
25
26 %Define the function - 1st equation satisfies TKE, 2nd
    equation satisfies
27 %dissipation; function variable is x where x(1) = c_L and x
    (2) =
28 %c_eta; the variable being integrated is eta_kap, note that
    kappa*L =
29 %eta_kap*Re_L^(3/4):
30 fun = @(x) [sqrt(Re_L) - integral(@(eta_kap) C .* eta_kap
    .^(-5/3) .* ...

```

```

31      (eta_kap.*Re_L.^(3/4) ./ ((eta_kap.*Re_L.^(3/4)).^2 +
      x(1)).^(1/2)).^(5/3 + p_0) .* ...
32      exp(-beta.*(((eta_kap).^4 + x(2).^4).^(1/4) - x(2)))
      ,10e-15,1000), ...
33      (1/2) - integral(@(eta_kap) eta_kap.^2 .* C .*
      eta_kap.^(-5/3) .* ...
34      (eta_kap.*Re_L.^(3/4) ./ ((eta_kap.*Re_L.^(3/4)).^2 +
      x(1)).^(1/2)).^(5/3 + p_0) .* ...
35      exp(-beta.*(((eta_kap).^4 + x(2).^4).^(1/4) - x(2)))
      ,10e-15,1000)];

36
37 options = optimoptions('fsolve', 'Display', 'iter', 'TolFun', 1e
      -30, 'TolX', 1e-30, 'MaxFunEvals', 1000);
38 x0 = [10, 1];
39 x = fsolve(fun, x0, options);
40
41 %define c_L and c_eta; now you have defined f_L and f_eta for
      the give Re_L
42 c_L = x(1)
43 c_eta = x(2)
44
45 % plug in results and solve for non-dimensional E as function
      of kappa*eta
46 eta_kap = logspace(-10,10,1000);
47 E = C .* eta_kap.^(-5/3) .* ...
48      (eta_kap.*Re_L.^(3/4) ./ ((eta_kap.*Re_L.^(3/4)).^2 +
      x(1)).^(1/2)).^(5/3 + p_0) .* ...
49      exp(-beta.*(((eta_kap).^4 + x(2).^4).^(1/4) - x(2)));
      %divide by (epsilon.*nu.^5).^(1/4)

```

```

50
51 %Plot 3-D spectrum
52 loglog(eta_kap,E,'k-', 'linewidth',1.7)
53 axis([10e-8 10e2 10e-8 10e8])
54 xlabel('$\kappa \eta$', 'Interpreter', 'LaTeX', 'FontSize'
      , 17)
55 ylabel('$E/(\epsilon \nu^5)^{1/4}$', 'Interpreter', 'LaTeX', '
      FontSize' , 17)
56 set(gca, ...
57     'FontSize' , 14, ...
58     'FontName' , 'Times', ...
59     'Box' , 'on' , ...
60     'TickDir' , 'in' , ...
61     'TickLength' , [.02 .02] , ...
62     'XMinorTick' , 'on' , ...
63     'YMinorTick' , 'on' , ...
64     'YGrid' , 'off' , ...
65     'LineWidth' , 1.4 );
66
67 % Compute longitudinal 1-D spectrum
68 kap_1 = logspace(-8,10,1000);
69 for i = 1:1000
70     % kap_1(i) = 10e-8 + 10000*(i-1);
71     E_11(i) = integral(@(eta_kap) C .* (1./eta_kap) .*
72         eta_kap.^(-5/3) .* ...
73         (eta_kap.*Re_L.^(3/4) ./ ((eta_kap.*Re_L.^(3/4)).^2 +
74             x(1)).^(1/2)).^(5/3 + p_0) .* ...
75         exp(-beta.*(((eta_kap).^4 + x(2)).^4).^(1/4) - x(2)))
76         .* ...

```

```

74         (1 - (kap_1(i).^2./eta_kap.^2)),kap_1(i),1000);
75 end
76
77 %Plot longitudinal 1-D spectrum
78 figure(2)
79 loglog(kap_1,E_11,'k-','linewidth',1.7)
80 axis([10e-8 10e2 10e-8 10e8])
81 xlabel('$\kappa_1 \ \eta$', 'Interpreter', 'LaTeX', 'FontSize'
      ,
      17)
82 ylabel('$E_{11}/(\epsilon \ \nu^5)^{1/4}$', 'Interpreter', 'LaTeX'
      , 'FontSize' , 17)
83 set(gca, ...
84     'FontSize' , 14, ...
85     'FontName' , 'Times', ...
86     'Box' , 'on' , ...
87     'TickDir' , 'in' , ...
88     'TickLength' , [.02 .02] , ...
89     'XMinorTick' , 'on' , ...
90     'YMinorTick' , 'on' , ...
91     'YGrid' , 'off' , ...
92     'LineWidth' , 1.4 );

```